Fluid Dynamics Modelling and Experimental Studies of the Flowing Electrolyte Channel in a Flowing Electrolyte – Direct Methanol Fuel Cell

by

Eric Duivesteyn

A thesis submitted to the Faculty of Graduate and Postdoctoral Affairs in partial fulfillment of the requirements for the degree of

Master of Applied Science

in

Mechanical Engineering

Carleton University
Ottawa, Ontario

Abstract

Fuel cells, and direct methanol fuel cells in particular, are a technology with intriguing potential. However, methanol crossover is a significant concern in direct methanol fuel cells that reduces power and efficiency. The flowing electrolyte – direct methanol fuel cell is a concept intended to combat this issue by using a sulphuric acid flowing electrolyte layer to remove crossed-over methanol before it can reach the cathode.

Hydrodynamic modelling of the flowing electrolyte channel was conducted in order to investigate the flow characteristics in this porous channel and analyze its response to various parameters. It was concluded that pressure drop decreases with temperature, is proportional to volume flux but unaffected by channel thickness, and can be reduced by increasing permeability, which can be achieved with higher porosities and pore diameters. Experimental studies noted improved cell performance at higher temperatures, but limited improvements at higher volume fluxes, likely due to leakage associated with higher pressure drops. Experimentally estimated permeability values had some discrepancy with theoretical values, highlighting the sensitivity of permeability values to imprecise parameters.

It was recommended that the flowing electrolyte channel should be very thin with a higher sphere diameter and lower porosity with a flow rate high enough to effectively negate methanol crossover. However, a possible alternative may be to use a higher porosity, but increase the flow rate to achieve the same performance; this may result in a lower pressure drop.

Acknowledgements

I would like to thank a number of individuals for their roles in making this work possible. First of all, I would like to thank my supervisors, Dr. Edgar Matida and Dr. Cynthia Cruickshank. Their advice, guidance, and feedback have always been helpful and insightful, and I am truly grateful to have had such excellent supervisors.

Secondly, I would like to thank my colleagues David Ouellette and Yashar Kablou for sharing their expertise and experience on fuel cell modelling and experimentation with me.

I would also like to acknowledge the Natural Science and Engineering Research Council of Canada (NSERC) and the Ontario Centres of Excellence (OCE) for their financial support.

Finally, but most importantly, I would like to thank my family: specifically my parents, Peter and Judy, for their support and encouragement, and my fiancée Megan for her patience and love throughout this process.

Table of Contents

List of Tables

List of Figures

Nomenclature

Acronyms

ABL	anode backing layer
BL	backing layer
ACL	anode catalyst layer
AFC	anode flow channel
CBL	cathode backing layer
CCL	cathode catalyst layer
CFC	cathode flow channel
CFD	computational fluid dynamics
CL	catalyst layer
DMFC	direct methanol fuel cell
FE-DMFC	flowing electrolyte - direct methanol fuel cell
FEC	flowing electrolyte channel
PEM	polymer electrolyte membrane or proton exchange membrane

Variables

$\mathbf{A}$	infinitesimal vector control surface [m^2]
$\mathbf{A'}$	vector area available to flow [m^2]
B_x	bias error of x
C	concentration [M]
C_i	initial concentration [M]

d	mean sphere diameter [m]
E	reversible cell potential [V]
e	total bias or random error
e_i	elemental bias or random error
F	Faraday's constant [9.6485×10^4 C/mol]
$\Delta \bar{g}_f$	change of molar Gibb's free energy of formation [J/mol]
h	enthalpy [J/kg]
i	current [A]
$\mathbf{K}$	area porosity tensor [unitless]
K_{loss}	loss coefficient [m^{-1}]
K_{perm}	permeability coefficient or permeability [m^2]
L	length of porous domain in streamwise direction [m]
P	power [W]
P	pressure [Pa]
Q	flow rate [m^3/s]
q	volume flux [m/s]
R_x	random error of x
$\mathbf{S_M}$	momentum source per unit volume per unit time [N/m^3]
S_E	energy source [$J/(m^3 \cdot s)$]
T	temperature [K]
t	time [s]
$t_{\upsilon,95}$	Student-t factor for 95% confidence interval
$\mathbf{U}$	velocity tensor [m/s]

U	total uncertainty, including bias and random error
V	voltage [V]
V	total volume [m^3]
V'	fluid volume [m^3]
V_i	initial volume [m^3]
V_f	final volume [m^3]
w	width of flowing electrolyte perpendicular to flow and thickness [m]
x	an arbitrary quantity
$\bar{x}$	sample mean of a quantity
y	an arbitrary quantity
z	electrons released per molecule in reaction [unitless]

Greek Letters

γ	porosity [unitless]
θ_i	sensitivity index for an elemental error source
λ	thermal conductivity [W/(m·K)]
μ	dynamic viscosity [Pa·s]
ρ	density [kg/m3]
τ	shear stress [N/m^2]

Subscripts

i	with respect to an elemental error source
x	component in arbitrary x-direction

x	with respect to the arbitrary quantity x
y	with respect to an arbitrary quantity y

Superscripts

T	transposed matrix

1 Chapter: Introduction

1.1 Introduction to Fuel Cells

1.1.1 Motivation for Fuel Cell Technology

Over the past few decades, public awareness and concern for environmentalism has risen drastically. In particular, there are many concerns about the exploitation of traditional energy sources such as fossil fuels. These fuels release harmful pollutants which are known to be damaging to the environment, including contributing to climate change. Even if this were not the case, there are also concerns regarding the finite nature of the fossil fuel supply; it is a non-renewable resource that cannot last forever. It is therefore obvious that new sources of energy and/or new approaches to using current energy sources must be explored.

There are numerous proposals for sustainable and practical sources of future energy. Wind, solar, hydroelectric, geothermal, and nuclear energy are some examples. Many experts have developed and analyzed these energy sources with the goal of moving towards a sustainable and environmentally-conscious energy sector.

Fuel cells are one these technologies that may play a role in the future of energy. They are devices that convert chemical potential energy into electrical energy, similar to a battery. The main distinction between a fuel cell and a battery, however, is that a fuel cell can operate continuously as long as fuel is continuously supplied, similar to a

combustion engine. However, unlike combustion engines, fuel cells involve not combustion, but rather oxidation and reduction reactions. Some of the advantages of fuel cell technology can be summarized as such [1]:

- They offer the potential to use renewable fuels, and typically produce little or no greenhouse gases.
- They directly produce electricity as a useful output, and do so continuously as long as fuel is supplied.
- Since they utilize the electrochemical potential of the fuel, their efficiency is not limited by Carnot's theorem, which governs the efficiency of a heat engine. Instead, a fuel cell is typically between 40 and 60% efficient [2], compared to the 25% efficiency of a typical internal combustion engine in a car [3].
- They have no moving parts, making their assembly not particularly complex, making mechanical fatigue and wear not particularly concerning, and reducing noise.
- Types of fuel cells exist that operate at relatively low temperatures (less than 100°C) for applications where that is necessary, while other types operate at high temperatures (500 to 1000°C) so that excess heat can be captured for heating or electricity generation.

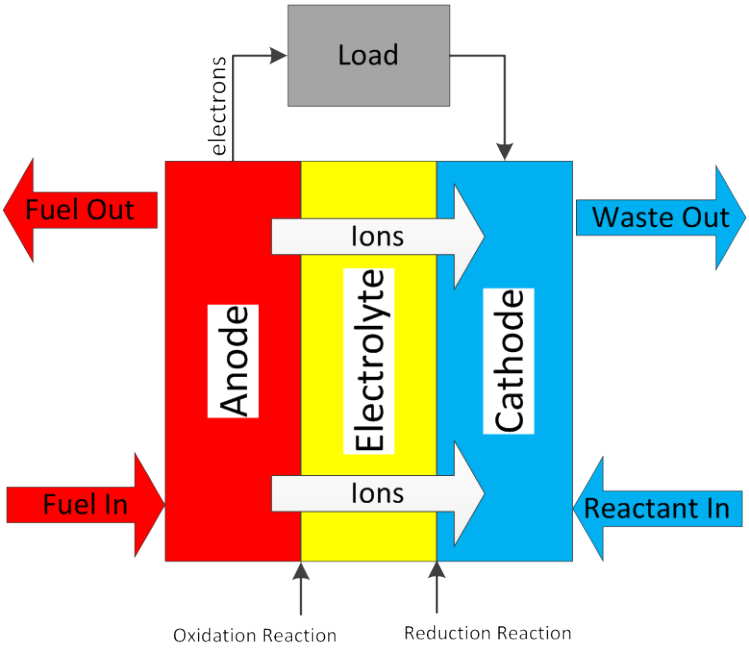

Figure 1 - General fuel cell schematic

1.1.2 General Description of Fuel Cell Technology

Generally speaking, a fuel cell consists of three main sections in series: an anode, an electrolyte, and a cathode, respectively, as shown in Figure 1. Fuel is supplied to the anode; at the interface between the anode and the electrolyte is a thin catalyzing region where the fuel is oxidized, producing products that include free electrons. Another chemical is supplied to the cathode as the oxidant; at the interface between the electrolyte and cathode, this oxidant reacts with electrons in a reduction reaction to form a product. The electrolyte is designed to resist the transport of electrons, forcing them to travel from the anode to the cathode in an external circuit, while allowing the transport of some other ion that must travel from the anode to the cathode (or vice versa, depending on the fuel cell type) to participate in a reaction. The consumption of ions creates an electrical potential across the cell that drives the electro-osmotic transport of ions across the cell.

Similarly, the consumption of electrons produces an electrical potential that drives the movement of electrons; however, since the electrons cannot pass through the electrolyte, the electrons must be transported from the anode to the cathode through an external circuit. This results in a current that provides electrical energy [1].

The fuel is typically hydrogen or some other chemical compound containing hydrogen, including hydrocarbons and alcohols. The oxidant supplied at the cathode is often oxygen, either in pure form or within air. The waste ideally consists only of water when hydrogen fuel is used, but also contains other products, such as carbon dioxide, when other hydrocarbons or alcohols are used [4].

1.1.3 Types of Fuel Cells

There are many types of fuel cells, each with their own characteristics, advantages, disadvantages, and potential applications. Typically, they are categorized and named by their electrolyte material; several of these fuel cell types are discussed below.

Phosphoric Acid Fuel Cell (PAFC): PAFCs use phosphoric acid as the electrolyte, which is non-conductive to the flow of electrons, but is ionically conductive to positive ions. Like most other fuel cell types, it typically uses hydrogen fuel or some other fuel containing hydrogen, with oxygen or air as the oxidant. They usually operate in the range of 150 to 200°C. Excess heat must be removed, and can be used for other purposes [4, 5].

Solid Oxide Fuel Cell (SOFC): SOFCs have a solid electrolyte material of yttria-stabilized-zirconia, and typically use hydrogen, or some other hydrocarbon fuel, and

oxygen. At the cathode, oxygen gas absorbs electrons, creating negatively-charged oxygen ions, which then travel through the electrolyte to the anode to react with hydrogen, forming water as a waste product and releasing electrons that generate a current as they travel through an external circuit back to the cathode. SOFCs are unusual among fuel cell types in that they involve negative ions traveling from the cathode to the anode instead of positive ions traveling from the anode to the cathode. SOFCs must operate at very high temperatures (generally, 500 to 1000°C), since the ionic conductivity of the electrolyte and reaction rates increase with temperature. These high temperatures are a major challenge in SOFC design and operation; however, they also make SOFCs very appropriate and efficient in applications where thermal energy is desired as a product in addition to the generated electricity, such as in combined heating and power of buildings (cogeneration) [4, 5].

Molten Carbonate Fuel Cell (MCFC): Like SOFCs, MCFCs are classified as high-temperature fuel cells, since they operate at high temperatures (typically around 650°C), and are therefore appropriate for cogeneration applications. Lithium potassium carbonate salt is used as the electrolyte, which is a liquid at high temperatures. Hydrogen or other hydrogen-containing compounds are used as fuel. Carbonate ions are produced in the cathode reaction, and travel through the electrolyte to participate in the anode reaction. MCFCs therefore share this unusual characteristic of negative ions being transported through the electrolyte with SOFCs [4, 5].

Proton Exchange Membrane Fuel Cell (PEMFC): Among those fuel cell types already described, PEMFCs are quite similar to PAFCs in terms of fuels, oxidants, reactions, and mechanisms, except that a proton exchange membrane (PEM) is used as the electrolyte instead of phosphoric acid. A PEM is a proton-conducting membrane, most often a polymer; for this reason, they are often referred to as polymer electrolyte membrane fuel cells, which results in the same acronym, so the two names are often used interchangeably. A catalyst, often platinum, is used at the interfaces between anode, PEM, and cathode in order to facilitate the reactions. PEMFCs operate at much lower temperatures (usually under 120°C) than high-temperature fuel cells, and are therefore classified as low-temperature fuel cells. This makes them unsuitable for high-temperature cogeneration, but much more cooperative in terms of material compatibility and safety. They are well-suited to portable applications such as vehicles and electronics. Hydrogen is a commonly used fuel because it results in no waste products besides water, though other hydrocarbons and alcohols are also common [4, 5]. PEMFCs using methanol, the most basic form of alcohol, are the focus of this research.

1.2 Direct Methanol Fuel Cells

1.2.1 Suitability of Methanol Fuel

Methanol, or CH_3OH, is a suitable fuel because it contains hydrogen atoms that can be ionized, but exists in the form of a stable liquid that is relatively safe to handle and is more volumetrically energy-dense than hydrogen. It is also safer and easier to store than hydrogen because methanol does not require a compressed tank [4, 5].

Methanol is commercially produced most commonly from natural gas using a process called steam reforming. In this process, natural gas is reacted with steam at high temperatures to produce hydrogen gas, carbon monoxide, and carbon dioxide, a mixture called synthesis gas. Then hydrogen gas can be combined with either carbon monoxide or carbon dioxide to produce methanol and water [1].

It has been proposed [6] that methanol may be suitable to be the primary carrier of energy in the near future, in a proposed 'methanol economy.' Methanol can be efficiently produced from fossil fuels, biomass such as agricultural products, municipal waste, wood, and even by recycling waste carbon dioxide. In this proposed methanol economy, methanol could be produced from fossil fuels and carbon dioxide waste at first, while they are still abundant, but the main methanol source could be gradually shifted to carbon dioxide recycling and biomass gasification.

Recycling carbon dioxide to produce methanol involves catalytic hydrogenation of carbon dioxide with hydrogen gas; the hydrogen could be produced by electrolysis (requiring electricity and water, with no other byproducts but oxygen). Alternatively, carbon dioxide can produce methanol through electrochemical reduction by water, with the input of electricity. In both of these carbon recycling processes, the electricity required could be produced by renewable energy sources such as wind, hydroelectric, and nuclear [6].

Biomass gasification uses biomass such as wood waste, municipal waste, animal waste, and agricultural waste, to obtain syngas, which contains methane and is then used to produce methanol through steam reforming [6].

Some of the advantages of a methanol economy are [6]:

- Contrasted to an alternatively proposed hydrogen economy, methanol is a liquid that could use existing gasoline infrastructure; hydrogen would require pressurized containers, and would be less energy-dense both by volume and by weight, when the weight of pressurized containers is taken into account.
- Contrasted to an alternatively proposed ethanol economy, methanol produced from agricultural products is possible from any biomass including agricultural waste; using food is not required.

1.2.2 Characteristics and Operation

A Direct Methanol Fuel Cell (DMFC) is a type of PEMFC that uses methanol fuel instead of hydrogen or some other fuel. 'Direct' refers to the fact that the fuel cell uses methanol as a fuel directly, as opposed to an indirect methanol fuel cell which has an external reformer to convert methanol into hydrogen, which the fuel cell then uses.

In a typical DMFC, whose parts and reactions are shown in Figure 2, a mixture of water and methanol fuel is delivered to the anode side through the anode flow channels (AFC), which are carved on the surface of a metal or graphite anode backing plate. The flow channels are in contact with the anode backing layer (ABL), which is a porous material such as carbon paper, through which the liquid mixture is transported to the anode catalyst layer (ACL), a very thin region on the opposite side of the ABL that is coated with microscopic platinum and ruthenium catalyst particles. The methanol is oxidized at the catalyst layer, producing protons, electrons, and the waste product carbon dioxide. The protons are transported by electro-osmotic, diffusive, and convective forces through the proton exchange membrane to the cathode catalyst layer (CCL). The PEM is

a specialized material, such as Nafion®, that allows protons, but not electrons, to pass through. The electrons are therefore forced to reach the cathode catalyst layer through an external circuit that connects the anode and cathode backing plates. Air or pure oxygen is also supplied to the cathode through the cathode flow channels (CFC), which are carved on the surface of the cathode backing plate. The air or oxygen is then transported through the cathode backing layer (CBL) to the CCL, which is coated with platinum catalyst particles. At the CCL, the electrons and protons participate in the reduction of oxygen, producing water. The waste products in the anode and cathode, carbon dioxide and water respectively, are removed by the anode and cathode flow channels [1, 4].

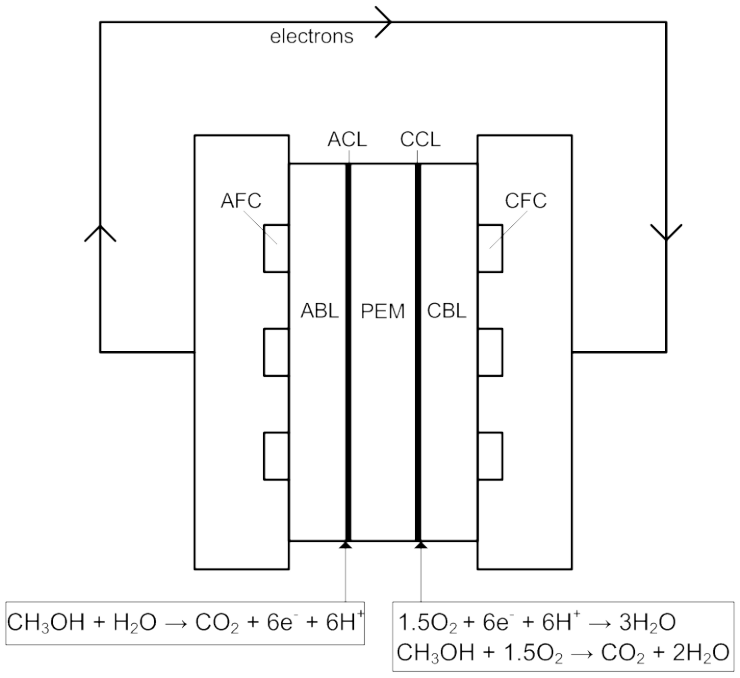

Figure 2 - DMFC schematic and reactions

A summary of the reactions is given here:

Anode half-reaction: $CH_3OH + H_2O \rightarrow CO_2 + 6e^- + 6H^+$

Cathode half-reaction: $1.5O_2 + 6e^- + 6H^+ \rightarrow 3H_2O$

Overall reaction: $CH_3OH + 1.5O2 \rightarrow 2H_2O + CO_2$

The additional cathode reaction shown in Figure 2 will be discussed in Section 1.2.3.

Platinum is most often used as a catalyst in DMFCs, both in the anode and the cathode. At the anode, it is often used in combination with ruthenium to mitigate the effects of catalyst poisoning. The catalyst in the anodes can be poisoned by carbon monoxide particles, which is an intermediary compound in the anode reaction. This means that the carbon monoxide particles preferentially attach to the catalyst sites, limiting the availability of the catalyst. Ruthenium is therefore used in conjunction with platinum at the anode because carbon monoxide will preferentially attach to ruthenium rather than platinum, leaving the platinum available for the desired reaction [7].

1.2.3 Performance and Losses

The reversible cell potential of an ideal DMFC can be calculated as such:

$$E = \frac{\Delta \bar{g}_f}{zF} \quad (1)$$

where E is the reversible cell potential, $\Delta \bar{g}_f$ is the Gibbs free energy release in the reaction, z is the electrons released per molecule, and F is Faraday's constant. For a DMFC, this reversible cell potential is approximately 1.21 V [1]. This is, however,

impossible to actually achieve due to the presence of losses. These losses increase with current density according to the general shape of the cell voltage versus current density curve shown in Figure 3; this graph is commonly referred to as a polarization curve.

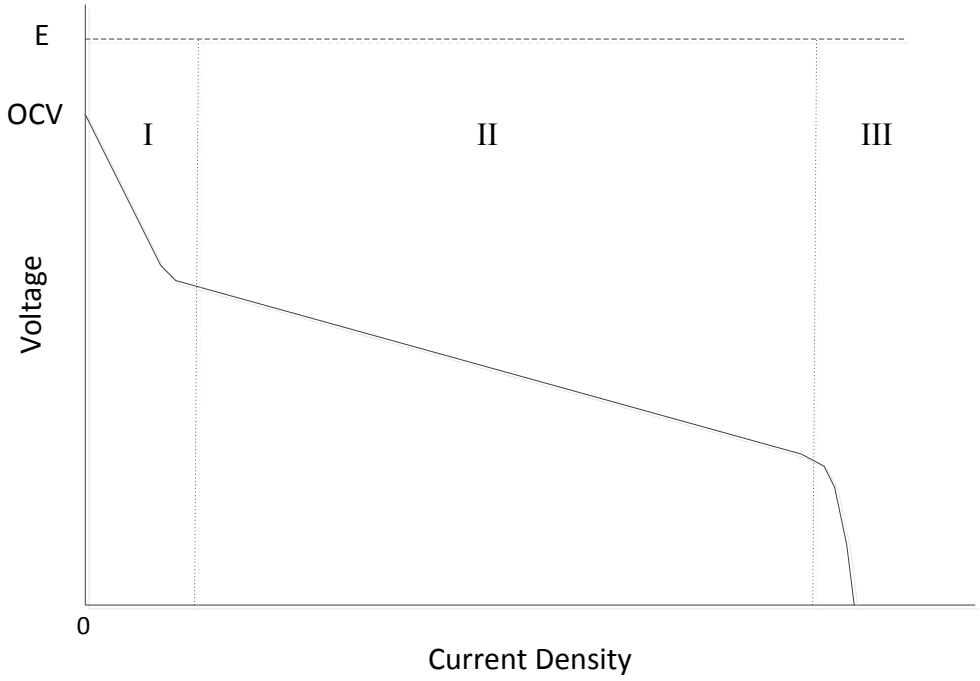

Figure 3 - Typical polarization curve for a DMFC indicating types of losses (I) activation (II) ohmic (III) mass transport

At zero current density, the voltage is below the ideal reversible cell voltage; this actual voltage is called the open circuit voltage (OCV). At low current densities (Region I in the figure), the activation losses are the most prevalent, which are a result of the slow reaction kinetics at such low current densities. The steepness of the curve in Region I is representative of the dominance of activation losses at such low current densities. The reaction kinetics can be improved, thus reducing the activation losses and increasing the

OCV, by raising temperature, improving catalyst loading or dispersion, or increasing the reactant concentration [1, 4].

In Region II, the ohmic losses dominate, which are largely a result of the PEM's resistance to ion transport, though electrical resistance in other portions of the cell (current collectors, backing plates, electrical connections) also play a role. Since ohmic losses increase proportionally to current, as defined by Ohm's Law, the cell voltage nearly linearly decreases in this region [1]. Good conductance and contact throughout the cell reduces these losses, as does a thin and ion-conductive PEM [4].

Region III is dominated by mass transport losses, which are a result of the decreasing availability of reactants at the reaction sites, since reaction rates are very high at high current densities. Mass transport losses eventually dominate since, at high enough current densities, reaction products eventually cannot be removed and reactants cannot arrive at the reaction site rapidly enough. Well-designed diffusion layers and flow channels, combined with suitably high flow rates and reactant concentrations, can delay the onset of significant mass transport losses [1].

Another significant loss with DMFCs is the phenomenon of methanol crossover, in which methanol is undesirably transported through the PEM from the anode to the cathode. The crossed-over methanol reacts with oxygen at the cathode catalyst layer, producing water and carbon dioxide, according to the following reaction, which is also shown on Figure 2:

Crossover reaction: $CH_3OH + 1.5O_2 \rightarrow 2H_2O + CO_2$

This reaction is equivalent to the overall reaction of the anode and cathode half-reactions. It occurs because unreacted methanol molecules tend to be transported by diffusion and by electro-osmotic drag through the PEM by the protons, which are transported to the cathode by electro-osmotic forces. Once reaching the cathode, the methanol is exposed to the reactant, oxygen, and reacts at the CCL. This is an undesirable result because it uses up valuable catalyst sites, decreases the fuel usage efficiency, and is essentially an electrochemical short circuit since the electrons in this reaction do not follow the desired path. This parasitic loss decreases the efficiency, voltage, and power output of the cell [1].

Higher temperatures increase methanol crossover, since transport mechanisms are more active. Supplying lower concentrations of methanol in the anode will reduce methanol crossover, since diffusion is reduced, as will increasing the thickness of the PEM, as experimentally demonstrated by Jung *et al.* [8]. However, these methods are not without their drawbacks; methanol of low concentration is less reactive, and a thicker PEM will increase the ohmic losses due to its lower ion conduction. Despite these careful measures to reduce methanol crossover, it always remains a problem in a DMFC, causing perhaps as much as 40% of losses in most DMFC designs [9].

1.3 Flowing Electrolyte – Direct Methanol Fuel Cells

1.3.1 Motivation and Description

As established, methanol crossover is a significant concern for DMFC design. One proposed solution is to introduce a flowing electrolyte layer (also called a flowing electrolyte channel, FEC) that is encased between two PEMs [10]. The flowing

electrolyte is an ion-conducting fluid, such as sulphuric acid, which conducts protons. The sulphuric acid is pumped through this layer so that it washes away any crossed-over methanol before it reaches the cathode. This fuel cell is called a flowing electrolyte-direct methanol fuel cell (FE-DMFC), which is shown in Figure 4. The main drawback of this design is the increased ohmic resistance between the electrodes, which is a result of the increased ionic resistance associated with the flowing electrolyte and the addition of a second PEM layer.

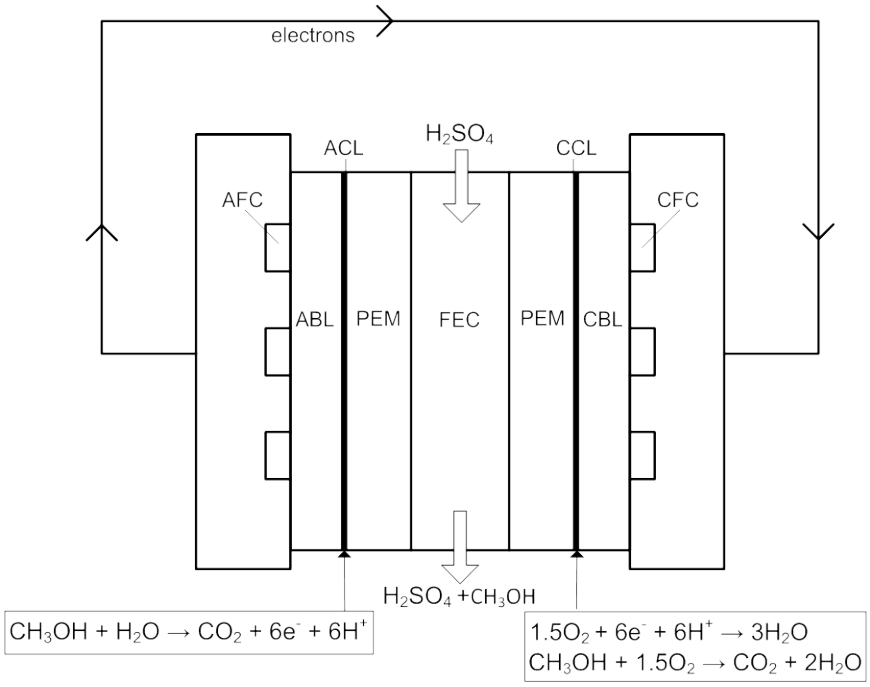

Figure 4 - FE-DMFC schematic and reactions

The increased ohmic resistance associated with the FE-DMFC is a drawback, as is the increased complexity and safety concerns associated with pumping and containing corrosive sulphuric acid. In addition, the flowing electrolyte may increase the rate of

methanol transport into the electrolyte through convection. However, these may be outweighed by the potential benefits, which are summarized here:

- Although methanol is convected into the flowing electrolyte channel, virtually all of the crossed-over methanol may be removed from the cell before reaching the cathode catalyst layer, virtually eliminating this electrochemical short circuit.
- PEMs may be made thinner since the FEC is responsible for methanol crossover prevention.
- With a suitably high flow rate of electrolyte, the methanol crossover may be virtually eliminated with a relatively thin FEC; if both the PEMs and FEC are made very thin the ionic resistance may not be significantly more than in a DMFC.
- Higher concentrations of methanol may be supplied without high losses due to methanol crossover; this will improve the reaction rate in the anode.
- Higher temperatures, which decrease the activation losses, will affect methanol crossover losses less severely.
- Cathode catalysts would be more effective without being poisoned by reacting methanol in the cathode.

In order to prevent the two PEM layers from collapsing inward, the flowing electrolyte layer (or channel) may include a spacer composed of a porous material that provides the necessary structural support, while allowing the sulphuric acid to flow within. This has proven to be necessary in the FE-DMFC design tested by Sabet-Shargi [11], which is very similar to the design used in this research. Without the porous spacer

in the flowing electrolyte channel, the two PEMs tend to bulge inwards and may contact each other, providing a pathway for methanol crossover to bypass the flowing electrolyte channel.

In the original flowing electrolyte concept proposed by Kordesch *et al.* [10], it was proposed that the used flowing electrolyte could be continuously circulated back and reused. However, this would cause the performance of the cell to gradually decrease while in operation due to the increasing amount of methanol in the flowing electrolyte that would cause the amount of crossover to increase. To avoid these concerns, only a FE-DMFC where the used flowing electrolyte is discarded is considered in this study. Although outside the scope of this research, a potential use of this discarded mixture of sulphuric acid and methanol could be as fuel for another fuel cell in order to increase the fuel usage efficiency.

1.3.2 Components of a FE-DMFC

The following section is a description of the components of a FE-DMFC design. Figure 5 shows an image of a FE-DMFC with parts labeled.

Current Collectors: At either end of the fuel cell assembly are the current collectors, which are flat plates that are intended to provide good surface contact with the backing plates. This is necessary both to provide even clamping pressure, and for good electrical contact between the current collectors and the backing plates. The current collectors must be conductive; they are therefore often made of a conductive metal such as copper, and may be coated in gold for excellent conductivity at the surface.

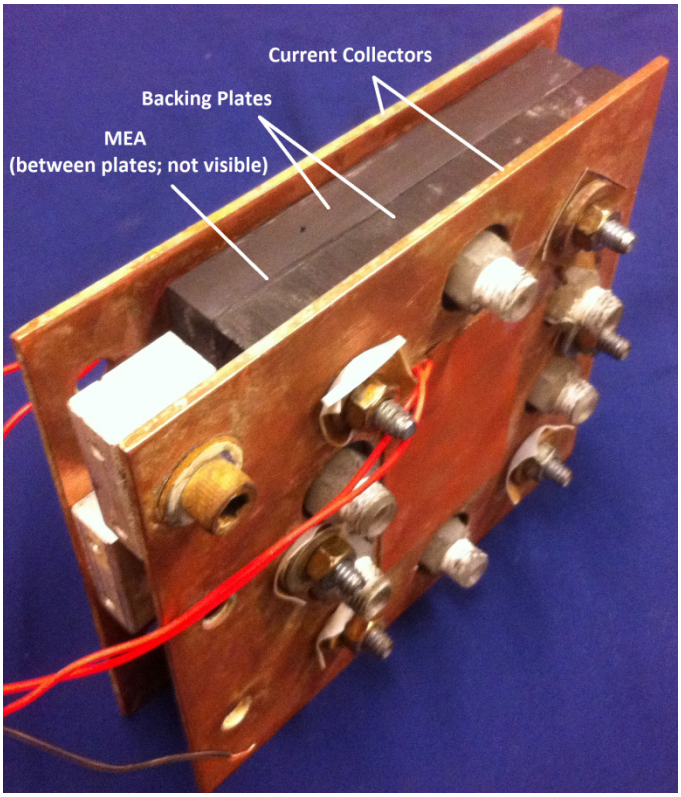

Figure 5 - Flowing Electrolyte – Direct Methanol Fuel Cell

Backing Plates: The backing plates are two solid flat plates at both the anode and cathode. They allow the delivery of the reactants to the backing layers through flow channels carved on their surfaces in contact with the backing layers. The flow channels also carry the excess reactants and waste products from the backing layers to the flow channel outlets. The electrons must also be transported between the backing layers and the current collectors, so the backing plates must be electrically conductive and have good contact with both the backing layers and the current collectors. They must therefore be made of a conductive material such as a metal or graphite.

Membrane Electrode Assembly (MEA): The membrane electrode assembly is a term that refers to all the thin layers contained between the two backing plates. A diagram of the components of a MEA in a FE-DMFC is shown in Figure 6.

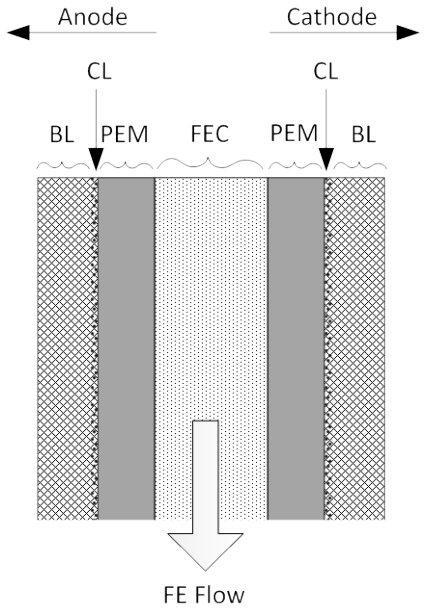

Figure 6 - Diagram of a membrane electrode assembly (MEA) in a FE-DMFC

The MEA consists of:

- **Backing Layers (BL) or Diffusion Layers:** The backing layers are porous layers required to allow the reactants to be transported from the flow channels to the catalyst layers, and to be distributed evenly. The waste products of the reaction must also be transported from the catalyst layers to the flow channels. Using hydrophilic materials in the anode can encourage the permeation of methanol and water reactants and the rejection of carbon dioxide waste, while hydrophobic materials in the cathode can encourage the permeation of oxygen reactant and the rejection of water product [1]. In addition, the backing layers must be electrically

conductive to allow for the transport of electrons consumed or produced in the reactions. Carbon paper or carbon cloth is commonly used. Both consist of fine strands of carbon; carbon cloth is woven while carbon paper is has more random orientation of strands.

- **Catalyst Layers (CL):** The anode and cathode catalyst layers are thin layers at the interfaces between the backing layers and PEMs where the reactions take place. In these regions, the backing layer is coated with microscopic dispersed catalyst particles, and is fused to the PEM. Platinum and ruthenium are used in the anode, and platinum is used in the cathode.
- **Membrane Layers:** The anode and cathode membrane layers each consist of a PEM on either side of the flowing electrolyte channel. In a regular DMFC, only one membrane layer is required since there is no flowing electrolyte channel. The membrane must allow hydrogen ions (protons) to pass through, while preventing electrons from passing, so that the electrons must go through the external current and provide useful electrical energy. The most commonly used membrane material is called Nafion®, and will be discussed in Section 1.3.3.
- **Flowing Electrolyte Channel (FEC):** This layer is the distinctive feature of a FE-DMFC, and separates the anode and cathode MEAs. It consists of an electrolyte, such as sulphuric acid, that is pumped through a porous spacer between the two PEM layers. It is conductive to proton transport, allowing the hydrogen ions to be transported from the anode to the cathode, while washing crossed-over methanol away in the outlet flow. Since the transport of methanol, unlike ions, is affected mainly by diffusion and convection, but not significantly

by electrochemical forces, the methanol is much less successful at crossing the FEC than the ions are.

1.3.3 Proton Exchange Membranes

The PEM must be a specialized material that is conductive to ions, while highly resistant to electrons, and also ideally impermeable by methanol. The most commonly used PEM material for DMFCs and FE-DMFCs is Nafion®, a highly specialized material, whose structure is illustrated in Figure 7.

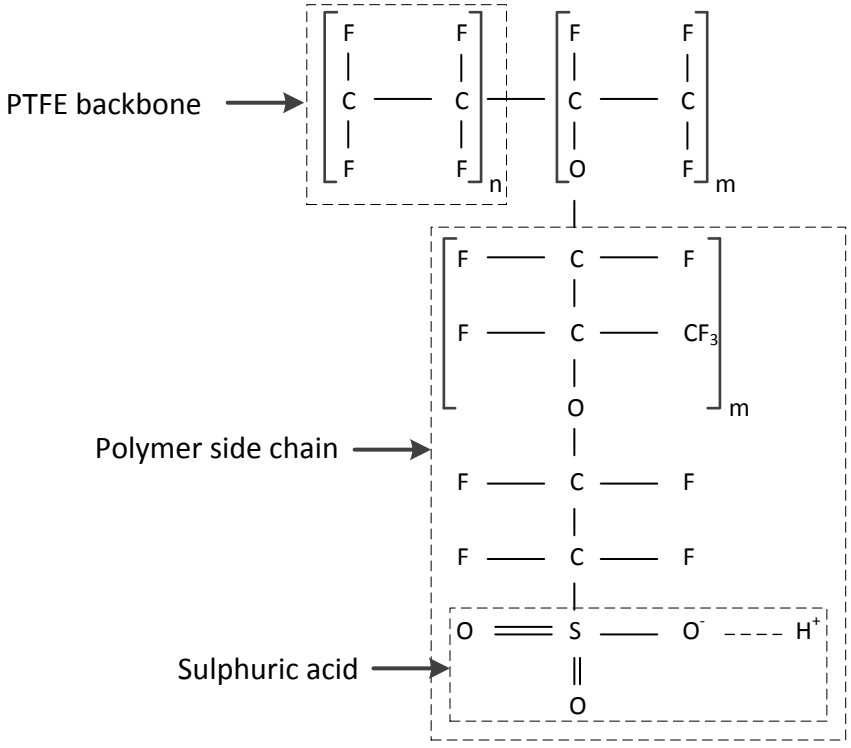

Figure 7 - Nafion® structure, adapted from Jiao and Li [12]

Nafion® membranes are composed of polymeric fibres that have a backbone of polytetrafluoroethylene (PTFE), and side chains with sulphate groups (SO_3^-). Because the PTFE is hydrophobic, it is naturally a good barrier to water permeation. However, the sulphate groups are hydrophilic, so tiny groups of water molecules tend to cluster by these sulphate groups inside the membrane, since water is capable of diffusing through theses voids in the membrane. A Nafion® membrane is said to be hydrated when it is fully saturated with these clusters of water molecules around the sulphate groups; hydration is necessary for the mechanisms of proton transport to function effectively [12].

There are two main mechanisms for proton transport through a Nafion® membrane. The first involves the positively-charged protons being attracted to the negatively-charged sulphonic acid groups, and becoming weakly attached to them, as shown by the dotted line connecting the proton to the sulphate group in Figure 7. Since this attraction is weak, and the proton is compelled to move across the membrane by electro-osmosis, the proton 'hops' from one sulphonic acid group to the next in order to cross the membrane [12].

The second mechanism of proton transport through the membrane happens when protons bond with water to form compounds such as hydronium (H_3O^+). Then the hydronium molecule can be transported through the membrane along with the diffusing water, while also driven by electro-osmosis. This mode is called vehicular transport, and water molecules tend to be 'dragged' through the membrane as well. In addition, methanol, which is soluble in water, also tends to be dragged along with the water, which is partially a cause of methanol crossover [12].

A common naming convention for commercial Nafion® membranes involves three digits. The first two digits represent the equivalent weight (molecular mass of Nafion® per sulphonic acid group) in hundreds of grams. The third digit represents the thickness of the membrane in mils (thousandths of an inch) [13]. For example a Nafion® 115 membrane has an equivalent weigh of 1100 g and has a thickness of 0.005 inches.

1.4 Fluid Dynamics Modelling and Porous Domains

The flowing electrolyte channel is a particularly intriguing aspect of the FE-DMFC design because its design and performance is distinctive and critical to the concept of a FE-DMFC. The modelling of the FEC for the purpose of hydrodynamic studies using computational fluid dynamics (CFD) is complicated by its porous nature. In this section, a brief overview of CFD and porous modelling is given.

1.4.1 Computational Fluid Dynamics

CFD is a branch of fluid mechanics that uses numerical algorithms, usually performed by a computer, to solve the behavior of fluid flow. The details of the scenario of interest must be set up by a user; this includes geometry, boundary conditions, fluid type and properties, and initial conditions. Many commercial CFD software packages are available; in this study, CFX-13.0 (ANSYS Inc.) is of interest.

The finite volume method (FVM) is a common approach for CFD programs, and is used in CFX-13.0. It involves dividing the domain into a number of smaller sub-domains, each centred on a node, and then solving the discretized governing equations for each of these volumes iteratively. The main governing equations are the continuity

(mass conservation) equation and the Navier-Stokes equations (momentum conservation), as shown below.

Continuity:

$$\frac{\partial \rho}{\partial t} + \nabla \cdot (\rho \mathbf{U}) = 0 \quad (2)$$

where ρ is the fluid density, t is time, and $\mathbf{U}$ is the velocity vector.

Navier-Stokes:

$$\frac{\partial}{\partial t}(\rho \mathbf{U}) + \nabla \cdot (\rho \mathbf{U} \times \mathbf{U}) = \mathbf{S_M} - \nabla P + \nabla \cdot \boldsymbol{\tau} \quad (3)$$

where $\mathbf{S_M}$ is the momentum source term, and P is the pressure. In addition, the term τ is the stress tensor, calculated as:

$$\boldsymbol{\tau} = \mu(\nabla \mathbf{U} + (\nabla \mathbf{U})^T - \frac{2}{3}\delta \nabla \cdot \mathbf{U}) \quad (4)$$

where μ is the fluid dynamic viscosity.

In addition, energy equations and turbulence equations must be considered. A turbulence model must be selected for turbulent flows; however, no turbulence equations are required for laminar flow. An energy equation is also required except in entirely isothermal cases. For low speed flows (not approaching the order of Mach speed), the full energy equation is not necessarily required, but the thermal energy equation may be suitable:

$$\frac{\partial (\rho h)}{\partial t} + \nabla \cdot (\rho \mathbf{U} h) = \nabla \cdot (\lambda \nabla T) + \boldsymbol{\tau} : \nabla \mathbf{U} + S_E \quad (5)$$

where h is enthalpy, λ is thermal conductivity, and S_E is an energy source.

Finally, equations of state for the fluid must be considered in a CFD problem. One convenient way of accounting for this when the fluid is water (in any phase) is to use the International Association for the Properties of Water and Steam (IAPWS) database. This

database allows the solver to look up the desired properties (enthalpy, specific heat, density, viscosity) at the current conditions [14].

1.4.2 Porous Modelling

Modelling a porous domain such as the flowing electrolyte channel presents additional challenges. A porous domain is one that has small voids throughout that fluid may travel through. For a domain to be modelled porous, it is assumed that the characteristic dimensions of the pores are much smaller than the characteristic dimensions of the domain.

The full porous model that is used is a generalization of the Navier-Stokes equations (which govern fluid flow) and Darcy's law (which governs fluid flow in porous regions at the macroscopic level). It involves modifications to all terms in the governing equations and the inclusion of a momentum source term to account for the effects of porosity [14].

Porosity, γ, is defined as:

$$\gamma = \mathrm{V}'/\mathrm{V} \tag{6}$$

where V is the physical volume of the domain, and V' is the volume in the domain that the fluid occupies. Essentially, porosity is the fraction of the total volume that the fluid occupies in a porous domain.

In addition, an area porosity tensor, K, is defined by:

$$\mathbf{A}' = \mathbf{K} \cdot \mathbf{A} \tag{7}$$

where $\mathbf{A}'$ is the vector area available to flow in the infinitesimal vector control surface $\mathbf{A}$. $\mathbf{K}$ is a tensor, and its purpose is to define the porosities of differently-oriented cross-

sections. In an isotropic model, it is simply a diagonal matrix with the porosity, γ, along the diagonal [14].

The mass and momentum governing equations are versions of those presented in Equations 2 and 4, modified to account for a porous domain. They are, respectively:

$$\frac{\partial}{\partial t}\gamma\rho + \nabla \cdot (\rho \mathbf{K} \cdot \mathbf{U}) = 0 \tag{8}$$

$$\frac{\partial}{\partial t}(\gamma\rho\mathbf{U}) + \nabla \cdot (\rho(\mathbf{K} \cdot \mathbf{U}) \times \mathbf{U}) = \gamma \mathbf{S_M} - \gamma\nabla P + \nabla \cdot \boldsymbol{\tau} \tag{9}$$

where the stress tensor is now defined as:

$$\boldsymbol{\tau} = (\mu \mathbf{K} \cdot (\nabla \mathbf{U} + (\nabla \mathbf{U})^T - (2/3)\delta \nabla \cdot \mathbf{U})) \tag{10}$$

Note that time-derivative terms are zero for steady state conditions. The thermal energy equation is not modified for porous domains apart from the altered stress tensor term given above.

For an isotropic model, a component of the momentum source term is defined as:

$$(S_M)_x = -\mu U_x K_{perm} - (\rho/2) K_{loss} |\mathbf{U}| U_x \tag{11}$$

where K_{perm} and K_{loss} are the permeability and loss coefficients, respectively, for the porous domain. This equation is given for the arbitrary Cartesian x-direction, but the equations for the y- and z-directions are identical, but with y or z in place of the x-subscripts [14].

The permeability coefficient, also simply referred to as the permeability, can be thought of as the ability of the porous domain to allow fluid to pass through. In other words, a material with a high permeability allows fluid to flow through with very little hindrance, while a material of low permeability severely hinders (reduces momentum) of fluid passing through. The loss coefficient is related to the inertial losses of the fluid because of the porous domain. The loss term is negligible in extremely low speed flows

on the order of a Reynolds number of 1 (using the pore dimension as the characteristic length to calculate Reynolds number) [14].

The permeability is a useful number that is used in Darcy's Law, a simple but important equation for fluid flow in a porous medium. Given the fluid viscosity and the medium's permeability, Darcy's Law can be used to relate the flow rate to the pressure drop over a given distance. It is stated as follows:

$$q = -K_{perm}\Delta P/(\mu L) \quad (12)$$

where q is the fluid volume flux and L is the thickness of the porous material in the direction that the fluid is travelling. Darcy's Law is phenomenological, meaning that it was developed empirically, but is consistent with fundamental theory; in fact, it can be derived from the Navier-Stokes equations by considering inertial forces to be negligible, and assuming that the viscous resisting force is linearly related to fluid velocity.

Note that the velocities in the above governing equations of porous media are specified as superficial velocities instead of true velocities. The distinction between the two is illustrated in Figure 8. When fluid is travelling from an arbitrary point A to point B, the superficial velocity is the distance between point A and point B (in a straight line) divided by the time elapsed. The true velocity, however, is the actual distance travelled from point A to point B (including all twists and turns that occur as a result of the porous medium) divided by the elapsed time. The superficial velocity is more convenient to characterize in porous media equations, and should be assumed to be referenced whenever velocity is mentioned in this study unless otherwise specified [14].

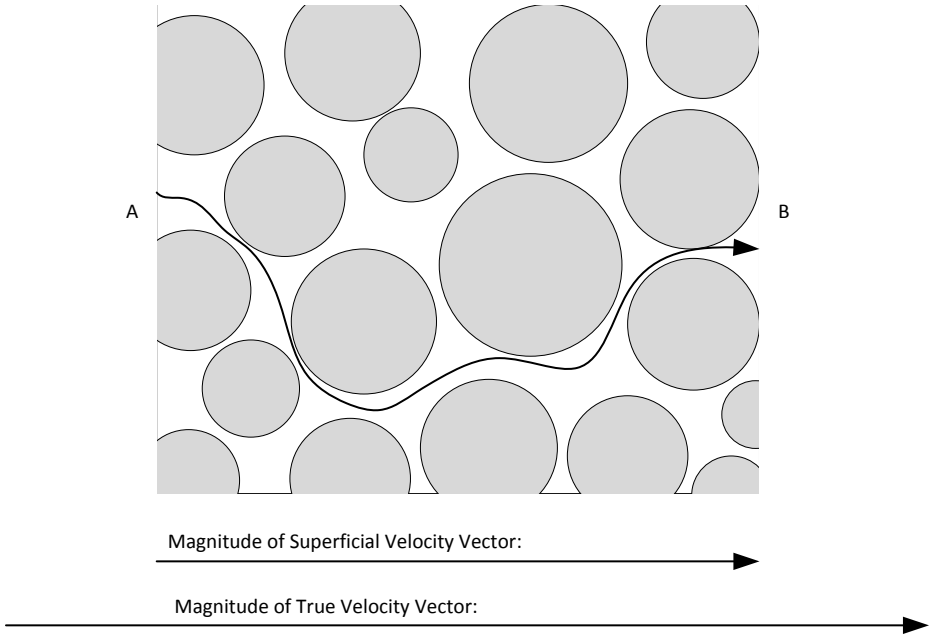

Figure 8 - Illustration of a fluid particle path in a porous medium showing the difference between superficial and true velocities

2 Chapter: Literature Review

2.1 FE-DMFC Modelling Studies

Fuel cell modelling is very useful because the performance of fuel cells with variable design parameters and operating conditions can quickly be simulated. This can provide a lot of insight into a variety of areas without investing the substantial time and equipment costs that would be required for experimental studies. In addition, simulation results allow for detailed analysis and isolation of the contributions of various operating parameters or sources of inefficiency. However, fuel cell modelling is very complex due to the intricate combination of fields such as electrochemistry, chemistry, thermodynamics, and fluid dynamics. This makes the pursuit of accurate models very difficult. In this section, relevant information from selected modelling studies related to FE-DMFCs is presented.

While models of DMFCs are relatively plentiful [15, 16, 17, 18, 19], models of FE-DMFCs are comparatively rare. In the limited amount of numerical modelling of FE-DMFCs that has been done to date, a FE-DMFC with a porous flowing electrolyte layer has rarely been fully represented. Often, fluid behaviour in the flowing electrolyte layer has been modelled as a fluid domain with an assumed parabolic velocity profile [20, 21, 22], similar to Poiseuille flow, or sometimes as a uniform (constant velocity) flow.

A numerical simulation was conducted by Cai *et al.* [20] of a DMFC with an electrolyte that was liquid, but not flowing; it therefore did not wash away crossed-over methanol. Only diffusive and electro-osmotic transport of methanol was modelled, while convective transport was ignored, and the liquid electrolyte was not considered to be a porous domain.

Kjeang *et al.* [21] created a rare 3D numerical computational fluid dynamics model of a FE-DMFC that did, in fact, have a flowing electrolyte channel. It therefore took into account convection-diffusion in the flowing electrolyte channel, unlike the liquid electrolyte fuel cell study by Cai *et al.* [20] previously mentioned. However, the flowing electrolyte was again not considered to be a porous domain, and a parabolic velocity profile similar to Poiseuille flow was assumed. In this model, dilute sulphuric acid was assumed to have fluid properties identical to water, and the thickness of edge effects was considered to be on the order of the flowing electrolyte layer thickness. The flow was also considered to be laminar, as the Reynolds number was between 0.5 and 10 for all cases considered. It was found that methanol crossover can be reduced by as much as 90% by a FE-DMFC, and crossover can be minimized by making both the flowing electrolyte layer thickness and the flow velocity higher. However, it was suggested that increasing the velocity rather than the thickness would be preferable, since the ohmic resistance increases with channel thickness.

Another study that also included a flowing electrolyte channel was a 1D [22] and a 2D [23] model by Colpan *et al.* of a FE-DMFC that included a porous spacer in the flowing electrolyte layer, with an assumed porosity of 0.6. Convective transport was not modeled in the 1D study. Similar to Kjeang *et al.* [21], a parabolic velocity profile similar

to Poiseuille flow was assumed in the flowing electrolyte channel. Colpan *et al.* [22] concluded that the power output could be increased by using a very high electrolyte flow rate and a very thin FEC.

A recent study by Ouellette *et al.* [24] did, in fact, fully model the flowing electrolyte channel of a FE-DMFC as a porous domain, including modelling of diffusion, convection, and electro-osmosis. A flat velocity profile in the FEC as a result of the porous domain was also assumed. This was a 1-dimensional, steady state, multiphase mixture performance model of a FE-DMFC. This study included an investigation of the effects of the flowing electrolyte channel's porous material properties (porosity and permeability) on methanol crossover. A noticeable increase in crossover current density was observed with increasing porosity, with the rate of increase becoming progressively lower. The crossover current density was observed to decrease only by about 2% as the permeability increased by several orders of magnitude. From the standpoint of reducing methanol crossover, therefore, a beneficial design for the flowing electrolyte channel would be with a lower porosity, with the selection of permeability being much less important. Specifically, Ouellette *et al.* suggested a porosity of 0.25 and a permeability of 10^{-9} m^2.

2.2 FE-DMFC Experimental Studies

While fuel cell modelling is useful for quickly evaluating the effects of a wide range of variables, experimental studies are also useful. They provide verification for models and reveal issues that may not have been properly addressed by models. In this section, a selection of relevant experimental studies related to FE-DMFCs is discussed.

As with modelling studies, experimental studies of DMFCs [25, 26, 27, 28] are much more common than experimental studies of FE-DMFCs. Though not a FE-DMFC study, Ravikumar and Shukla [29] investigated the effects of methanol crossover in a DMFC and found that for methanol concentrations under 2 M, crossover was negligible, but caused significant losses as the methanol concentration exceeded 2.5 M. Du *et al.* [30] confirmed the hypothesis that methanol crossover causes catalyst poisoning at the cathode, and observed that this effect was more pronounced at higher current densities and methanol concentrations. The concept of the FE-DMFCs is investigated in order to address this significant issue of methanol crossover.

Although rare, a few experimental studies involving flowing electrolyte fuel cells have been conducted. The flowing electrolyte fuel cell concept has been experimentally demonstrated in membraneless micro fuel cells [31], alkaline fuel cells [32], and direct methanol fuel cells [11, 33].

Kordesch *et al.* [10] proposed and demonstrated a DMFC with a circulating sulphuric acid electrolyte; however, their experimental cell did not utilize PEMs, but rather exposed the flowing electrolyte channel directly to the catalyst layers. It was concluded from their work that the concept of a flowing electrolyte in a DMFC did indeed reduce methanol crossover, as was intended.

A study on FE-DMFCs by Sabet-Shargi *et al.* [11, 33] involved a fuel cell design using a sulphuric acid flowing electrolyte in a channel of porous polyethylene. Experiments were conducted to determine the impact of membrane thickness, channel thickness, and concentrations and flow rates of methanol, air, and flowing electrolyte. It was recommended in this study that a porous spacer should be used in the FEC to prevent

the PEMs from contacting each other. In the previously-mentioned study by Kjeang *et al.* [21], it was suggested that increasing the flowing electrolyte velocity rather than the thickness would be the preferable method of reducing methanol crossover since channel thickness increases the ohmic resistance. In this experimental study by Sabet-Shargi [11], it was confirmed that this increase in ohmic resistance is indeed significant; therefore, keeping the flowing electrolyte channel as thin as reasonably possible is recommended. It was also observed in this study that thinner PEMs (Nafion® 212 as opposed to 115) resulted in better performance when used in conjunction with a flowing electrolyte channel, and higher electrolyte flow rates reduced the methanol crossover.

A study by Kablou [34] included experimental analysis of a FE-DMFC stack, which is a set of fuel cells (5 in this case) connected in series to increase the voltage for the same current density. The cell design was similar to the single cell design used by Sabet-Shargi [11]. Kablou's study experimentally investigated the effects of temperature, methanol concentration and flow rate, and flowing electrolyte and air flow rates. Among the conclusions of this study were that the flowing electrolyte channel does indeed reduce methanol crossover, and that increasing the flowing electrolyte flow rate significantly improves performance by reducing methanol crossover.

A study by Ouellette *et al.* [35] investigated a FE-DMFC design based on Sabet-Shargi's [11] and Kablou's [34] fuel cell designs, but using formic acid as the electrolyte instead of sulphuric acid. The effects of temperature, acid concentration, and methanol concentration were investigated. Again, the flowing electrolyte channel was found to be effective at reducing methanol crossover; however, the lower conductivity of formic acid compared to sulphuric acid posed a challenge.

2.3 Porous Modelling and Permeability Measurement

Many examples of fluid dynamics modelling of porous domains can be found in literature, including advanced cases such as moving boundaries with chemical reactions [36], coupled with fracture mechanics equations [37], involving a radially heterogeneous medium [38], among others. Studies have been conducted on porous mass transport in fuel cells, specifically in the gas diffusion layer (backing layer) [39, 40]. No studies, however, have been found that specifically investigate the hydrodynamics of a porous flowing electrolyte channel.

The permeability of a material is an empirically-defined quantity based on the material's resistance to fluid flow. However, it is sometimes useful to have equations to relate the permeability to the physical structure of the porous medium, particularly with regards to modelling fluid flow in a porous domain. One such useful semiheuristic relation proposed by Rumpf and Gupte that is intended to estimate the permeability of a bed of packed spheres with a narrow size distribution for creeping flows is presented here:

$$K_{perm} = \frac{\gamma^{5.5}}{5.6} d^2 \tag{13}$$

where d is the mean sphere diameter. This equation is reported to have good agreement with experimental results for porosities in the range of 0.35 to 0.67 [41].

The permeability of a porous material is typically determined by experimentally measuring the pressure drop of fluid flowing through the material at a known flow rate, and using Darcy's Law (Equation 12) to then determine the permeability. This is demonstrated in a number of literature sources, including some studies of fuel cell diffusion layers [42, 43].

2.4 Research Objectives

DMFCs are a developing technology, and FE-DMFCs are a sub-category of DMFCs that has been barely explored by comparison. DMFCs may be a part of a sustainable and viable energy sector in the future, with particular suitability for portable applications such as vehicles and electronics. FE-DMFCs are a novel concept that, with development and research, may be an improvement over standard DMFCs and make methanol fuel cells a more attractive technology. The potential of FE-DMFCs stems from their promising ability to reduce methanol crossover, which has been a significant barrier preventing DMFCs from approaching their theoretical efficiencies and power densities.

Therefore, this research is conducted with the aim of developing the design and operation of a FE-DMFC, so that this technology can gain efficiency, practicality, and power density, and eventually realize its potential applications. In particular, the flowing electrolyte channel, as the defining feature of a FE-DMFC, has received very little detailed analysis. This research will aim to model the hydrodynamics of the flowing electrolyte channel, and experiment with different design parameters and operating conditions in order to better understand the fluid behavior in the FEC and make recommendations for improved design. In particular, the effects of the FEC's thickness and porous properties, temperature, and flow rate will be explored.

Furthermore, performance testing of a FE-DMFC will be conducted, with the aim of determining the impact of the design parameters and operating conditions explored in the modelling studies. This will aid in verifying the recommendations of the modelling studies for improved design.

Finally, permeability is an important measure for the porous spacer and features prominently in the modelling and experimental studies; however, it is a fairly uncertain quantity that is not readily known for material samples. Therefore, experimental studies will be performed in order to more accurately determine the permeability of porous material samples, which will be compared to theoretical values.

In summary, the main objectives for this research are:

- to better understand the hydrodynamics in a flowing electrolyte channel through fluid dynamics modelling, including exploring the effects of varying thickness, porous properties, flowing electrolyte flow rate, and temperature, so that design recommendations can be made;
- to verify that these design recommendations improve the performance of a FE-DMFC by experimentally operating a fuel cell and observing the effects of the design parameters and operating conditions of interest; and
- to experimentally verify that the estimates for the permeabilities of the porous spacers are reasonable.

2.5 Contributions

The main contribution of this study is to improve FE-DMFC design by:

- providing insight into the hydrodynamic behaviour of the flowing electrolyte in a FE-DMFC to aid in future modelling and design studies;
- making recommendations regarding operating conditions and design parameters of the flowing electrolyte channel for better fuel cell performance;

- making recommendations regarding the porous properties of the flowing electrolyte channel spacer for better fuel cell performance while minimizing the pressure drop of the channel; and
- providing insight into the accuracy of estimates for the permeability of porous spacers.

3 Chapter: Flowing Electrolyte Channel Modelling

The flowing electrolyte channel is a unique feature of the FE-DMFC and is critical to its performance, yet the hydrodynamics of the porous flowing electrolyte channel have not been specifically explored in any great detail in any known studies. Therefore, it is beneficial to model the flowing electrolyte channel using computational fluid dynamics software, and explore the effects of various design parameters and operating conditions. This chapter will detail the setup and results of this model.

3.1 Modelling Setup

In the limited amount of numerical modelling of FE-DMFCs that has been done to date, a FE-DMFC with a porous flowing electrolyte layer has not been fully represented. Instead, fluid behaviour in the flowing electrolyte layer has been modelled as a fluid domain with an assumed parabolic velocity profile, similar to Poiseuille flow, or as a uniform (constant velocity) flow. For this study, the flow of sulphuric acid in the porous media is simulated as a porous region using CFX-13.0 (ANSYS Inc.) software to determine a more realistic velocity profile. It is examined how this profile changes as the volume flux, flowing electrolyte channel thickness, temperature, and porous material properties are modified. In addition, pressure drop is also examined as these parameters change, since the pumping power required to drive the flow of electrolyte is also of

interest. Note that this study focuses specifically on the hydrodynamic behaviour of the flowing electrolyte channel, while the electrochemical performance is outside of the scope. However, this study is intended to make recommendations for the design and operation of a flowing electrolyte channel that effectively reduces methanol crossover without drastically increasing the ohmic resistance, which will directly improve the electrochemical performance of a FE-DMFC.

The gravitational pressure drop is not factored into these results; however, it can be expected to reduce all estimated pressure drops consistently by approximately 0.5 kPa for an elevation reduction of 5 cm along the flowing electrolyte channel.

Several assumptions are made in modelling the hydrodynamic behaviour of sulphuric acid flow in the flowing electrolyte channel of a FE-DMFC. The domain is considered to be isotropic and porous. The fuel cell is assumed to operate at 80°C (for the base case), and have a 5-cm by 5-cm active area, with a flowing electrolyte channel of the same size. The sulphuric acid is assumed to have properties identical to water, as was assumed in the previously-mentioned 3D numerical model [21]. The flow is considered to be laminar. The edge effects are assumed to be very small, so the model is 2D. In addition, the flow of crossed-over methanol and water is considered to be very low, such that the presence of methanol does not significantly affect the fluid properties or alter the flow patterns of the flowing electrolyte. In a practical system, the flowing electrolyte flow rate should be intentionally selected to be much higher than the expected crossover flow rate so that crossed-over methanol is effectively removed. The effects of the crossed-over methanol in a practical FE-DMFC are therefore more relevant to the electrochemical behaviour of the cell, which is not explored in this study, than to the

hydrodynamic behaviour of the flowing electrolyte channel. The anode and cathode PEM interfaces are modelled as no-slip boundaries. Flow of constant mass flux is injected into the inlet, and the outlet is considered to be at zero average gauge pressure. An illustration of the modelling domain described is given in Figure 9.

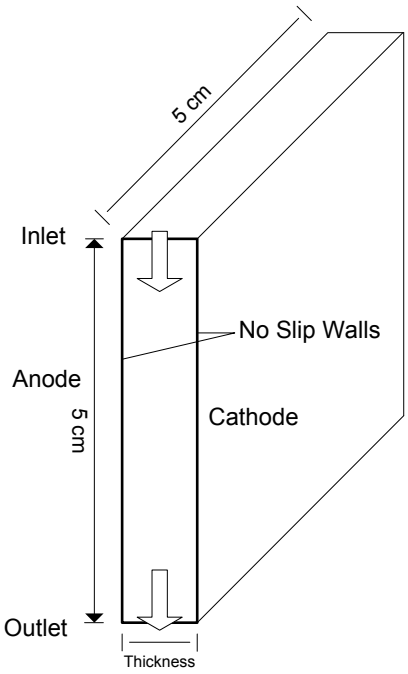

Figure 9 - Illustration of Modelling Domain

The assumption that diluted sulphuric acid has properties identical to water depends on the molarity of the solution. Dilute sulphuric acid is typically used in FE-DMFC experiments, usually with a concentration of 2 M (10.7% by mass) or less. Even at higher molarities of around 3.5 M, this assumption causes no property discrepancy greater than 25% (for dynamic viscosity) [44].

The assumption of laminar flow can be justified by calculating the Reynolds number using the characteristic dimension of the porous structure (70 μm), the properties

of water at 80°C, and the base volume flux of 10 mL/min/(75 mm^2), which is equivalent to superficial velocity. The result is a very low Reynolds number of 0.43; for the largest characteristic porous dimension used in this study (100 μm) the Reynolds number is 0.61.

The values of the permeability and loss coefficients of the porous spacer are derived from images obtained from a Scanning Electron Microscope (SEM) of the porous spacer material (porous polyethylene, Figure 10) used in experimental studies related to this research [11, 24, 34]. From these images, the permeability coefficient is estimated from Equation 13, which is applicable to creeping flow through a bed of packed spheres, which can be considered similar to the structure of the porous polyethylene. It has already been presented as:

$$K_{perm} = \frac{\gamma^{5.5}}{5.6} d^2$$

where d, the mean sphere diameter, is estimated from Figure 10 by manual measurement to be 70 μm [41].

In addition, the porosity is estimated to be 0.5 by Ouellette *et al.* [24] using a liquid saturation method, which estimates the porosity by comparing the dry weights of porous spacers to their weights when saturated with liquid. It is possible that the porosity of a porous spacer may be lower in the interior than near the edges, since boundaries tend to reduce the packing density (while increasing the porosity) of a bed of packed spheres. A higher porosity near the boundaries would effectively increase the permeability, since the fluid would preferentially travel through this pathway of least resistance. In Chapter 5, experimentally measured permeability values are compared to values calculated from this model of packed spheres; any significant disagreement between these values might suggest that this reduction of porosity at the boundaries is a concern.

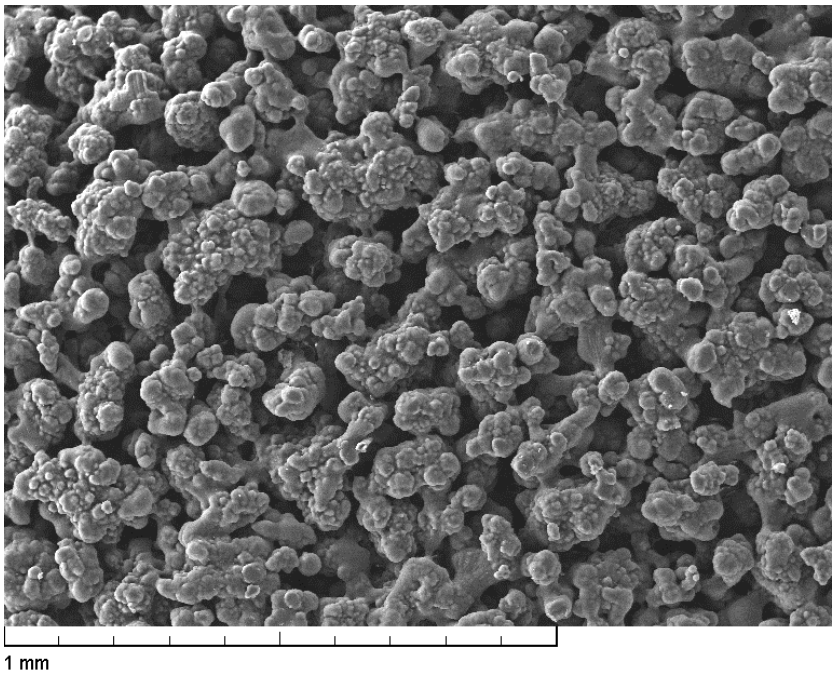

Figure 10 - SEM image of porous polyethylene structure [24], used by permission

The estimated permeability coefficient is therefore calculated as 1.9×10^{-11} m^2. However, it is questionable whether or not modelling a porous spacer as a bed of packed spheres provides an accurate estimate of the actual permeability of a spacer, since the microscopic structures are not truly spherical, and could have a wide size distribution. For this reason, in Chapter 5 experiments are conducted to determine the actual permeability of porous spacers, and compare them to theoretical estimates obtained from this packed sphere model.

The loss coefficient, also known as the inertial coefficient, is related to the inertial losses of the fluid due to the presence of the porous material. Since this flow has a Reynolds number of less than 1 for the operating conditions of this study, calculated using a characteristic length of the porous material's typical sphere diameter (which is

appropriate for classifying flow characteristics within a porous medium), the inertial effects are negligible. Therefore, the loss coefficient is considered to be zero.

For this study, the effects of independently varying the flowing electrolyte volume flux, channel thickness, and porous material properties are examined. In ANSYS CFX, the porous domain characteristics can be modified by inputting values for the porosity and permeability. The studies related to varying the porous material properties are conducted by two different approaches: by varying the porosity and permeability directly, and by varying the porosity and sphere diameter. Since permeability is a function of porosity and sphere diameter, as shown in Equation 13, in the second approach modelling the different values of porosity and sphere diameter is accomplished by calculating the appropriate permeability associated with the desired combination of porosity and sphere diameter. Varying the parameters in this way gives a better sense of the effects of changing the directly-controllable physical properties of the porous material. A summary of the base case parameters for the simulations can be found in Table 1.

Table 1 - Summary of base case parameters for simulations

Parameter	Symbol	Units	Value	Comments
Temperature	T	°C	80	
Length	L	cm	5	Length of active area in streamwise direction
Width	w	cm	5	Width of active area
Dynamic viscosity	μ	Pa·s	-	Automatically varied with operating conditions from IAPWS library
Density	ρ	kg/m^3	-	Automatically varied with operating conditions from IAPWS library
Inlet flow rate	Q	mL/min	10	
Porosity	γ	-	0.5	
Permeability	K_{perm}	m^2	$1.9x10^{-11}$	Corresponds to a porosity of 0.5 and a sphere diameter of 70 μm
Loss Coefficient	K_{loss}	m^{-1}	0	Negligible inertial losses

When varying the porosity values, it is necessary to consider what values are realistic or possible. The maximum packing density (fraction of total volume occupied) of an infinite bed of close-packed spheres is approximately. 0.74 [45]; since porosity can be obtained by subtracting the packing density from unity, this corresponds to a porosity of 0.26. Therefore, it would be unrealistic to use porosity values lower than 0.26 for this model. The lowest porosity simulated in this study is 0.3.

The maximum possible porosity of packed spheres is less well-defined. Certain sphere packing configurations can achieve much lower packing densities (and higher porosities), as observed in atomic packing configurations. For example, simple cubic structure (observed in polonium) achieves a packing density of 0.52 (porosity of 0.48). One of the least densely packed configuration is the diamond cubic crystal structure (observed in silicon, germanium, diamonds, and other materials), which achieves a packing density of approximately 0.34 (porosity of 0.66). While the configuration of spheres in porous spacers for fuel cells cannot be expected to behave as these crystal structures, it is nonetheless of note that mechanically stable configurations of equally-sized spheres exist with such high porosities.

Of course, the actual structure of the porous spacers is expected to more closely correspond to a random packing pattern rather than a repeating crystal structure. Rong et *al.* [46] used a discrete element method to simulate the random packing of equally-sized spheres with different porosities, and successfully achieved porosity values as high as 0.80 with mechanical stability. It was noted that the highest porosities were achieved when the cohesion forces between spheres were very high relative to gravitational forces. This is a plausible configuration for porous spacers, since the particles are in fact cohered

together for mechanical stability, and could theoretically be manufactured in an environment where gravitational forces are negligible (such as being immersed in a liquid in which the spacer material is neutrally buoyant). Finally, it is of note that the edges of the porous spacer may have a higher porosity than the interior, as discussed previously, which would increase the overall porosity of the spacer. Porosity values in this study do not exceed 0.7, which is within the range of porosities simulated in the study by Rong *et al.* The simulated porosity values also do not greatly deviate from the experimentally validated porosity range of Equation 13, which has been stated as 0.35 to 0.67, though both extreme values of simulated porosity should therefore be viewed with caution.

The mesh, or grid, in this study is structured and manually created, with significant inflation of the node densities near the walls and inlet, as shown in Figure 11. A fully implicit coupled solver is employed, using the finite volume method.

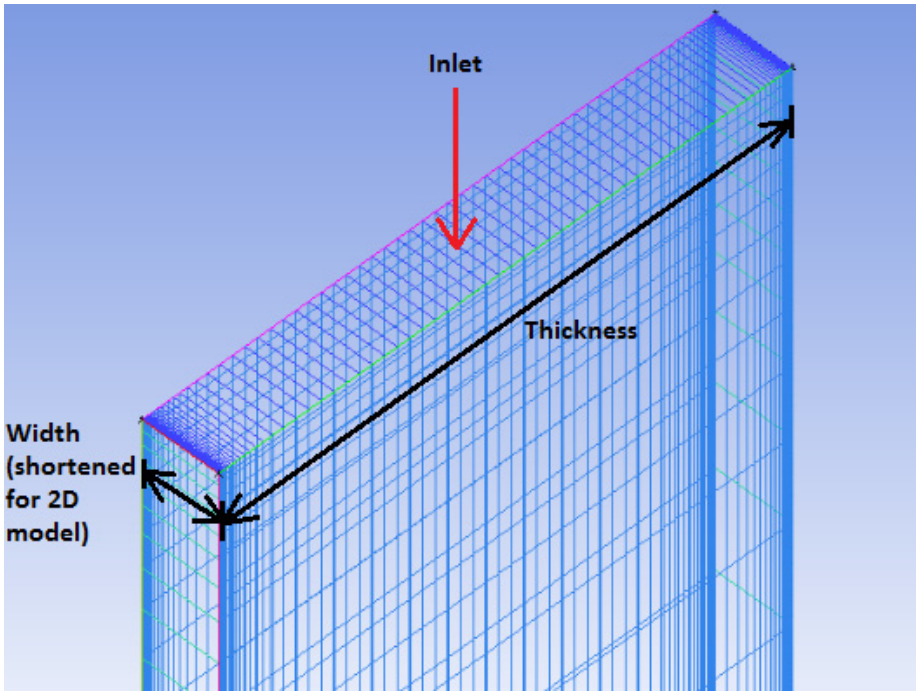

Figure 11 - Grid inflation at inlet

Note that the energy source in the thermal energy equation (Equation 5) is zero throughout this study due to the absence of any heating sources within the domain, and all time derivatives in all governing equations (Equations 5, 8-11) are zero because the simulations are steady state. The second term on the right side of the thermal energy equation accounts for viscous heating, which is negligible for the very low-speed flows in this study (as demonstrated by the low Reynolds number).

Because some of water's fluid properties vary over the range of temperatures used in this study (particularly viscosity and density by about 56% and 2.4% relative to room temperature, respectively), the fluid properties used in these equations must adapt to the appropriate values for the temperature of each individual finite fluid element at all times during the simulation. This is accomplished using ANSYS's capability to incorporate look-up table for water's fluid properties using IAPWS data.

The validity of the model can be confirmed by comparing the simulated pressure drops to an analytical pressure drop for a general porous domain, as calculated from Darcy's Law, which was given in Equation 12:

$$q = -K_{perm}\Delta P/(\mu L)$$

3.2 Results of Modelling Study

3.2.1 Grid Convergence Analysis

A grid convergence analysis was conducted using three grids. For this analysis, a 1.5 mm channel was used with a flow rate of 10 mL/min, a permeability of 1.9×10^{-11} m^2, and a porosity of 0.5. Figure 12 shows the pressure drop across the domain and the maximum fluid velocity for each grid.

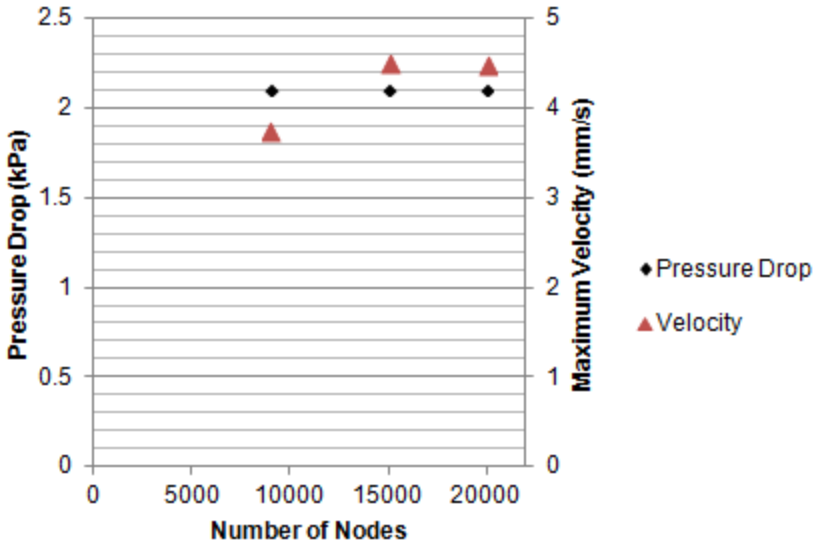

Figure 12 - Grid Convergence Study

It is shown in Figure 12 that the trends in both the pressure drop and the maximum velocity demonstrate convergence. The difference in pressure drop between the coarsest and the finest meshes is less than 0.2 % of the total pressure drop, and is less than 0.02% between the intermediate and finest meshes. For the maximum velocity, a significant difference of 16.8% is seen between the coarsest and intermediate meshes; however, the trend converges for the third mesh, demonstrating only a change of less than 0.0002% between the intermediate and finest meshes. Therefore, the finest grid is of sufficient node density, and is used for all of the subsequent analyses.

3.2.2 General Behaviour of Flow

Figure 13 shows the velocity profile over the channel thickness in the fully developed region of the channel for a channel thickness of 1.5 mm and a flow rate of 10 mL/min, which is used as a typical example of the flow behavior seen for most of the

conditions simulated in this study. Compared to a parabolic velocity profile that would be expected in a non-porous domain, results show that there is significant flattening of the velocity profile so that it is virtually constant except in a very small boundary region at either edge. The flattening of the profile is a result of the porous domain's tendency to act as a momentum sink, which is compounded by the fact that the flow has a very low Reynolds number, which means that there is very little momentum in the flow to resist the momentum-sapping effects of the porous domain. The thickness of each boundary layer, as defined by 95% of the maximum velocity, is only 0.019 mm, or about 1.2% of the thickness for the case of 10 mL/min/(75 mm^2) volume flux and a channel thickness of 1.5 mm, which is used as a typical example of flow behaviour. Therefore, when considering mass transport in a flowing electrolyte channel of similar size and with similar flow conditions, it appears that considering the velocity profile to be flat would be a reasonable approximation.

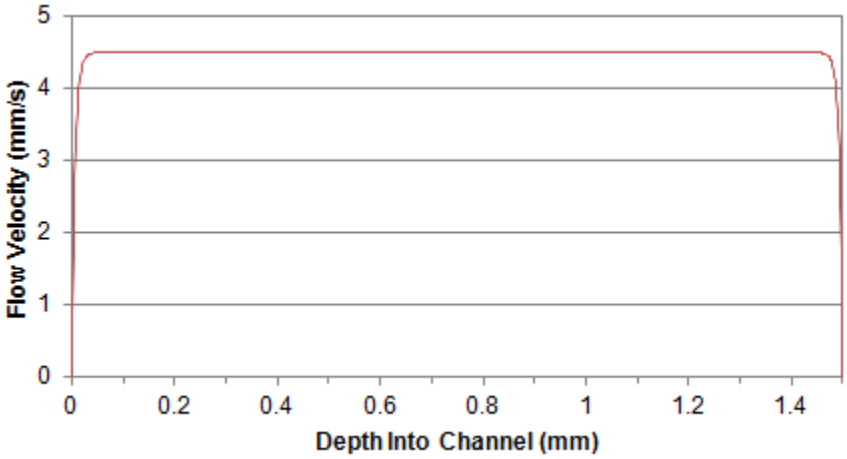

Figure 13 - Velocity profile in a 1.5 mm channel with a volume flux of 10 mL/min/(75 mm^2)

Note that the inlet volume fluxes for this report are hereafter given in units of mL/min/(75 mm^2), as 75 mm^2 is the inlet area of the original 1.5 mm channel model. The inlet velocity will therefore be constant across all channel thicknesses with equivalent volume fluxes.

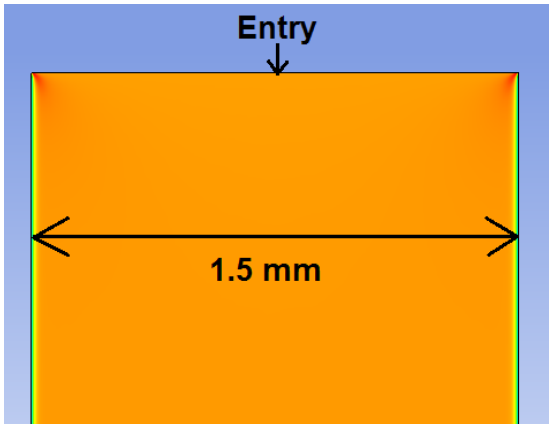

Figure 14 - Velocity contour plot of entry region for 1.5 mm channel with 10 mL/min/(75 mm^2)

(Red = higher; Blue = lower)

Figure 14 shows a contour plot of the velocity in the entry region for the same 1.5 mm channel with a flow rate of 10 mL/min/(75 mm^2). A velocity scale is not shown, as it is for qualitative analysis only. It can be seen that fully developed conditions exist after a very short distance, on the order of only 10% or less of the channel thickness, which, for this channel size, is less than 0.3% of the channel length. Therefore, it would likely be reasonable to ignore the entry effects when considering the mass transport in a flowing electrolyte channel. It is seen throughout the range of conditions simulated that the entry length is never significant. This result is not unexpected, since the very low inertia of the flow means that the flow should quickly be affected by the strong effects of porosity. In addition, the boundary layers are so thin that the vast majority of the flow

does not have to significantly change velocity or direction to accommodate the presence of the boundary layers.

3.2.3 Effects of Volume Flux and Channel Thickness

Figure 15 shows the fully developed velocity profiles across the channel thickness for varying volume fluxes, which were simulated at a channel thickness of 1.5 mm. The profile maintains the same flattened shape with very thin boundary layers for all volume fluxes. As expected, scaling the volume flux tends to scale the maximum velocity by the same amount. An analysis of the boundary layer thicknesses, defined by 95% of the maximum velocity, reveals that the thickness of the boundary layer changes by no more than 0.002% when the volume flux is changed within the range of 1 to 100 mL/min/(75 mm^2). Therefore, when considering the design of a flowing electrolyte channel, it would be reasonable to assume that the boundary layer thickness is independent of the volume flux, within or near this simulated range.

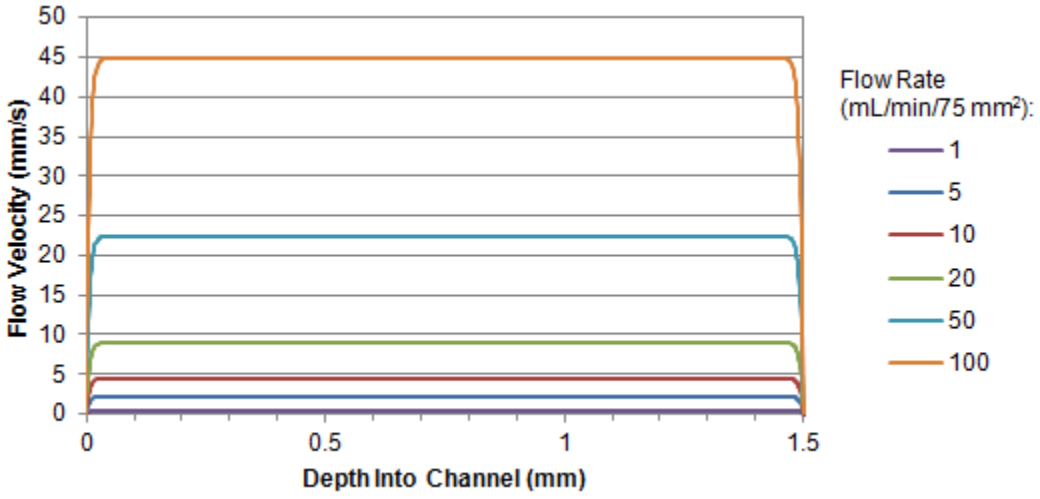

Figure 15 - Velocity profiles for varying volume fluxes at 1.5 mm

While boundary layers typically change size as the volume flux is varied, this is not the case for this problem. This is likely because the driving factor behind boundary layer characteristics is the competition between inertial and viscous forces. Since the Reynolds number is so low throughout the range of volume fluxes simulated, the inertial forces are so miniscule compared to the viscous forces that the interplay between viscous and inertial forces in the boundary regions is not significantly affected by the changing volume flux.

When varying channel thickness within the range of 0.05 to 2 mm with constant volume flux, the thickness of the boundary layer relative to the channel thickness increases with decreasing channel thickness, as shown in Figure 16. This is because the absolute boundary layer thickness does not change, so the fraction increases with decreasing channel thickness. Because the boundary layer occupies a larger fraction of the thickness for thinner channels, the maximum velocity increases slightly in order to maintain constant volume flux per unit thickness. When considering mass transport through the flowing electrolyte channel, it appears to be reasonable to assume that the boundary layer thickness is negligible as long as the channel thickness is significantly larger than the absolute boundary layer thicknesses seen in this study (which are each approximately 0.019 mm for all channel thicknesses and volume fluxes).

The independence of the boundary layer thickness from the channel thickness in this range is expected. Because the boundary layers are very thin compared to the channel thicknesses, the channel would have to be much thinner for the two boundary layers to begin affecting each other or for the maximum velocity to be significantly affected. It is not until the very lowest channel thickness simulated (0.05 mm) that the thickness of the

channel begins to have noticeable effects on the boundary layer thickness, which is likely an impractically low channel thickness, since the thinnest channels used in known studies are 0.61 mm.

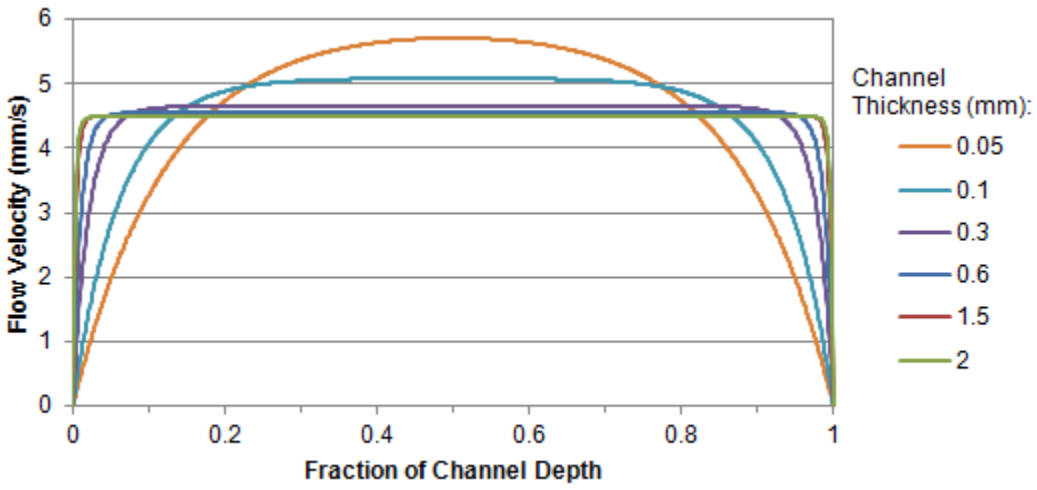

Figure 16 - Velocity profiles for varying channel thicknesses with a volume flux of 10 mL/min/(75 mm^2)

Figure 17 shows the pressure drops over the domain for various volume fluxes and channel thicknesses. The pressure drop is strongly dependent on the volume flux in a nearly linear fashion, as Equation 12 would predict. The channel thickness is not a major factor, since the porous domain has much more significant effects on the pressure drop than the viscous resistance of the walls, except for the very thinnest channels (which are likely impractically thin). Note that volume fluxes higher than approximately 20 mL/min/(75 mm^2) are significantly higher than those that have been experimentally tested in an FE-DMFC and are likely unnecessarily high.

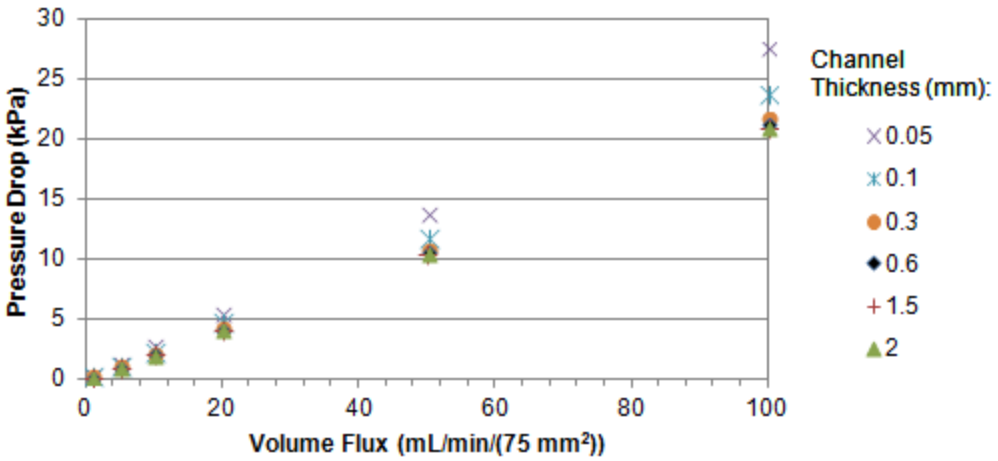

Figure 17 - Pressure drops for various volume fluxes and channel thicknesses

3.2.4 Effects of Porosity and Permeability

Figure 18 shows the boundary layer thicknesses for a 0.6 mm channel with an inlet volume flux of 10 mL/min/(75 mm^2) at various porosities and permeabilities. One trend seen in these data is that the boundary layer thickness decreases with increasing porosity at constant permeability. Another trend seen is that as the permeability decreases by an order of magnitude at a time, the boundary layer thickness also decreases, but by less than an order of magnitude. This result is expected since the permeability is a measure of the ability of porous materials to allow fluid to pass through. As such, a lower permeability more strongly resists the fluid flow, and therefore is a stronger momentum sink that more effectively flattens the velocity profile.

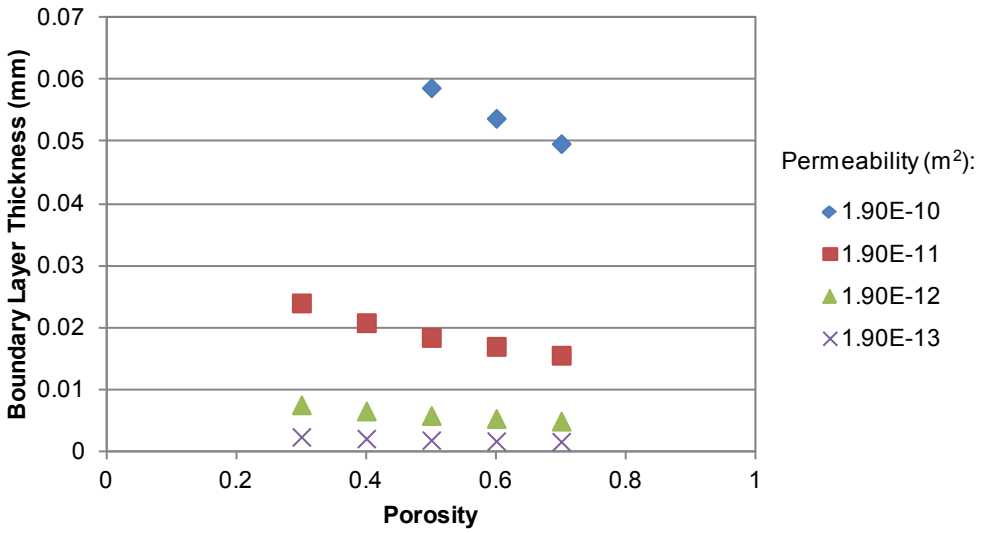

Figure 18 - Boundary layer thicknesses for various porosities and permeabilities in a 0.6 mm channel with a volume flux of 10 mL/min/(75 mm^2)

Note that similar trends were seen when varying porosity and permeability at other volume fluxes and channel thicknesses.

For a permeability of 1.90×10^{-10} m^2, it was found that the simulations failed to converge for porosities lower than 0.5. This is likely due to the fact that this combination of permeability and porosity implies a very large sphere diameter according to Equation 13; for example, the sphere diameter would be near 0.4 mm for a porosity of 0.4. This is only slightly smaller than the channel thickness of 0.6 mm, negating the assumption that the characteristic dimensions of the porous structure are much smaller than the width of the channel.

Figure 19 shows the pressure drops for various porosities and permeabilites for a 0.6 mm channel with an inlet flux of 10 mL/min/(75 mm^2). Consistent with Equation 12 (which is not a governing equation of the model, but defines a phenomenological relation

between permeability and pressure drop), the pressure drop increases by an order of magnitude as the permeability decreases by an order of magnitude, and is virtually independent of porosity as permeability remains constant.

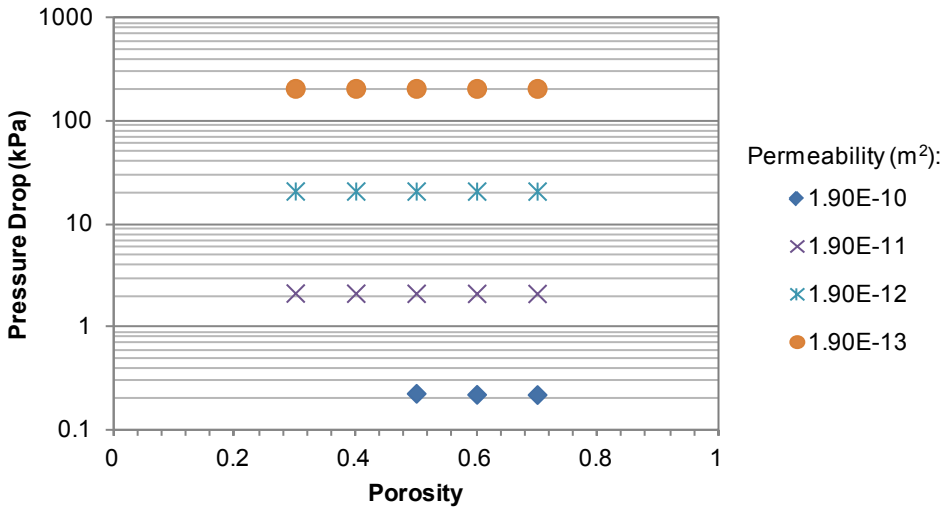

Figure 19 - Pressure drops for various porosities and permeabilities in a 0.6 mm channel with a volume flux of 10 mL/min/(75 mm^2)

3.2.5 Effects of Porosity and Sphere Diameter

In the previous investigation of varying porosity and permeability independently, it is not immediately apparent which data points represent porous materials that obey the assumption that the characteristic dimensions of the porous material are much smaller than the channel width. Therefore, an investigation is conducted where the more intuitively physically meaningful parameters, the porosity and sphere diameter, are varied independently. Note that varying the porosity and sphere diameter independently of each other affects permeability, since permeability is a function of both porosity and sphere diameter according to Equation 13.

Figure 20 shows the boundary layer thicknesses for a 0.6 mm channel with an inlet flow of 10 mL/min/(75 mm^2) at various porosities and sphere diameters. One trend seen in these data is that the boundary layer thickness increases with increasing porosity at constant sphere diameter, due to the associated increasing permeability. Similarly, the boundary layer thickness increases with increasing sphere diameter, also due to the associated increasing permeability.

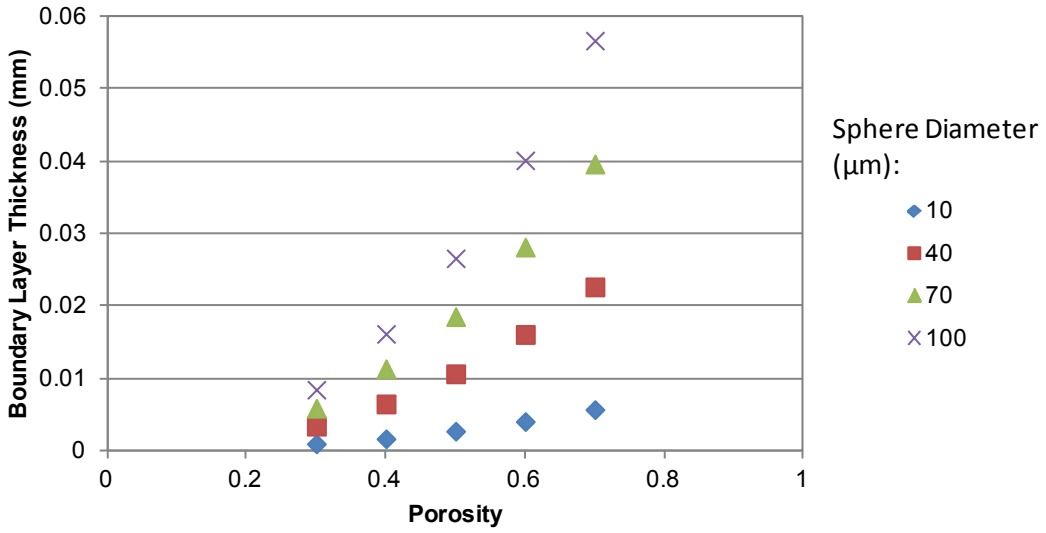

Figure 20 - Boundary layer thicknesses for various porosities and sphere diameters with a 0.6 mm channel and a volume flux of 10 mL/min/(75 mm^2)

Figure 21 shows the pressure drops for various porosities and sphere diameters for a 0.6 mm channel with an inlet flux of 10 mL/min/(75 mm^2). It is observed that the pressure drop decreases for increasing porosity and sphere diameters, due to the resulting increase in permeability. The effects of porosity and sphere diameter on permeability and pressure drop are very significant.

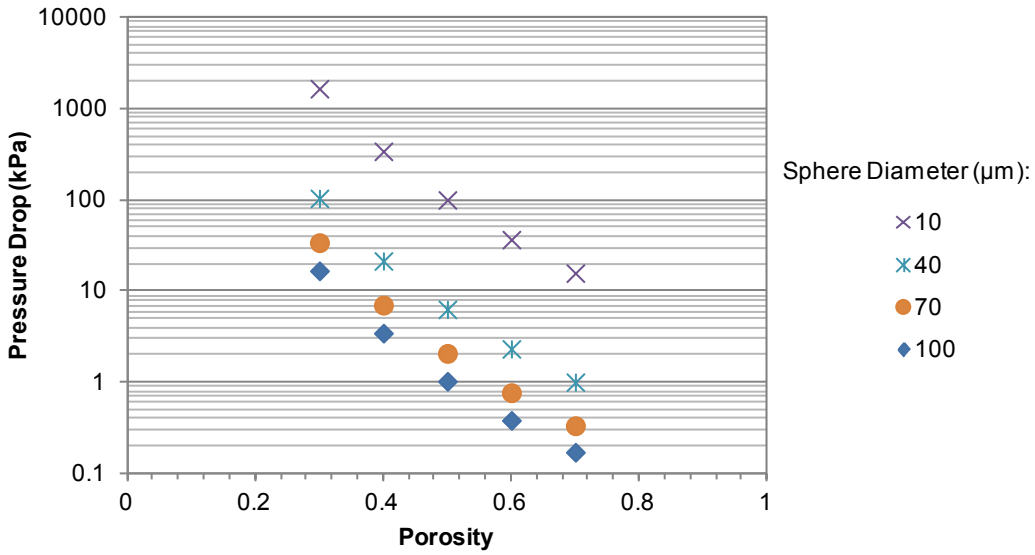

Figure 21 - Pressure drops for various porosities and sphere diameters with a 0.6 mm channel and a volume flux of 10 mL/min/(75 mm^2)

3.2.6 Non-Isothermal Simulations

It is also of interest to take into account the effects of heat transfer when the flowing electrolyte inflow and the fuel cell are not at the same temperature. The inlet temperature was varied at 10°C increments from 30°C to 80°C, and the fuel cell temperature was varied at 10°C increments from 60°C to 80°C.

These values were chosen because they represent a typical range of operation temperatures for DMFCs or FE-DMFCs, and simulate varying degrees of flowing electrolyte preheating from virtually none to fully equalized at fuel cell temperature. The resulting pressure drops can be seen in Figure 22 for a 0.6 mm channel with a volume flux of 10 mL/min/(75mm^2). Simulations were also performed for a volume flux of 20 mL/min/(75mm^2) for the same channel thickness, and for a 0.3 mm channel with a

volume flux of 10 mL/min/(75mm^2). Note that all volume fluxes are corrected to a temperature of 25°C, so that the mass flux is identical across different temperatures.

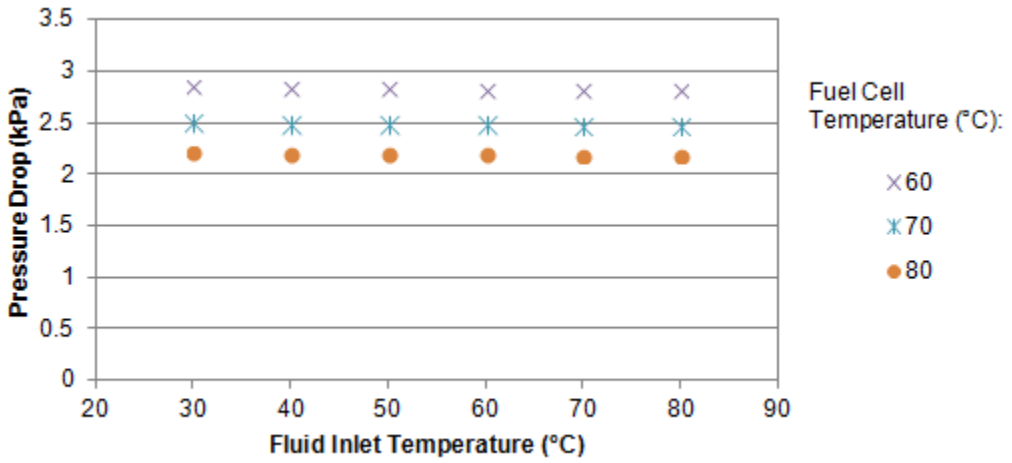

Figure 22 - Pressure drops for various fuel cell and electrolyte inflow temperatures for a 0.6 mm channel and a volume flux of 10 mL/min/(75 mm^2)

These results indicate that the fuel cell temperature is a major factor in pressure drop. The pressure drop is approximately 30% lower with a temperature increase from 60°C to 80°C. This is largely a result of the decreasing fluid viscosity at higher temperatures, which is shown in Figure 23. Conversely, the fluid inlet temperature has virtually no effect on pressure drop, which is because the fluid flux is small and is exposed to a large surface area of the channel walls, so that the fluid temperature is 90% heated to the fuel cell temperature within the first 5% of the channel length for all cases, as seen in Figure 24 for the case of the 80°C fuel cell. Another result of these simulations, not pictured, is that the velocity profiles and hydrodynamic behavior of the flowing

electrolyte channel in general, besides pressure drop, are negligibly different from isothermal simulations.

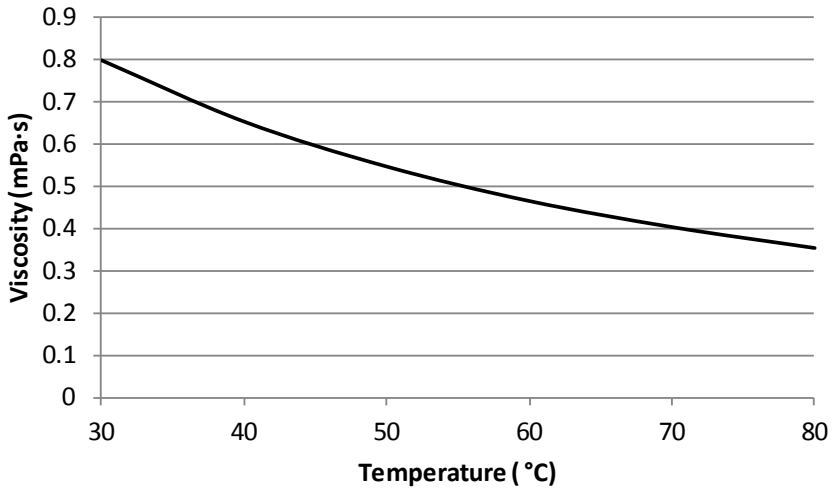

Figure 23 - Variation of the dynamic viscosity of water within the temperature domain

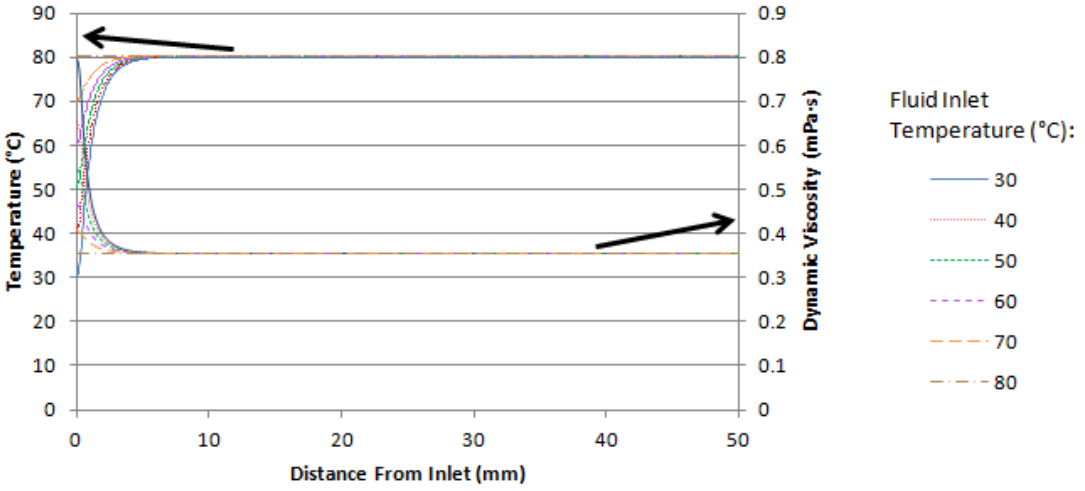

Figure 24 - Centreline fluid temperature and dynamic viscosity for various electrolyte inflow temperatures for a 0.6 mm channel with a volume flux of 10 mL/min/(75 mm^2) and a fuel cell at 80°C

Although not pictured, the effect of doubling the volume flux is to double the pressure drop, which is consistent with the observations in previous isothermal simulations. Halving the flowing electrolyte channel thickness does not have any noticeable effects on pressure drop, but shortens the distance required for the flow to equalize its temperature with the fuel cell temperature from about 5% to 1-2% of the channel length.

These non-isothermal simulations therefore suggest that fuel cell temperature is an important consideration when predicting pressure drop, with higher temperatures recommended to reduce pressure drop. Otherwise, temperature and non-isothermal effects do not significantly affect the hydrodynamic behavior of the flowing electrolyte channel.

3.2.7 Analytical Verification of Results

Using the form of Darcy's Law in Equation 12, estimates of pressure drop can be calculated and compared to the simulated pressure drops in the model. Darcy's Law in this form takes into account the permeability of the porous material, the fluid's dynamic viscosity, and the flow rate to predict the pressure drop in a porous medium. Since it does not take into account the pressure drop due to friction at the edges of the domain, the pressure drop from Darcy's Law is independent of the channel thickness. A comparison between the pressure drops from the model and from Darcy's Law for a variety of volume fluxes and channel thicknesses can be seen in Figure 25 for a porous medium with a porosity of 0.5 and a permeability of 1.90×10^{-11} m^2. It can be seen that Darcy's Law and the model are in agreement regarding the linear dependence of pressure drop on

volume flux. However, the model predicts an increase in pressure drop for thinner channels, while Darcy's Law does not account for channel thickness. This difference is only significant for impractically thin channels (0.1 mm or thinner). The difference is less than 5% for all channel thicknesses greater than 0.3 mm, and is smaller than 1% for a 2 mm channel. For these practical channel thicknesses, the model predicts the decreasing importance of channel thickness to pressure drop as the channel thickness increases. This is consistent with the expectation that the contribution of channel size should diminish relative to the contribution of the porous medium for practical channel thicknesses, since the velocity profile is expected to be fairly flat at the low Reynolds numbers experienced in these scenarios. There is therefore very little interaction (and very little further contribution to pressure drop) between the two boundary layers. Therefore, in these cases the model demonstrates a closer similarity to the expected physical behaviour than the solution of Darcy's Law, which does not account for viscous losses at the walls (PEMs).

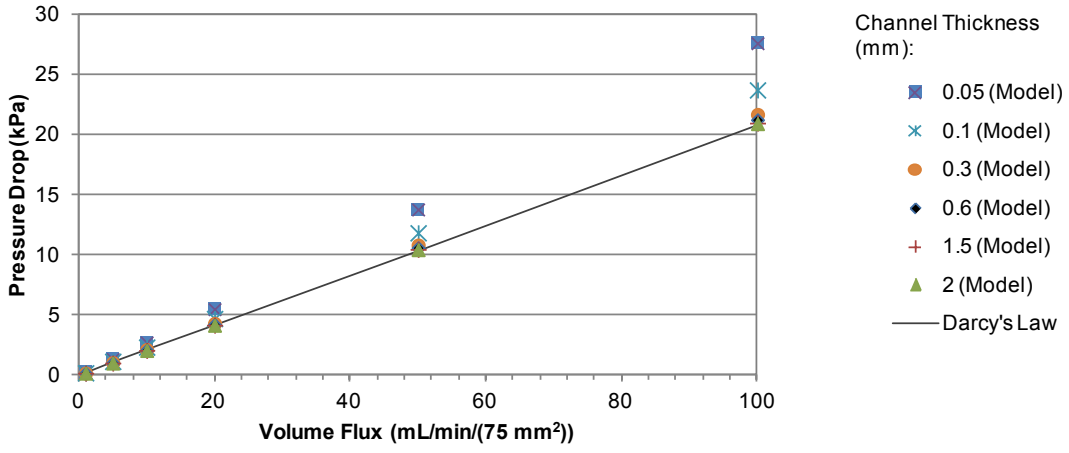

Figure 25 - Comparison between pressure drops predicted by Darcy's Law and by model for various volume fluxes and channel thicknesses

Overall, the approximation for pressure drop obtained from Darcy's Law, which takes into account the most significant source of pressure drop (the porous medium), suggests that the flowing electrolyte channel model in ANSYS CFX represents behaviours and results consistent with those that are expected.

Further verification of the model can be conducted by comparing the pressure drop predictions made by the model to those made by Darcy's Law when varying the properties of the porous domain, as shown in Figure 26. Darcy's Law predicts no relation between porosity and pressure drop at constant permeability; likewise, the model demonstrates very little effect of porosity on pressure drop. The pressure drop in the model also demonstrates the same inversely proportional dependence on permeability as Darcy's Law predicts. The error between the model and analytical results is not obvious in the figure due to the logarithmic vertical axis. It is, however, between 5 and 10% for the highest permeability (lowest pressure drop), and is lower than 3% for all other permeabilities, dropping below 1% for the lowest permeability value. This trend can be explained by the decreasing significance of the viscous pressure drop at the walls (which is not accounted for in Darcy's Law) relative to that due to the porous medium as the permeability becomes smaller. Therefore, in these cases the model also demonstrates a closer similarity to the expected physical behaviour than the analytical solution of Darcy's Law, which does not account for viscous losses at the walls (PEMs).

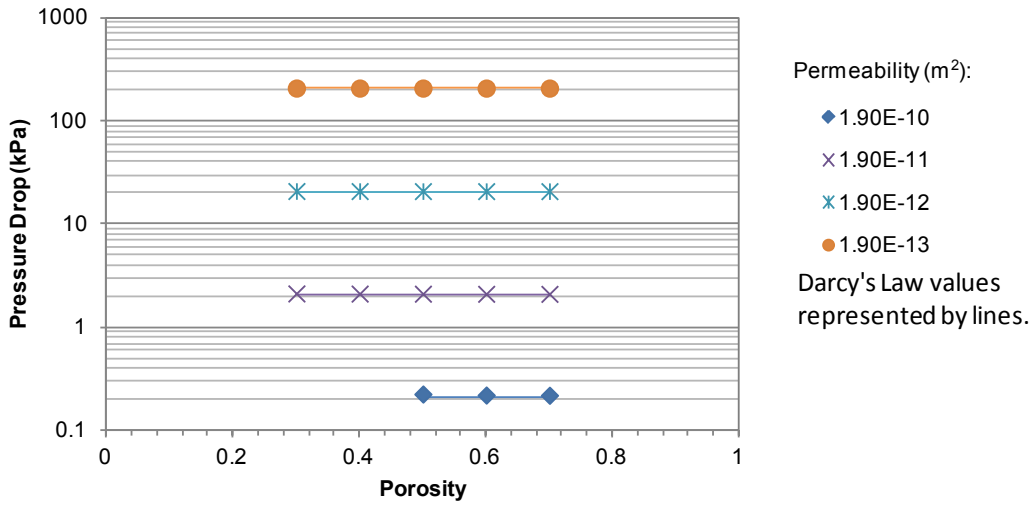

Figure 26 - Comparison between pressure drops predicted by Darcy's Law and by model for various porosities and permeabilities

3.2.8 Summary of Important Results

The most important results from the above sections can be summarized as follows:

- Velocity profile is very flat; boundary layers and entry length are negligible.
- Pressure drop increases nearly linearly with volume flux, and is largely independent of channel thickness; ohmic resistance can therefore be reduced with a thinner channel without adversely affecting the pressure drop.
- Permeability is the determining porous property for predicting pressure drop; a higher permeability reduces pressure drop significantly, while still maintaining a relatively thin boundary layer.
- Since permeability is a function of porosity and sphere diameter, increasing either will increase the permeability and reduce pressure drop; however, there are

practical limits to how high either of these values can reasonably be. For example, the sphere diameter must not approach the order of magnitude of the channel size, otherwise the porous domain model is invalid.

- To illustrate a potentially practical goal, a porosity of 0.5 to 0.6 with a sphere diameter of at least 40-70 μm (one order of magnitude smaller than the channel thickness) would achieve a permeability on the order of 10^{-11} m^2, which would limit pressure drop to less than 2 kPa.
- Pressure drop can also be reduced with higher cell temperatures; preheating the flowing electrolyte is unnecessary as it has little effect.
- Results tend to agree with expectations based on Darcy's Law.

4 Chapter: Fuel Cell Experimental Studies

The previous chapter detailed the hydrodynamic modelling studies conducted of the porous flowing electrolyte channel in a FE-DMFC, and a number of conclusions and recommendations were made. This chapter details the fuel cell experimental studies conducted to provide further insight into FE-DMFC performance and design.

4.1 FE-DMFC Components

In this section the components of the experimental fuel cell are detailed. This cell is manufactured in-house, and is the design created by Kablou [34] that was also used by Ouellette *et al.* [24], which is based on the design by Sabet-Shargi [11].

Current Collectors: Copper flat plate current collectors, shown in Figure 27, were used due to copper's good electrical conductivity. Each current collector is attached to an aluminum block for electrical connections, and has a heating pad adhered to maintain the active area of the fuel cell at the desired temperature. The thickness of each current collector is 3.2 mm.

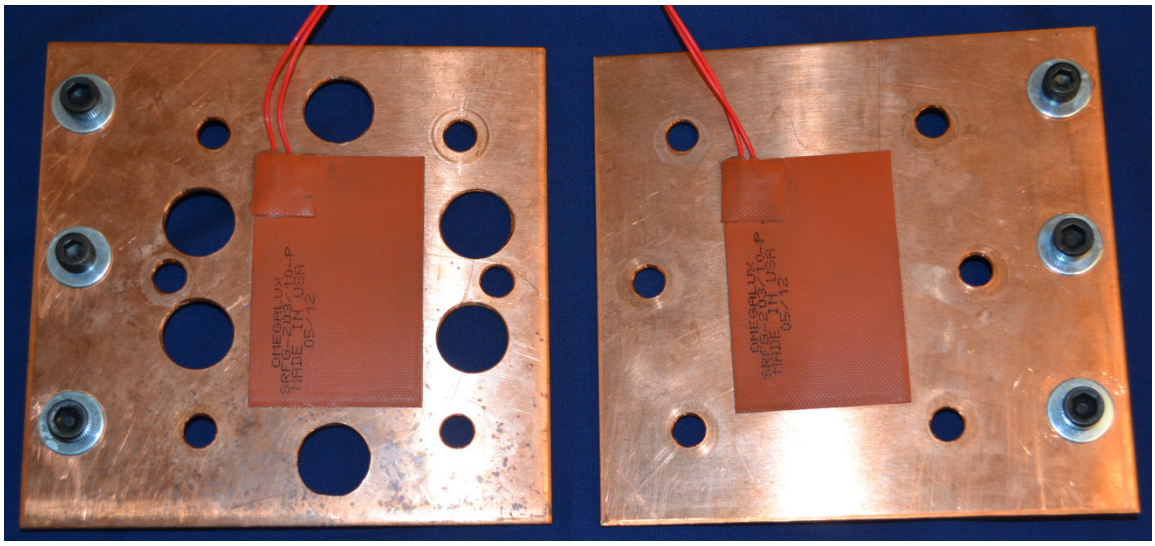

Figure 27 - Copper flat plate current collectors (Left: Anode; Right: Cathode)

Backing Plates: Graphite backing plates, one of which is shown in Figure 28, are used in this FE-DMFC. Graphite AR-08 is electrically conductive and relatively soft, allowing for flow channels and manifolds for reactants and electrolyte to be easily machined. An arrangement of seven parallel serpentine flow channels is used. Each flow channel has a square cross-section of 1.0 mm width, and the flow distribution area is a square with a 50 mm width. Drawings can be seen in Appendix B.

Backing Layers: The backing layers are commercially available fuel cell electrodes composed of carbon paper (TGP-H-090) and are sized at 50 mm by 50 mm, as shown in Figure 29. One side of each backing layer is coated with a fine dispersion of catalyst particles, which defines the thin catalyst layer at the interface. The anode catalyst loading is 2.0 mg/cm^2 of Pt; the catalyst loading for the cathode is 2.7 mg/cm^2 of Pt and 1.35 mg/cm^2 of Ru [11].

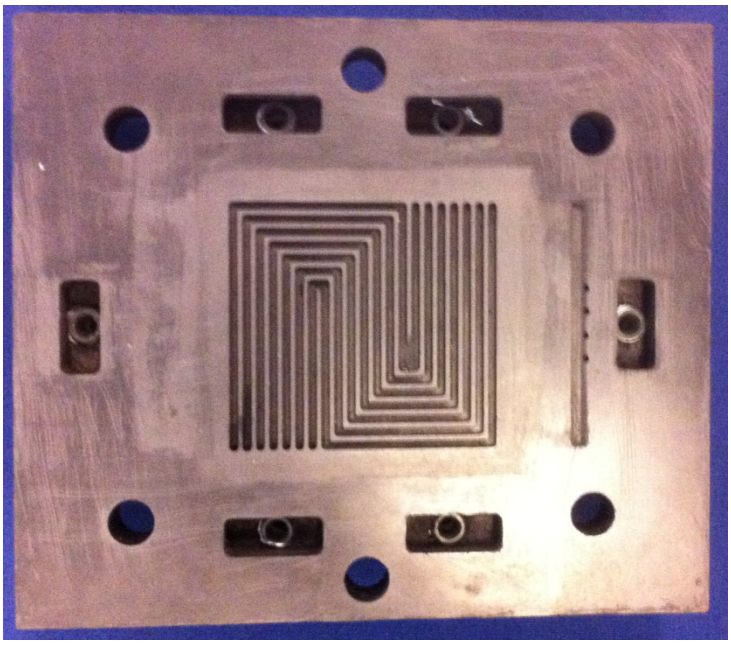

Figure 28 - Graphite backing plate

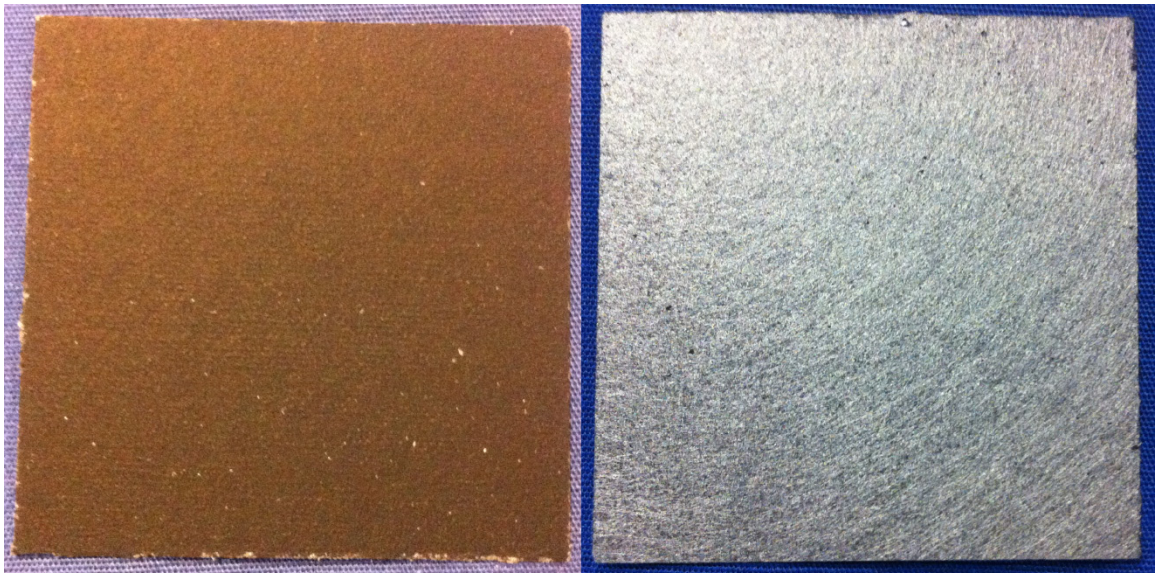

Figure 29 - Cathode carbon paper electrode (Left: Catalyst-coated side; Right: Backing layer side)

Proton Exchange Membranes: The anode and cathode PEMs, as shown in Figure 30, are composed of Nafion® 115, which is manufactured by DuPont, and has a thickness of 0.005" (approximately 0.127 mm). Nafion® 117 is thicker and commonly used in PEM fuel cells to reduce methanol crossover; however, Nafion® 115 was selected because a thicker membrane increases the ohmic resistance and is not necessary to reduce crossover when a flowing electrolyte is used. A membrane thinner than Nafion® 115, such as Nafion® 212, was not selected due to its fragility.

Figure 30 – A hydrated proton exchange membrane (PEM) Nafion® 115

Flowing Electrolyte Channel: The flowing electrolyte channel is composed of a hydrophilic porous spacer, as shown in Figure 31. Spacers with 35, 70, and 90 μm pore sizes were used, the former two of which were polyethylene (PE), while the latter of

which was polypropylene (PP). Both PE and PP are chemically resistant to sulphuric acid.

Figure 31 - Porous polyethylene spacer for flowing electrolyte channel

4.2 Experimental Setup and Procedures

4.2.1 Preparation and Assembly

Preparation of the cell for experimentation involved Nafion® hydration, heat pressing, and final assembly.

Nafion® hydration is a necessary process to ensure that the membranes have activated sulphate groups, are permeated with water, and are not contaminated. This process involves five stages; each stage involves submerging the membranes in a solution held between 80 and 100°C for one hour. The solutions for each of the five stages are:

1. Distilled water
2. Hydrogen peroxide (3% by volume) in distilled water, to remove organic contaminants
3. Distilled water

4. Sulphuric acid (0.5 M) in distilled water, to activate the sulphate groups
5. Distilled water

Following these five steps, the membranes are stored in distilled water at room temperature until they are assembled into the MEAs.

Each half-MEA is composed of a Nafion® membrane and a backing layer with catalysts. In a FE-DMFC, each cell contains an anode half-MEA and a cathode half-MEA that are separated by the flowing electrolyte channel; all of these together comprise the full MEA. At the catalyst layer, it is important that there is good contact between Nafion®, catalyst, and carbon paper in order to provide the most favourable environment for reactions to occur. That is why each MEA is heat pressed, fusing the Nafion® to the catalyst layer. A Carver Laboratory Press (Model 2697-5) is used to provide 3 MPa of pressure at 180°C for 3 minutes. See Figure 32 for an image of a heat pressed MEA. Note that an excessive size of Nafion® is used since the edges can later be trimmed.

The MEAs were attached to the graphite backing plates using PTFE tape, with holes cut through the tape at the manifolds, bolt holes, and active cell area, as shown in Figure 33. The two half-cells were then assembled with the porous spacer and a chemically-resistant 0.75 mm Viton gasket in between; the Viton gasket held the porous spacer in position at the active cell area, and provided a seal against the PTFE tape to prevent any fluid leakage, as shown in Figure 34. With the current collectors in place at either side of the cell, the assembly was held together by six M5 carbon steel threaded bolts, each wrapped in PTFE heat shrink to provide electrical insulation. A torque of 60 in·lb was used, since lower torques result in leakage and higher torques can crush the

electrodes. Both steel and electrically insulating Viton washers were used with the bolts, as well as hand-cut washers of PTFE sheet. The assembled cell can be seen in Figure 35.

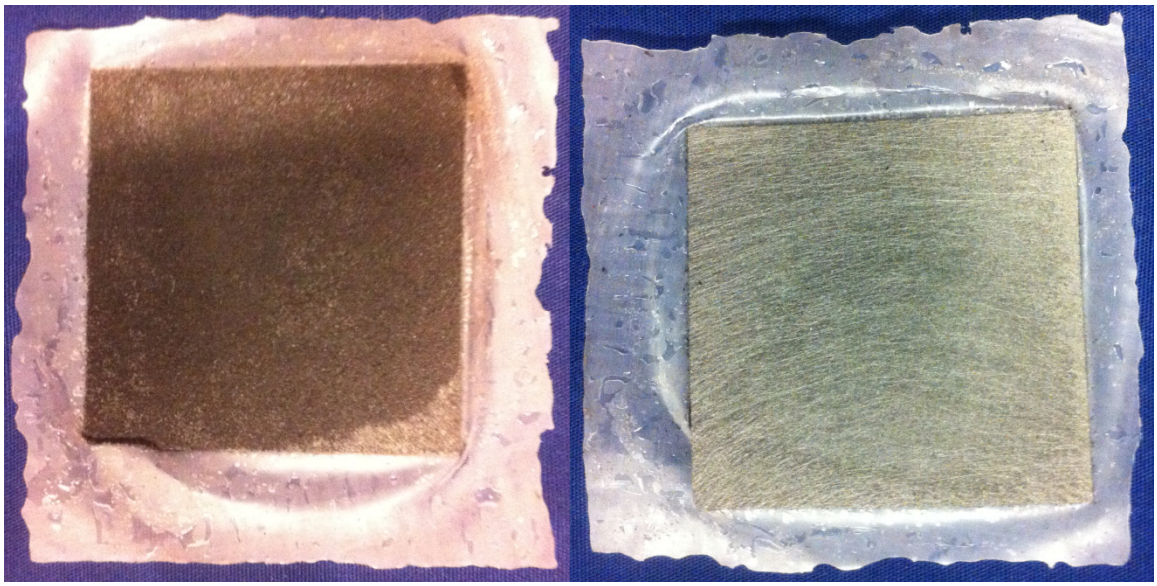

Figure 32 - Heat pressed MEA (Left: PEM side; Right: Electrode side)

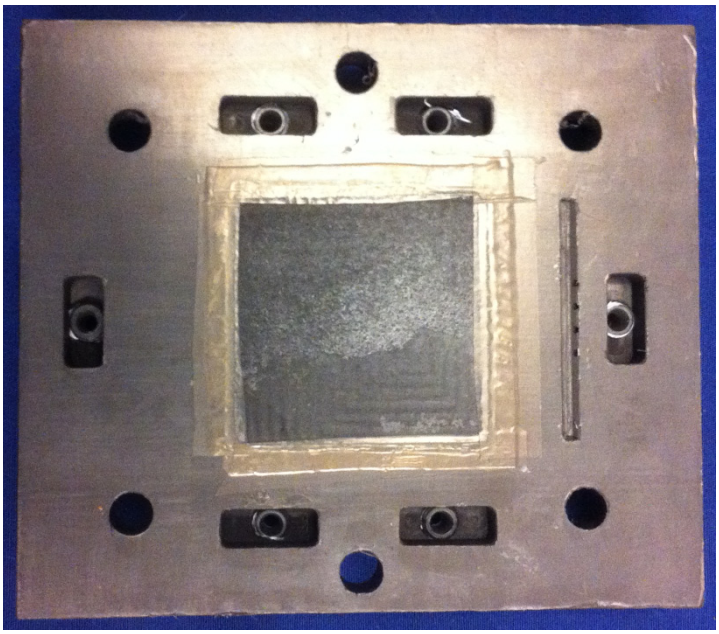

Figure 33 - Anode backing plate assembled with MEA and PTFE tape

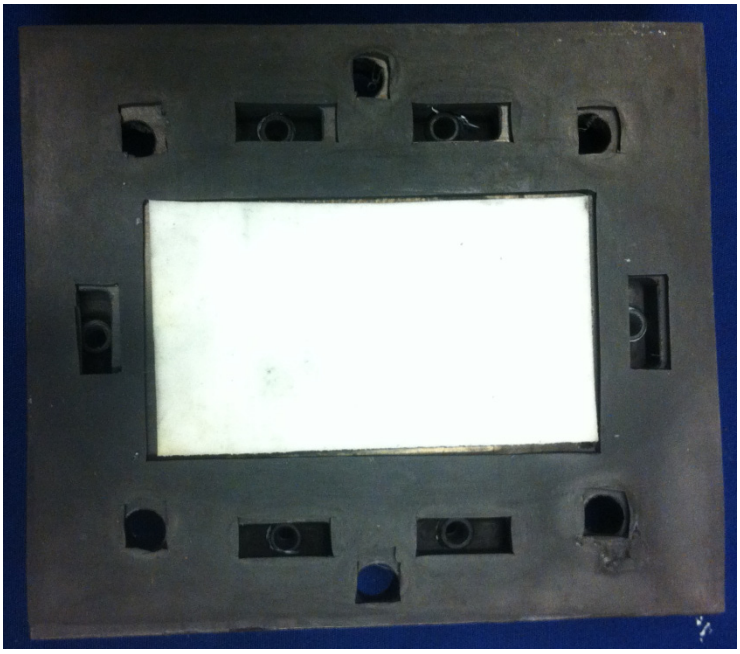

Figure 34 - Anode with FEC spacer and Viton gasket

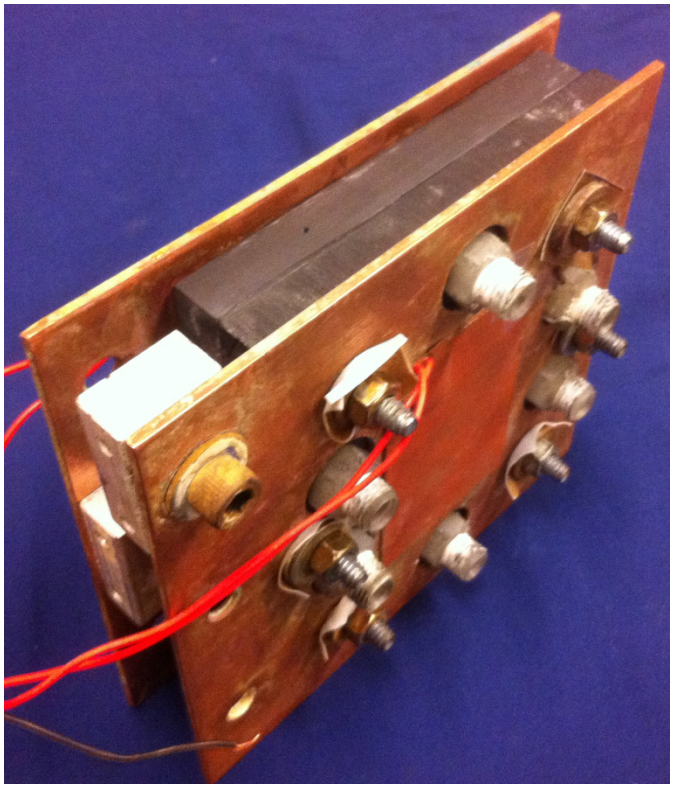

Figure 35 - Assembled FE-DMFC

After installing new MEAs into the FE-DMFC, the cell was flushed with only distilled water in the anode and in the flowing electrolyte channel for 2 hours. The cell was then operated with methanol, sulphuric acid, and air at zero current until steady state was reached. Finally, loads of 300 mV were alternated with zero current in 15-minute cycles until the response became repeatable. This process ensured proper activation of new MEAs for steady results.

4.2.2 Experimental Setup

The experimental setup for the operating fuel cell includes fluid control, temperature control, and load control systems. A photograph of the setup can be seen in Figure 36, and a schematic of the setup can be seen in Figure 37.

The methanol and sulphuric acid are each separately supplied in containers and pumped through tubing to the anode and flowing electrolyte inlets of the fuel cell. The methanol is, in addition, heated by a ribbon heater to 30°C before entering the fuel cell. The methanol pump is a peristaltic pump (MASTERFlex C/L-77122-22), and the sulphuric acid pump is a positive displacement pump (Fluid Metering Inc RHB-PM6013). Both anode and electrolyte waste are collected in containers from the outlets.

Air is supplied to the cathode from an air compressor through tubing, passing through an air filter and manometer before entering the cell. Any liquid droplets in the cathode outlet waste are collected in a beaker.

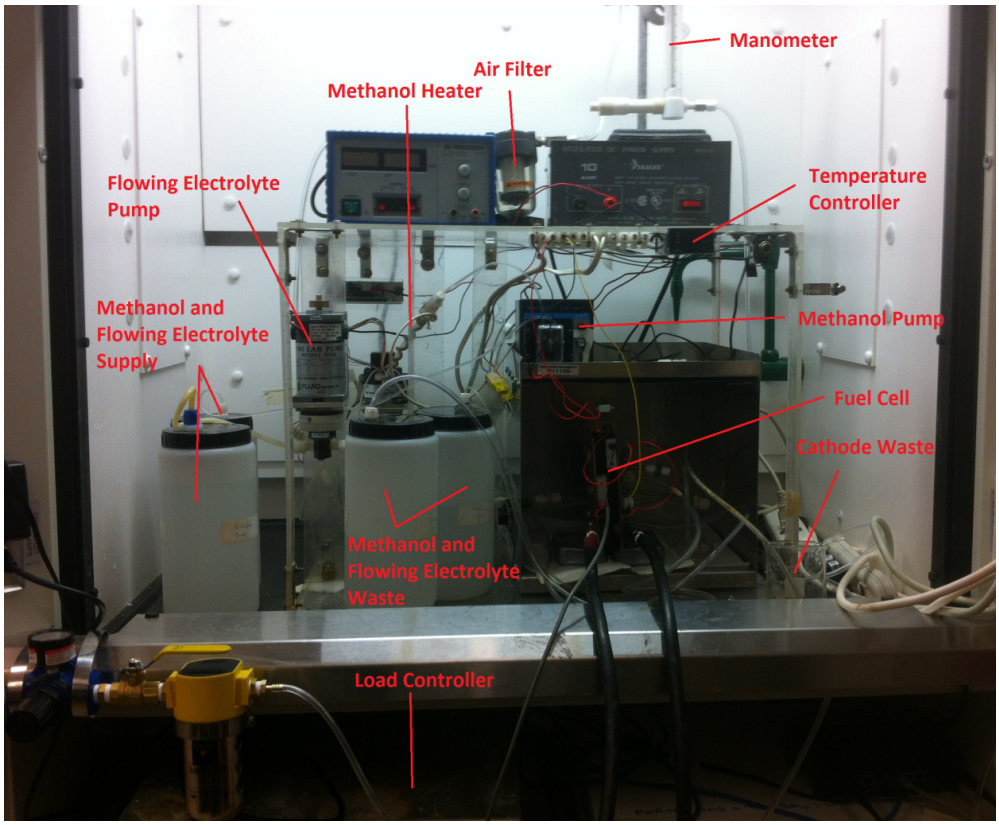

Figure 36 - Photograph of fuel cell experimental setup

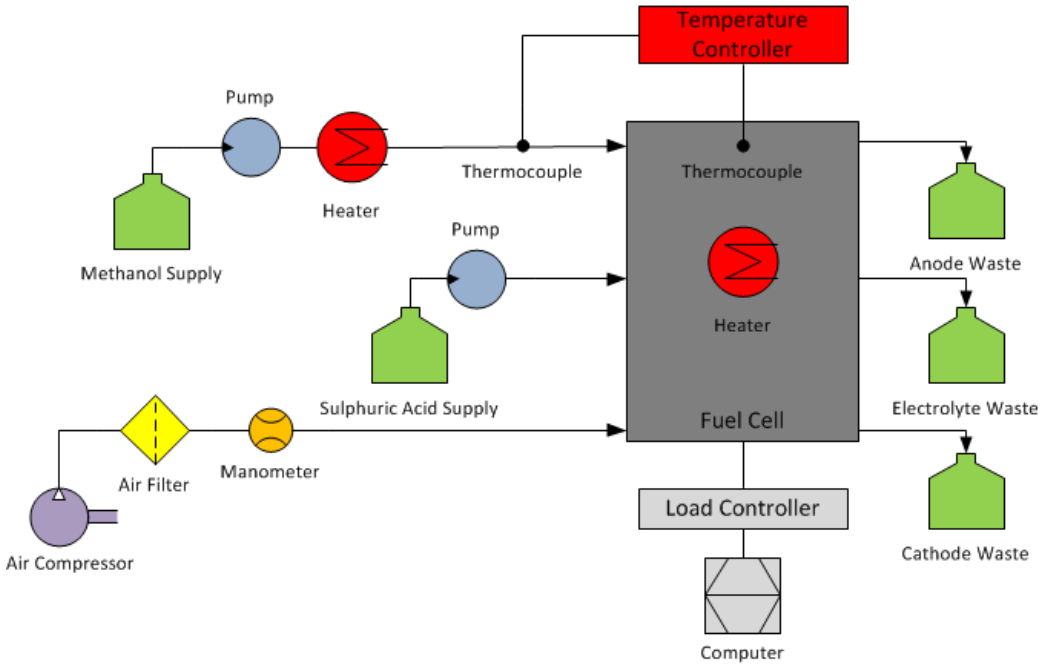

Figure 37 - Schematic of fuel cell experimental setup

Attached to either side of the fuel cell are OMEGALUX heating pads (SRFG-203/10-P). A TEF-30-K type thermocouple is inserted into a small hole at the top of the cathode backing plate to measure fuel cell temperature. An OMEGA CN-79000 temperature controller monitors and controls the temperature for both the cell and the methanol supply.

A digital load bank was used to monitor and control the electrical loads of the cell. A computer was used to control the load bank and log test results. In addition, the fuel cell was set up inside a Faraday cage to reduce the effects of external signals.

Equipment specifications can be found in Appendix B.

The fuel cell is oriented in a vertical position. The methanol flows upward, in order for buoyancy forces to aid in removing gas bubbles. Conversely, the air flows downward through the cell, in order for gravity to aid in removing liquid droplets. The electrolyte flows downward, so that the required pumping power is reduced.

4.2.3 Testing Procedures

Polarization curves were generated by the operating fuel cell at various conditions by conducting two-minute sweeps across the operating range from high voltage to low. Sweeps do not, however, go to the range below 100 mV, in order to avoid damaging the catalysts. The cell was always operated at zero current until steady state was achieved before running any sweeps.

The cell was tested for various flowing electrolyte flow rates using FECs with pore sizes of 35, 70, and 90 μm. In addition, the channel with 70 μm pores was used for

temperatures of both 60 and 70°C. The baseline conditions that are used unless otherwise specified are shown in Table 2.

Three different porous spacers were used in the fuel cell experimental studies. The reported pore diameters by the manufacturers of the three spacers were reported to be 35, 70, and 90 μm, respectively. The thicknesses for all three were all reported to be $^1/_{16}$"; however, the actual measured thickness differed slightly for each. The details of each spacer can be seen in Table 3.

Table 2 - Baseline conditions for fuel cell experiments

Parameter	Units	Value
Cell Temperature	°C	70
Anode inlet temperature	°C	30
Anode volume flux	mL/min/(75 mm^2)	10
Methanol concentration	mol/L or M	2
FE volume flux	mL/min/(75 mm^2)	10
FE concentration	mol/L or M	2
Air flow rate	mL/min	500
Clamping torque	in·lb	60

Table 3 - Details of porous spacers in flowing electrolyte channel

Sample	Pore Diameter [μm]	Reported Thickness [in (mm)]	Actual Thickness [in (mm)]	Material
1	35	$^1/_{16}$ (1.5875)	0.0685 (1.74)	Polyethylene (PE)
2	70	$^1/_{16}$ (1.5875)	0.0709 (1.80)	Polyethylene (PE)
3	90	$^1/_{16}$ (1.5875)	0.0630 (1.60)	Polypropylene (PP)

4.3 Uncertainty Analysis

An uncertainty analysis was conducted in accordance with ANSI/ASME PTC 19.1 [47]. The identified elemental sources of error affecting the voltage measurements of

the cell were air, methanol, and sulphuric acid flow rate, cell temperature, methanol and flowing electrolyte concentration, clamping torque, and flowing electrolyte channel thickness.

A summary of the procedure and important results can be found in Appendix A. The total bias and random uncertainties for the voltage measurements were estimated to be 11.7 and 5.5 mV, respectively. The total voltage uncertainty is therefore estimated at 14.0 mV. The maximum uncertainty for the cell power is calculated to be 1.19 mW.

4.4 Experimental Results

4.4.1 General Behaviour

An example of a curve generated is shown in Figure 38 for the baseline conditions using the spacer with a 70 μm pore diameter. Note that the scale for the polarization curve (blue) is indicated by an arrow to be on the left side; similarly, the scale for the power curve (red) is indicated to be on the right side. As with all curves presented in this chapter, it is generated by averaging the results of a minimum of three runs. Error bars of the magnitudes specified in Section 4.3 are shown here for proper visualization of the uncertainty size; in following graphs, the error bars are usually not shown to avoid confusion.

The shape of the polarization curve is consistent with typical FE-DMFC polarization curves [11, 34, 24]. The most notable trend is the nearly linear downward trend of the voltage, which is an indication of the high ohmic losses resulting from the thick FEC. Activation and mass transport losses are not noticeable on this graph; they tend to cause steep losses at the beginning and end of the curve, respectively. However, it

is likely that mass transport losses would become noticeable in the low-voltage region if the sweep were to continue to zero voltage. This general dominance of linear ohmic losses is, however, indicative of the significant challenge of reducing ohmic losses in FE-DMFCs.

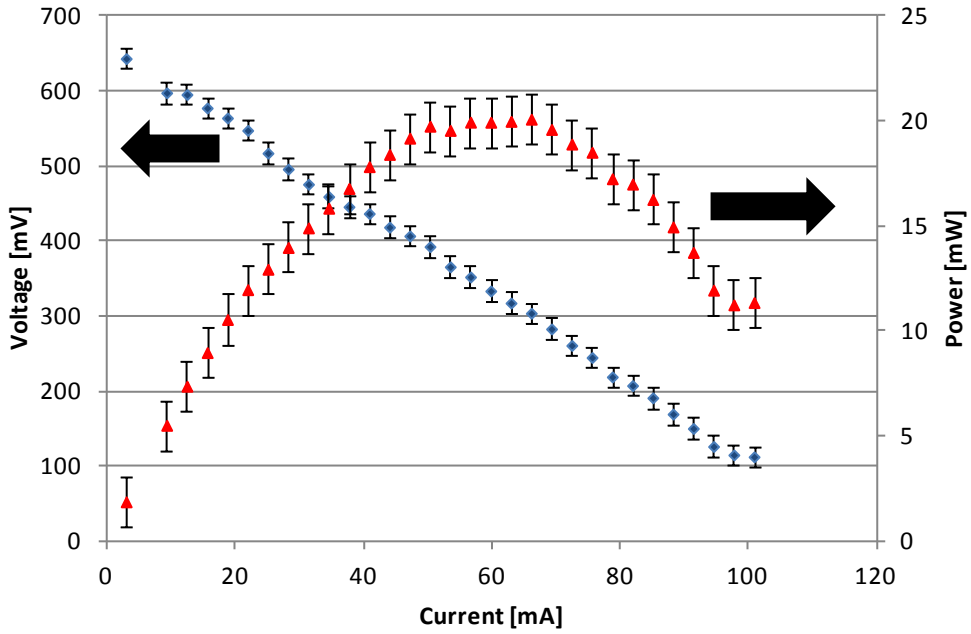

Figure 38 - Polarization and power curves for 10 mL/min flow with a pored diameter of 70 µm

The power curve is generated as the product of the measured current and voltage, since:

$$\mathbf{P = iV} \qquad (14)$$

It peaks in the mid to upper range of the current here, as it typically does, since it will tend back towards zero as either the current or voltage approach zero.

4.4.2 Temperature Effects

The fuel cell was operated with the 70 µm porous spacer at two different temperatures (60 and 70°C) in order to examine the effects of temperature, as shown in Figure 39.

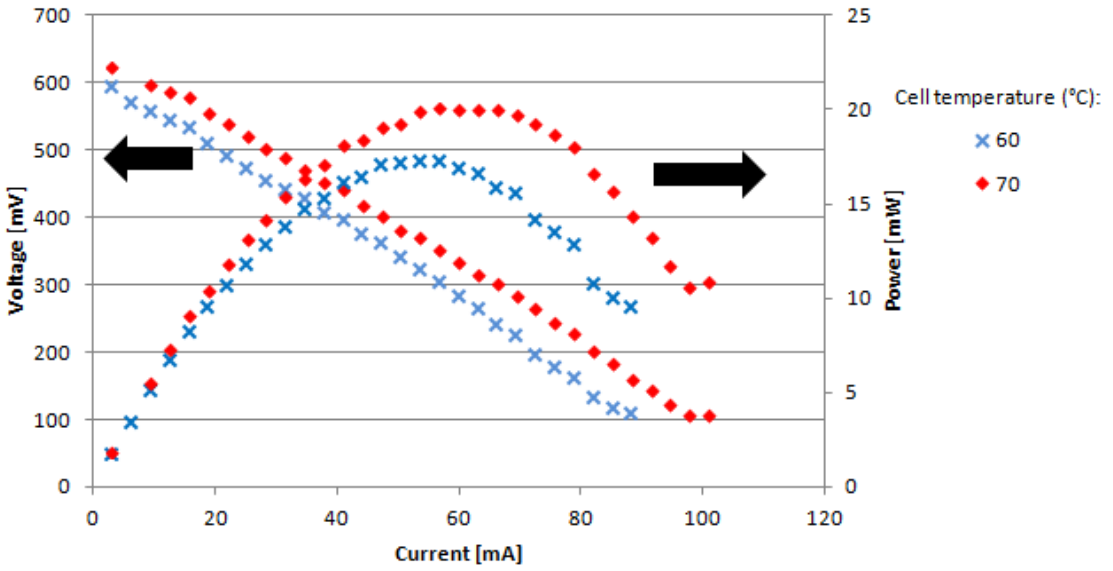

Figure 39 - Fuel cell performance at different temperatures

As expected, the higher temperature results in better performance, with a noticeably higher voltage and resulting power. This is likely because higher temperatures result in better reaction kinetics and more accelerated mass transport. In fact, these results seem to indicate a more gradual slope of the polarization curve for the higher temperature; this may be a result of improved ionic transport decreasing the ohmic resistance of the PEMs. Methanol crossover is known to increase in a DMFC at higher temperatures; there is, however, increased performance at higher temperatures. The flowing electrolyte channel is therefore likely reducing the negative effects of methanol

crossover. Overall, these results confirm that higher cell temperatures are beneficial to FE-DMFC performance.

4.4.3 Effects of Pore Diameter

Several flow rates were used for each of the three porous spacers. Figure 40 shows the cell performance comparison with an electrolyte flow rate of 2 mL/min, while Figure 41 and Figure 42 show flow rates of 5 and 10 mL/min, respectively.

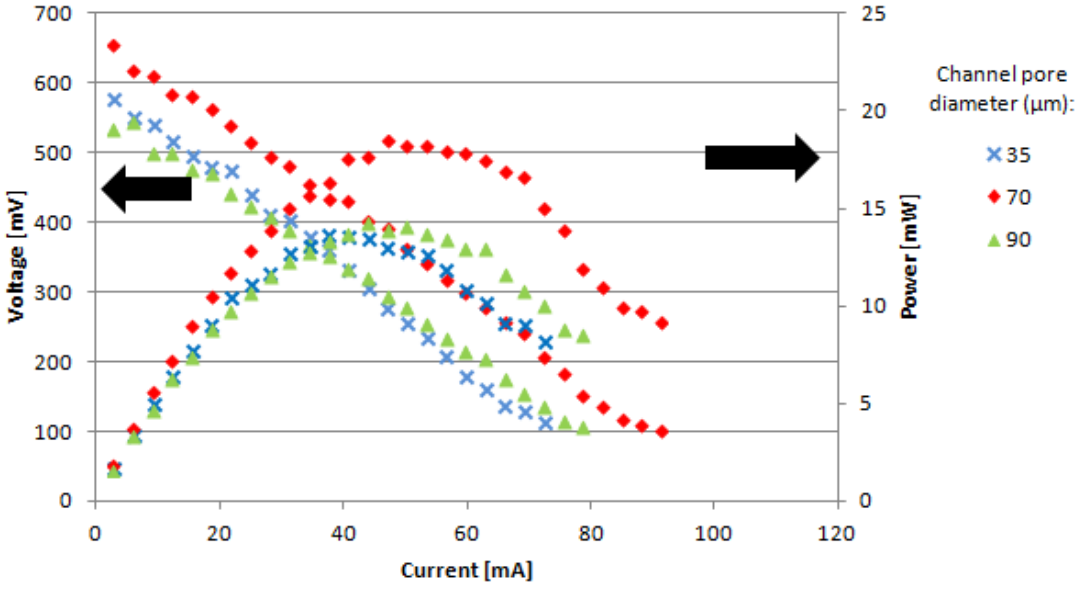

Figure 40 - Effects of pore diameter for an electrolyte flow rate of 2 mL/min

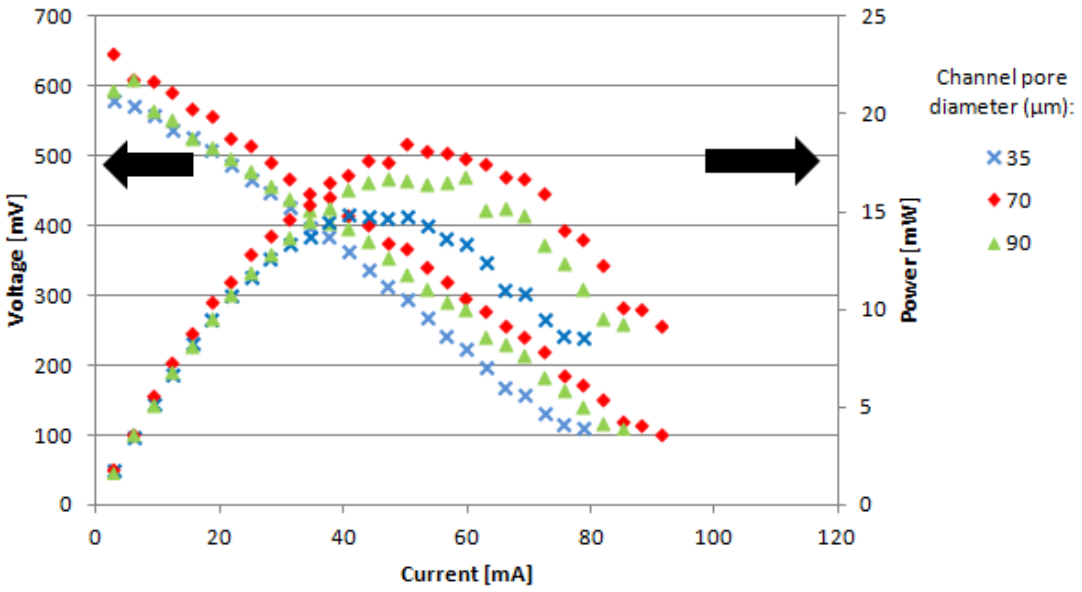

Figure 41 - Effects of pore diameter for an electrolyte flow rate of 5 mL/min

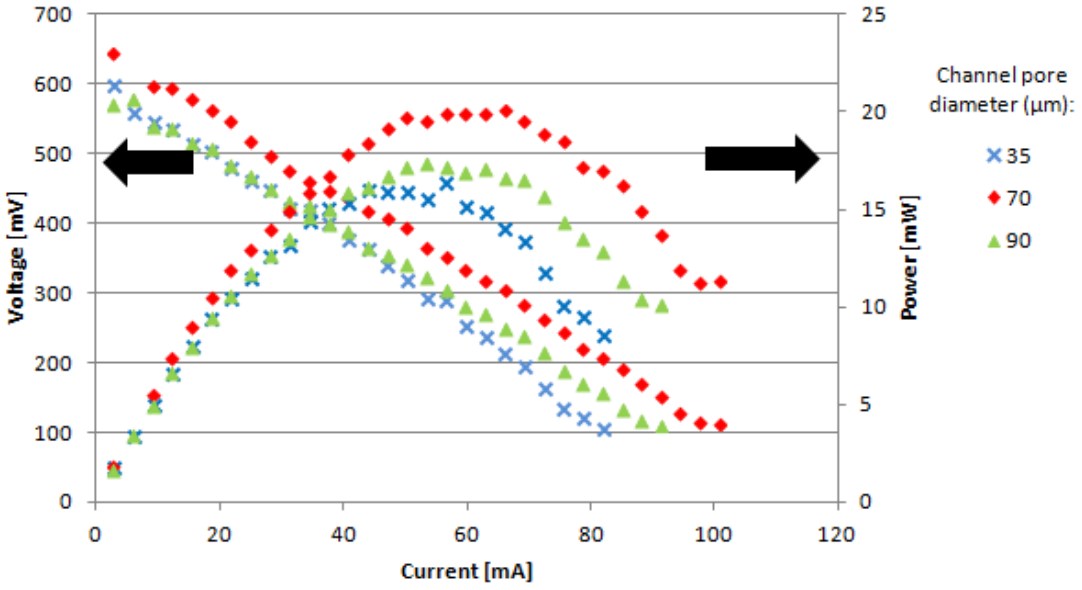

Figure 42 - Effects of pore diameter for an electrolyte flow rate of 10 mL/min

In all three cases, the performance of the 70 µm sample was best, while the 90 µm sample performed better than the 35 µm sample. It is difficult to explain this result based

on the differing pore sizes. While the pore size changes the pressure drop along the channel, this will affect the pumping power required for the flowing electrolyte, but does not have an obvious reason for affecting the voltage and power. It is possible that this discrepancy is partly a result of the differences in the measured thicknesses of the spacers; however, this cannot be the only factor since the performance rankings of the three spacers does not match their rankings by thickness. Other possible factors in this result may include undetected internal leakage in the cell, deterioration of the backing plates or PTFE tape, or decreasing effectiveness of the catalysts over time.

4.4.4 Effects of Electrolyte Flow Rate

For each porous spacer, the electrolyte flow rate was varied between 2 and 20 mL/min. The resulting polarization and power curves are shown in Figure 43, Figure 44, and Figure 45 for pore diameters of 35, 70, and 90 μm, respectively.

In all three cases, generally improved performance is observed when increasing the flow rate from 2 to 5 and 10 mL/min, with the exception of the 70 μm case when increasing from 2 to 5 mL/min. This general improvement suggests that the performance is improved by reduced methanol crossover, as expected.

For the 15 and 20 mL/min cases, however, trends are less clear. For the case with the 70 μm pore diameter, performance with flow rates of 15 and 20 mL/min are noticeably worse than with a 10 mL/min flow rate. For the 90 μm case, the performance with a 15 mL/min flow rate is marginally better than the 10 mL/min case, but marginally worse for the 20 mL/min case. This is counterintuitive, since higher electrolyte flow rates are always expected to improve the performance by reducing methanol crossover.

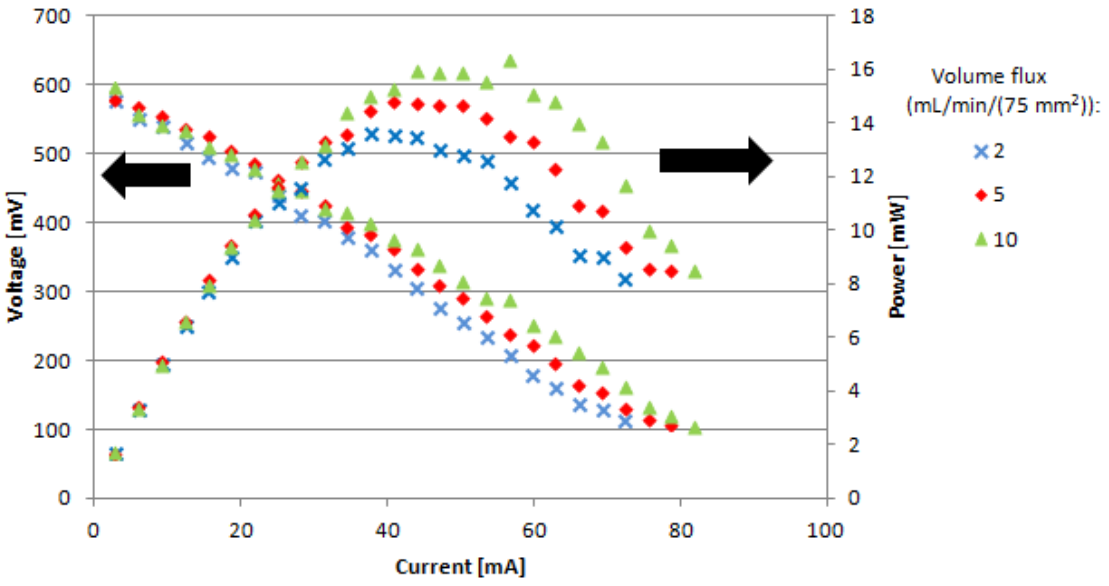

Figure 43 - Effects of electrolyte flow rate for a channel with a 35 µm pore diameter

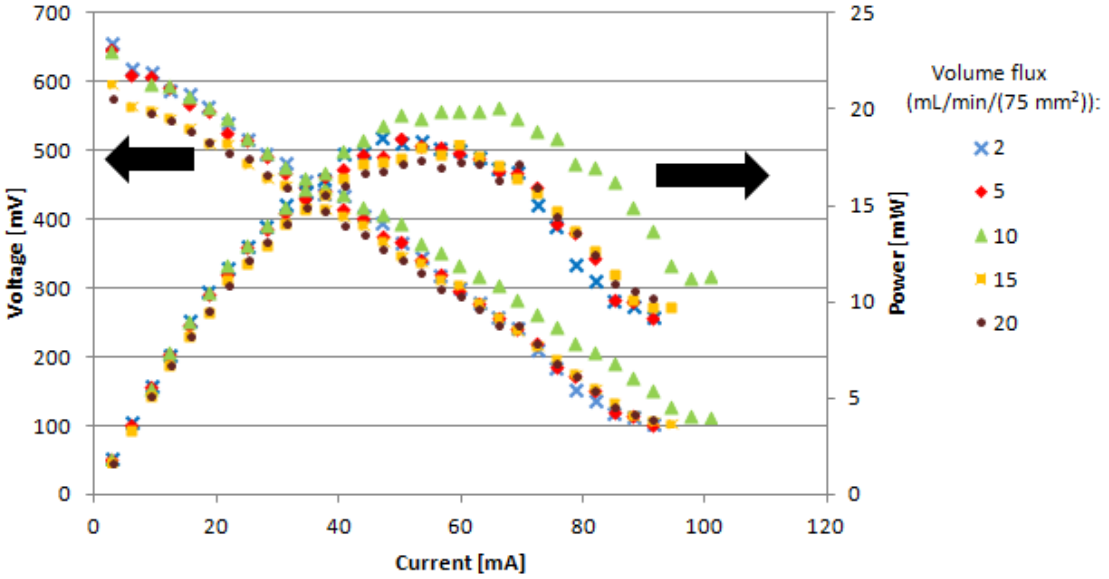

Figure 44 - Effects of electrolyte flow rate for a channel with a 70 µm pore diameter

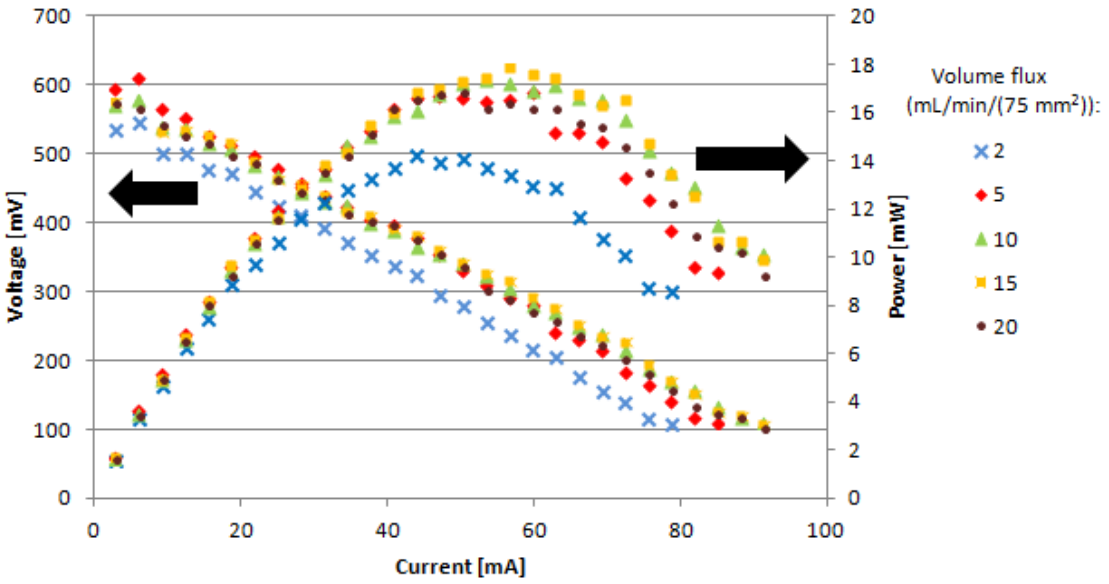

Figure 45 - Effects of electrolyte flow rate for a channel with a 90 µm pore diameter

It is possible that this decrease in performance at the highest flow rates is a result of high pressure drops along the flowing electrolyte channel. As discussed in Section 3.2.3, pressure drop increases linearly with flow rate. The higher pressure drops at the higher flow rates may be causing adverse effects such as leakage through the graphite or PTFE tape seams, or compression of the backing layers. This hypothesis is supported by the fact that the performance decrease at higher flow rates is more significant for the 70 µm case than the 90 µm case; the 70 µm case is expected to have a higher pressure drop because the pore diameters are smaller, as established in Section 3.2.5.

4.4.5 Summary of Important Results

The most important results of this fuel cell performance experimental study can be summarized as follows:

- A higher cell temperature improves cell performance, likely due to improved reaction kinetics and mass transport. Enhanced methanol crossover as a result of the higher temperature is not a noticeable factor, as it is likely negated by the flowing electrolyte.
- The porous spacer sample with a 70 μm pore diameter generally resulted in better performance than the 35 or 90 μm spacer samples. The cause of this result is unknown.
- Performance generally improved with increased electrolyte flow rate up to 10 mL/min, likely as a result of reduced methanol crossover. For higher flow rates, trends were less consistent, possibly as a result of adverse effects caused by increased pressure drops.

5 Chapter: Permeability Measurement

Since the permeability estimates calculated from Equation 13 in Chapter 3 are theoretical, it is of interest to experimentally determine the permeability of the spacers. This will allow for verification of this equation's applicability to the porous spacers.

5.1 Experimental Setup and Components

As demonstrated in literature [42, 43], the permeability of a porous material can be determined by measuring the pressure drop of fluid flowing through the material. If the fluid properties, material thickness, and flow rate are known, the permeability can be calculated from Equation 12, as rearranged here to isolate the permeability coefficient:

$$K_{perm} = \frac{-q\mu L}{\Delta P}$$

A test rig was fabricated for this study to pump water through a porous spacer and measure the pressure drop of the fluid, as shown in a schematic in Figure 46. Distilled water in a beaker was pumped through tubing by a positive displacement pump (Fluid Metering Inc RHB-PM6013) through an aluminum rig with threaded fittings, shown in Figure 47. This aluminum rig clamped a circular porous material sample across the flow, with Viton gaskets around the circumference of the sample to prevent flow from bypassing the porous material. The aluminum rig was clamped with six threaded bolts

fastened through holes in the aluminum arranged circumferentially around the sample. The water exited the outlet of the aluminum rig to be collected into a beaker. The flow rate was measured by measuring the volume of the outflow in a specified amount of time. There was also a differential pressure transducer (OMEGA model PX409-001DWU5V) connected to the flow by a T-junction upstream of the aluminum rig, as shown in Figure 48. All tubing lengths between the T-junction, the transducer, and the aluminum rig were kept short to minimize the pressure losses in the tubes. Specifications for the equipment can be found in Appendix B.

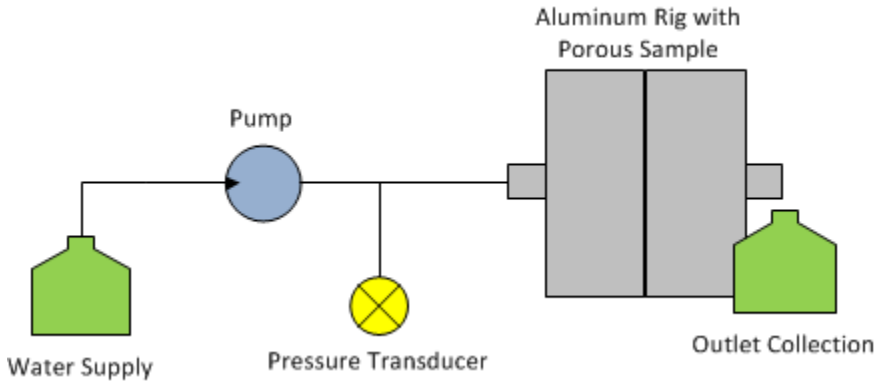

Figure 46 - Schematic of permeability testing experimental setup

The porous spacer is clamped in place over a circular cross-section with a diameter of 1 in (2.54 cm). The actual diameter of the cross-sectional flow area in the spacer is 2 mm less, due to the 1 mm overlap of the gaskets around the circumference.

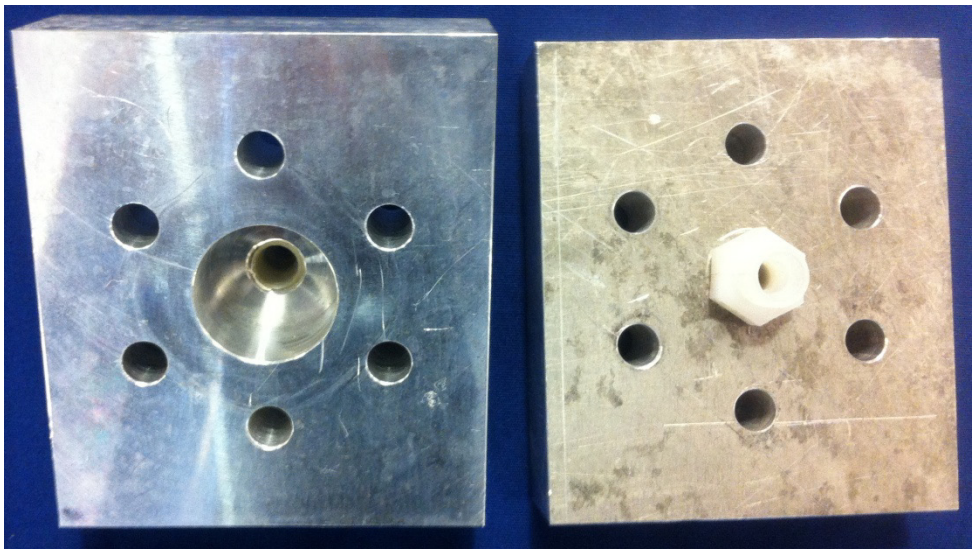

Figure 47 - Aluminum plates for permeability testing rig

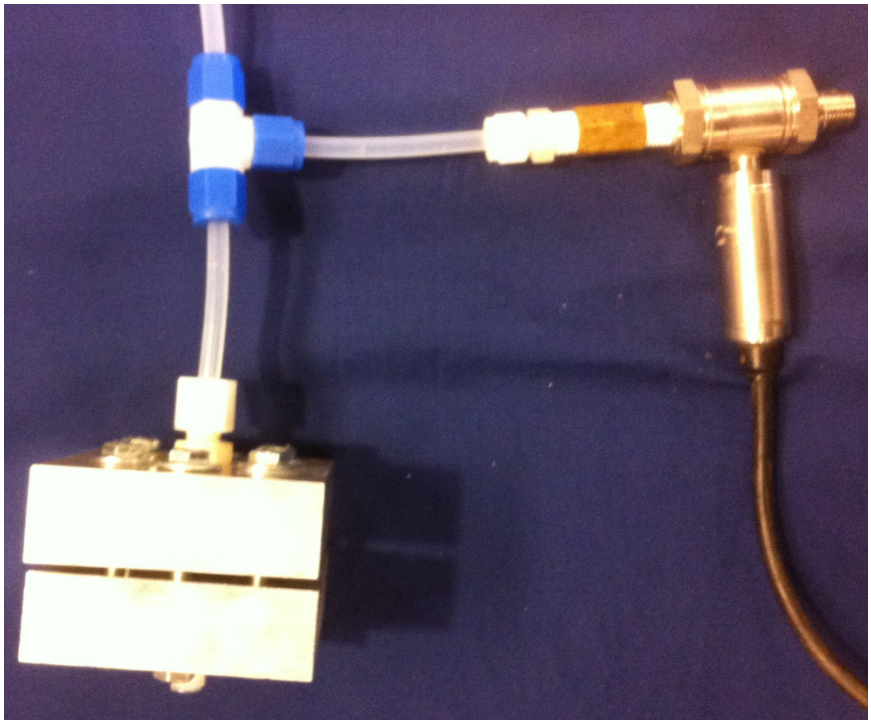

Figure 48 - Aluminum rig connected to pressure transducer

Experiments were conducted at ambient temperature by varying and measuring the flow rate in increments, and measuring the resulting pressure drop with the pressure transducer. Since one end of the differential transducer was open to atmospheric pressure, as was the outlet of the aluminum rig, the differential pressure measured is the pressure drop across the rig.

5.2 Results and Conclusions

The pressure versus flow rate results can be seen for the 35, 70, and 90 µm pore diameter samples in Figure 49, Figure 50, and Figure 51, respectively. Each is shown with a line of best fit, and error bars on the values, as estimated in Appendix A.

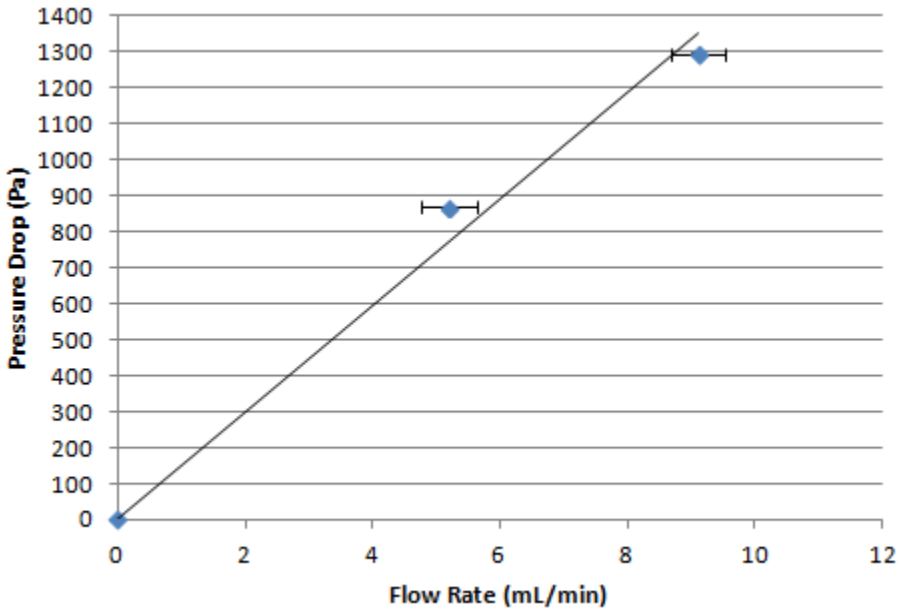

Figure 49 - Pressure vs. flow rate for a sample with a 35 µm pore diameter

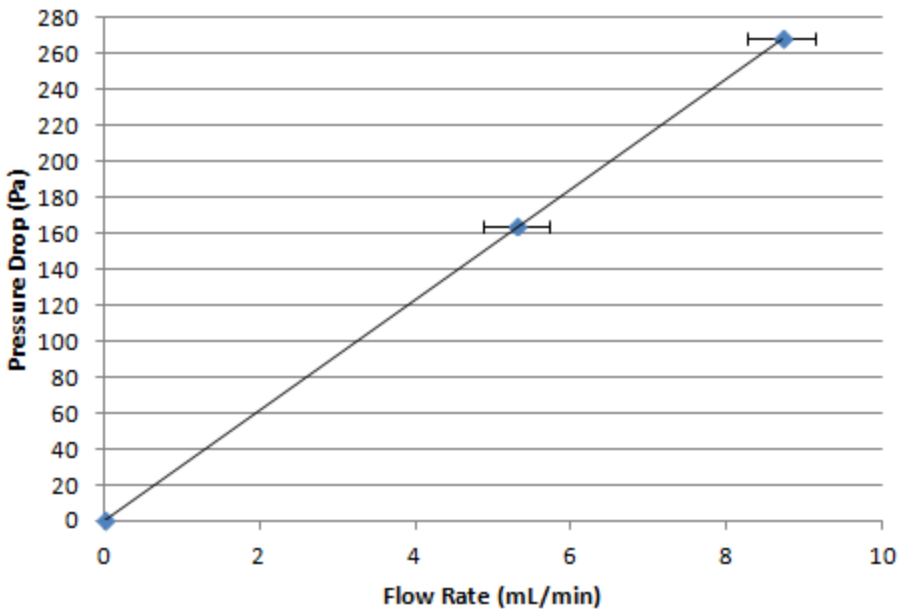

Figure 50 - Pressure vs flow rate for a sample with a 70 µm pore diameter

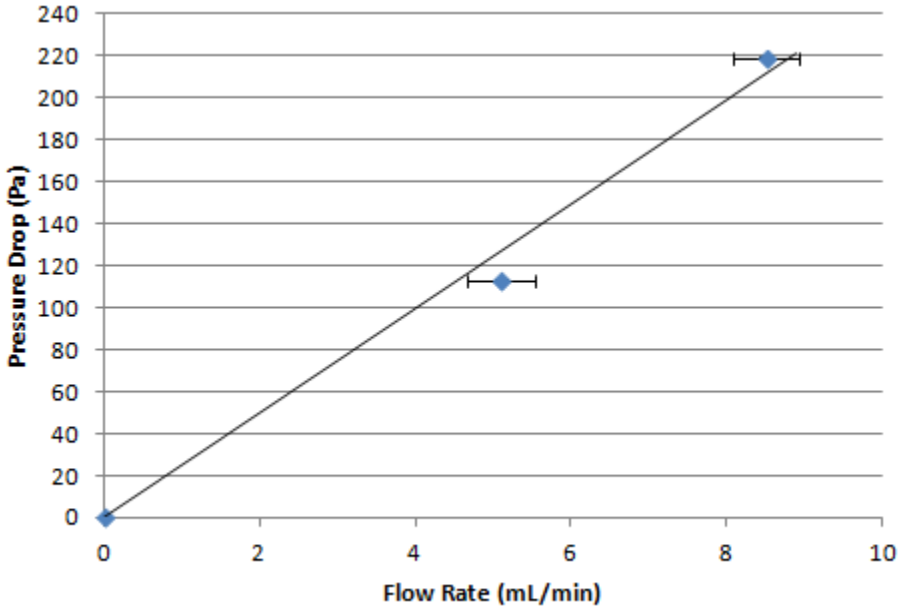

Figure 51 - Pressure vs flow rate for a sample with a 90 µm pore diameter

In order to obtain a permeability estimate from a graph, the slope of a line of best fit must be calculated. Dividing the slope by the cross-sectional area of the flow (since volume flux is flow rate divided by area) through the porous spacer yields the quantity pressure drop per volume flux ($\Delta P/q$), which can be substituted into Equation 12 along with the thickness of the spacer (tabulated in Table 3) and the fluid viscosity to calculate the permeability. The calculated permeabilities are shown in Table 4, compared with their theoretical values as predicted by Equation 13 using the manufacturer-specified pore size and the experimentally-measured porosity. The "Error" column denotes the percentage that the experimental value differs from the theoretical value. Note that the maximum uncertainty of the experimental permeability values is estimated at 2.2×10^{-14} m^2, as shown in Appendix A.

Table 4 - Comparison of experimental and theoretical permeability values

Pore Diameter (μm)	Experimental Permeability (m^2)	Porosity	Theoretical Permeability (m^2)	Error (%)
35	4.04×10^{-13}	0.35	6.80×10^{-13}	-40.6
70	2.01×10^{-12}	0.33	1.97×10^{-12}	2.0
90	2.22×10^{-12}	0.33	3.25×10^{-12}	-31.7

The porosity estimates used to calculate the theoretical permeabilities were obtained by measuring the dimensions and mass of porous samples both when dry and when saturated with isopropyl alcohol; the volume of the isopropyl alcohol could then be calculated and used to determine the porosity as the ratio of void volume (saturated with alcohol) to total volume.

It is observed that the experimental values of permeability are of the same order of magnitude as the theoretical values, with error varying from 2.0% to -40.6%. Possible

causes of the discrepancies include the uncertainty of the compression of the spacers and the structure of the porous material.

It is possible that the compression of the spacers in the test rig causes the porosity to be effectively reduced. It was noticed that the porous samples became slightly deformed, bulging in the downstream direction. This deformation is a result of the pressure drop, and may have caused the samples to be compressed, reducing their porosity and permeability. The permeability can change very drastically based on porosity, as a porosity change from 0.35 to 0.30 will cause the permeability to decrease by approximately 57%, according to Equation 13.

The structure of the porous material was modelled as a bed of packed spheres for the theoretical permeability calculations. However, any non-spherical structures, a difference between reported and actual average pore size, or a wide variability in pore sizes may have contributed to inaccurate theoretical permeability estimates. For example, if the sample with a reported pore size of 35 μm actually has an average pore size of 27 μm (without altering the porosity), then that would entirely account for the difference between the theoretical and experimental permeability.

Given the sensitive nature of permeability values, these results indicate that the assumed model for estimating permeability is not far off. In addition, the magnitudes of the permeabilities of the three spacers relative to each other are similar to what was expected. This means that trends discussed in the previous chapter regarding the effects of increasing or decreasing the permeability are not invalid.

6 Chapter: Conclusions and Recommendations

6.1 Conclusions and Design Recommendations

6.1.1 Cell Temperature

Fuel cell temperature is an important design consideration because temperature affects reaction kinetics, fluid properties, and mass transport. It was demonstrated in the non-isothermal simulations that higher temperatures reduce the pressure drop in the flowing electrolyte channel due to the temperature-dependence of properties such as density and viscosity. Meanwhile, the electrolyte inlet temperature proved unimportant due to the short thermal entry length. In addition, cell performance is expected to improve at higher temperatures due to improved reactions kinetics; this was confirmed in the fuel cell performance experimental studies. The experimental studies also demonstrated no obvious adverse affects due to increased diffusion rates of methanol at higher temperatures; it is likely that the flowing electrolyte negated most of the crossover.

Operating at a higher cell temperature is therefore a beneficial course of action for improved cell performance and reduced electrolyte pressure drop, with temperatures of up to 70°C demonstrated. However, there are other factors to consider such as safety and avoiding boiling of the liquids, which would prevent the ideal temperature from approaching the boiling point of a methanol-water solution, which is around 90°C for a 2 M solution.

6.1.2 Electrolyte Flow Rate

As suggested in the flowing electrolyte channel modelling studies, and verified by Darcy's Law, the pressure drop of the flowing electrolyte is roughly proportional to the volume flux, while virtually independent of channel thickness except for extremely thin channels. This is because the viscous effects of the porous domain are much more significant than the effects of the wall and boundary layers.

Methanol crossover can be reduced by increasing the electrolyte volume flux or increasing the channel thickness. However, it has been established by other researchers [21, 22] that a flowing electrolyte channel that is as thin as practically achievable is desirable because it minimizes the ohmic losses of the cell, and that increasing the volume flux of the flowing electrolyte is therefore a more beneficial method of maximizing the methanol removal. The modelling in the current study suggests that this would be a reasonable approach, since a flow channel thickness of 0.1 mm or possibly lower would have only a small effect (around 10%) on pressure drop at a practical constant volume flux.

The fuel cell performance experiments in the current study investigated the effects of increasing the electrolyte flow rate. While improvements were consistently observed for flow rates of up 10 mL/min, the trends at higher flow rates were inconsistent. Other experimental studies [11, 34] agree with the modelling study that performance improves for higher flow rates due to reduced methanol crossover, so this is almost certainly true. The source of inconsistencies at higher flow rates in the current experimental study is likely an unforeseen adverse effect of high flow rates and pressure drop such as leakage through the graphite plates or the PTFE tape seams.

It is therefore recommended that higher electrolyte flow rates should be used to reduce the methanol crossover in a relatively thin channel for best performance. However, care must be taken in fuel cell design to accommodate for the pressure losses that are expected to occur, since a fuel cell involves many thin, fragile, or porous components.

6.1.3 Porous Material Properties

In hydrodynamic modelling of the flowing electrolyte channel, it was shown that permeability has a significant effect on pressure drop. Relatively small changes to the physical structure of the porous material (i.e., porosity, sphere diameter) can affect the value of permeability by orders of magnitude, which in turn affects the pressure drop by orders of magnitude. A larger permeability is desirable to reduce pressure drop, which can be achieved with a larger porosity and sphere diameter.

As previously mentioned, in a recent 1-dimensional multiphase mixture performance model of an FE-DMFC by Ouellette *et al.* [24], several observations were made regarding methanol crossover. It was found that methanol crossover is more significant when the porosity is higher (with constant permeability). The variation in methanol crossover with permeability was, conversely, very small. From the standpoint of reducing methanol crossover, therefore, a beneficial design for the flowing electrolyte channel would be with a lower porosity, with the selection of permeability being much less important.

A recommendation on flowing electrolyte channel design can be made by considering both the hydrodynamics examined in the current modelling studies and the

methanol crossover considered by Ouellette *et al.* Although a lower porosity can result in a higher pressure drop when varied independently of sphere diameter, this is outweighed by the benefits of reducing methanol crossover. Since permeability does not greatly affect the methanol crossover, it should be increased in order to reduce the pressure drop. This can be accomplished by using a larger sphere diameter. A sphere diameter of 60-70 μm is therefore suggested, since it cannot be significantly increased beyond that without approaching the order of magnitude of the 0.61 mm channel thickness used in other FE-DMFC experimental studies [11, 24, 34]. At this sphere diameter, the porosity can go no lower than 0.4 without increasing the pressure drop above 10 kPa. Although this is a relatively high pressure drop, the increased pumping power is likely justified by the power gained by reducing methanol crossover.

An alternative suggestion would be to use a relatively higher porosity (around 0.6) to reduce pressure drop, while using a higher electrolyte flow rate to compensate for the increased methanol crossover resulting from the higher porosity. At the same sphere diameter and a porosity of 0.6, a pressure drop of under 1 kPa could be achieved with a volume flux of 10 mL/min/(75 mm^2); therefore, the volume flux could be doubled or tripled without even approaching the 10 kPa pressure drop predicted for a porosity of 0.4. It is possible that the flow rate could be selected to provide equivalent methanol crossover reduction with a lower pressure drop.

A larger pressure drop is, however, concerning in the physical design of the fuel cell, as it may cause material bulging, compression, leakage, or failure. High pressure drops in the flowing electrolyte channel proved to be of concern in the fuel cell experimental studies, since results were inconsistent at higher flow rates. If these

unwanted events could be avoided even at very high pressure drops, it is potentially beneficial to have a very high pressure drop that is compensated by drastically reduced methanol crossover.

6.2 Future Work

Several recommendations can be made for future work that would extend and improve upon the current work:

- Future fuel cell performance modelling studies can incorporate flat velocity profiles in the FEC.
- The possibility of using the discarded electrolyte from a FE-DMFC as fuel for another fuel cell could be investigated, in order to improve the efficiency of fuel usage.
- FE-DMFC experimental studies may incorporate electrolyte flowing upwards, in order to promote the removal of any gas bubbles that may form in the FEC
- Verification of the pressure drop predictions from the modelling study could be accomplished by measuring the pressure drop of the flowing electrolyte in a fuel cell. Water could be used as a substitute for the flowing electrolyte for this measurement to avoid damaging the pressure transducer.
- While limited varieties of commercially available porous spacers limited the flexibility of the current fuel cell performance experiments, future experimental work could incorporate specialized or custom porous materials to investigate the benefits of very thin spacers with sphere diameters as high as possible without approaching the order of magnitude of the channel thickness.

- With these custom porous spacers, experimentally investigating the performance of both higher and lower porosity samples would be very useful. Of particular interest would be to determine at what electrolyte flow rate a higher porosity spacer could achieve equivalent performance to a lower porosity spacer, and if this would be achieved at a lower pressure drop. If so, then that would be the recommended design for a flowing electrolyte channel.
- Fuel cells designed to withstand the higher pressure drops in the FEC associated with higher flow rates would be worthwhile. Some possible areas of improvement would be the robustness of the backing layers and the PTFE tape, and replacing the porous, fragile graphite plates with metal plates.
- Experimentally quantifying the permeability of all porous spacers used in fuel cell testing would be recommended in future studies due to the sensitivity of estimates. Also, determining the porosity and sphere diameter of samples would aid in making more accurate predictions.

References

[1] J. Larminie and A. Dicks, Fuel Cell Systems Explained, 2nd ed., West Sussex, England: John Wiley and Sons, 2003.

[2] U.S. Department of Energy, "Comparison of Fuel Cell Technologies," 2011. [Online]. Available: http://www1.eere.energy.gov/hydrogenandfuelcells/fuelcells/pdfs/fc_comparison_chart.pdf. [Accessed November 2013].

[3] U.S. Department of Energy, "Fuel Economy: Where the Energy Goes," [Online]. Available: http://www.fueleconomy.gov/feg/atv.shtml. [Accessed November 2013].

[4] R. O'Hayre, S. Cha, W. Colella and F. Prinz, Fuel Cell Fundamentals, Hoboken, NJ, USA: John Wiley & Sons, 2006.

[5] V. Bagotsky, Fuel Cells: Problems and Solutions, Hoboken, NJ, USA: John Wiley & Sons, 2009.

[6] G. Olah, "The methanol economy," *Chemical & Engineering News,* vol. 81, no. 38, p. 5, 2003.

[7] V. Oliveira, C. Rangel and A. Pino, "Effect of anode and cathode flow field design on the performance of a direct methanol fuel cell," *Chemical Engineering Journal,* vol. 157, pp. 174-80, 2010.

[8] D. Jung, C. Lee, C. Kim and D. Shin, "Performance of a direct methanol polymer electrolyte fuel cell," *Journal of Power Sources,* vol. 71, pp. 169-73, 1998.

[9] F. Liu, "Optimizing membrane electrode assembly of direct methanol fuel cells for portable

power, PhD thesis," Pennsylvania State University, 2006.

[10] K. Kordesch, V. Hacker and U. Bachhiesl, "Direct methanol-air fuel cell with membrane plus circulating electrolyte," *Journal of Power Sources,* vol. 96, pp. 200-3, 2001.

[11] N. Sabet-Shargi, "Experimental studies of a single cell flowing electrolyte-direct methanol fuel cell," Masters thesis, Carleton University, Ottawa, ON, Canada, 2011.

[12] K. Jiao and X. Li, "Review of water transport in polymer electrolyte membrane fuel cells," *Progress in Energy and Combustion Science,* vol. 37, pp. 221-91, 2011.

[13] K. Mauritz and R. Moore, "State of understanding of Nafion," *Chemical Reviews,* vol. 104, no. 10, pp. 4535-85, 2004.

[14] ANSYS Inc., "ANSYS CFX-Solver Theory Guide, Release 12.0," 2009. [Online]. Available: www1.ansys.com/customer/content/documentation/120/cfx/xthry.pdf. [Accessed March 2012].

[15] T. Shultz and K. Sundmacher, "Rigorous dynamic model of a direct methanol fuel cell based on MaxwellStefan mass transport equations and a Flory-Huggins activity model: formulation and experimental validation," *Journal of Power Sources,* vol. 145, pp. 435-62, 2005.

[16] D. Kareemulla and S. Jayanti, "Comprehensive one-dimensional, semi-analytical, mathematical model for liquid-feed polymer electrolyte membrane direct methanol fuel cells," *Journal of Power Sources,* vol. 188, pp. 367-78, 2009.

[17] J. Meyers and J. Newman, "Simulation of the direct methanol fuel cell - I. Thermodynamic framework for a multicomponent membrane," *Journal of the Electrochemical Society,* vol. 149, pp. 710-7, 2002.

[18] C. Xu, T. Zhao and W. Yang, "Modeling of water transport through membrane electrode assembly of direct methanol fuel cells," *Journal of Power Sources,* vol. 178, pp. 291-308, 2008.

[19] C. Wang and P. Cheng, "A two-phase mixture model of liquid-gas flow and heat transfer in capillary porous media - I. Formulation," *International Journal of Heat and Mass Transfer,* vol. 36, pp. 2747-58, 1993.

[20] W. Cai, S. Li, L. Yan, L. Feng, J. Zhang, W. Liang and C. Liu, "Design and simulation of a liquid electrolyte passive direct methanol fuel cell with low methanol crossover," *Journal of Power Sources,* vol. 196, pp. 7616-26, 2011.

[21] E. Kjeang, J. Goldak, M. Golriz, J. Gu, D. James and K. Kordesch, "A parametric study of methanol crossover in a flowing electrolyte-direct methanol fuel cell," *Journal of Power Sources,* vol. 153, pp. 89-99, 2006.

[22] C. Colpan, C. Cruickshank, E. Matida and F. Hamdullahpur, "1D modeling of a flowing electrolyte-direct methanol fuel cell," *Journal of Power Sources,* vol. 196, pp. 3572-82, 2011.

[23] C. Colpan, A. Fung and F. Hamdullahpur, "2D modeling of a flowing electrolyte-direct methanol fuel cell," *Journal of Power Sources,* vol. 209, pp. 301-11, 2012.

[24] D. Ouellette, C. Colpan, E. Matida and C. Cruickshank, "Multiphase mixture modelling and experimentation of the flowing electrolyte-direct methanol fuel cell," in *11th International Conference on Sustainable Energy Technologies*, Vancouver, BC, Canada, 2012.

[25] G. Lu and C. Wang, "Electrochemical and flow characterization of a direct methanol fuel

cell," *Journal of Power Sources,* vol. 134, pp. 33-40, 2004.

[26] A. Casalegno, P. Grassini and R. Marchesi, "Experimental analysis of methanol crossover in a direct methanol fuel cell," *Applied Thermal Energy,* vol. 27, pp. 748-54, 2007.

[27] C. Xu and T. Zhao, "Effect of anode backing layer on the cell performance of a direct methanol fuel cell," *Electrochimica Acta,* vol. 51, pp. 5524-31, 2006.

[28] F. Liu and C. Wang, "Water and methanol crossover in DMFCs effect of anode diffusion media," *Electrochimica Acta,* vol. 53, pp. 5517-22, 2008.

[29] M. Ravikumar and A. Shukla, "Effect of methanol crossover in a liquid-feed polymer-electrolyte direct methanol fuel cell," *Journal of the Electrochemical Society,* vol. 143, pp. 2601-6, 1996.

[30] C. Du, T. Zhao and W. Yang, "Effect of methanol crossover on the cathode behavior of a DMFC: a half-cell investigation," *Electrochimica Acta,* vol. 52, pp. 5266-71, 2007.

[31] E. Coban, L. Markoski, A. Wieckowski and P. Kenis, "Microfluidic fuel cell based on laminar flow," *Journal of Power Sources,* vol. 128, pp. 54-60, 2004.

[32] F. Brushett, M. Naughton, J. Ng, L. Yin and P. Kenis, "Analysis of Pt/C electrode performance in a flowing electrolyte alkaline fuel cell," *International Journal of Hydrogen Energy,* vol. 37, pp. 2559-70, 2012.

[33] N. Sabet-Shargi, C. Cruickshank, E. Matida and Hamdullahpur, "Performance measurements of a single cell flowing electrolyte-direct methanol fuel cell (FE-DMFC)," *Journal of Power Sources,* vol. 230, pp. 194-200, 2013.

[34] Y. Kablou, "Hydrodynamic Modeling and Experimental Analysis of DMFC Stacks," Master's thesis, Carleton University, Ottawa, ON, Canada, 2012.

[35] D. Ouellette, C. Cruickshank and E. Matida, "Experimental investigation on the performance of a formic acid electrolyte-direct methanol fuel cell," *Journal of Fuel Cell Science and Technology,* vol. 11, 2013.

[36] S. Srinivas, A. Gupta, S. Gulati and A. Subramanyam Reddy, "Flow and mass transfer effects on viscous fluid in a porous channel with moving/stationary walls in presence of chemical reaction," *International Communications in Heat and Mass Transfer,* vol. 48, pp. 34-9, 2013.

[37] T. Mohammadnejad and A. Khoei, "An extended finite element method for hydraulic fracture propagation in deformable porous media with the cohesive crack model," *Finite Elements in Analysis and Design,* vol. 73, pp. 77-95, 2013.

[38] A. Salama, W. Li and S. Sun, "Finite volume approximation of the three-dimensional flow equation in axisymmetric, heterogenous porous media based on local analytical solution," *Journal of Hydrology,* vol. 501, pp. 45-55, 2013.

[39] J. Yuan and B. Sunden, "On mechanisms and models of multi-component gas diffusion in porous structures of fuel cell electrodes," *International Journal of Heat and Mass Transfer,* vol. 69, pp. 358-74, 2014.

[40] W. He, J. Zou, B. Wang, S. Vilayurganapathy, M. Zhou, X. Lin, K. Zhang, J. Lin, P. Xu and J. Dickerson, "Gas transport in porous electrodes of solid oxide fuel cells: A review on diffusion and diffusivity measurement," *Journal of Power Sources,* vol. 237, pp. 64-73, 2013.

[41] M. Kaviany, Principles of Heat Transfer in Porous Media, New York, NY, USA: Springer-Verlag, 1991.

[42] H. Taira and H. Lui, "In-situ measurements of GDL effective permeability and under-land cross-flow in a PEM fuel cell," *International Journal of Hydrogen Energy,* vol. 37, pp. 13725-30, 2012.

[43] I. Hussaini and C. Wang, "Measurement of relative permeability of fuel cell diffusion media," *Journal of Power Sources,* vol. 195, pp. 2830-40, 2010.

[44] F. Rhodes and C. Barbour, "The viscosities of mixtures of sulphuric acid and water," *Industrial and Engineering Chemistry,* vol. 15, no. 8, pp. 850-2, 1923.

[45] C. Musès, "Validating Kepler's conjecture: A new approach," *Applied Mathematics and Computation,* vol. 110, no. 1, pp. 99-104, 2000.

[46] L. Rong, K. Dong and A. Yu, "Lattice-Boltzmann simulation of fluid flow through packed beds of uniform spheres: Effect of porosity," *Chemical Engineering Science,* vol. 99, pp. 44-58, 2013.

[47] The American Society of Mechanical Engineers, Measurement Uncertainty: Instruments and Apparatus, New York, NY, USA, 1985.

Appendix A - Uncertainty Analysis

A.1 Equations

This appendix gives further detail about the uncertainty analysis conducted for the performance testing of the FE-DMFC discussed in Chapter 3, which is based on ANSI/ASME PTC 19.1 [47]. The two types of errors are systematic or bias errors (S), which shift the measured values away from the true value by a fixed amount, and random errors (R), which is the scattering of measurements around the sample mean.

The true value of a quantity that is measured is x, which is unknown, but the average of the measurements, $\bar{x}$, can be calculated. Then the true value can be expected to lie in the range of $\bar{x}$ plus or minus an uncertainty value, U_x, as shown:

$$x = \bar{x} \mp U_x \quad \text{(A. 1)}$$

Calculating a reasonable estimate for U_x is the goal of conducting an uncertainty analysis. It consists of both bias (S_x) and random (R_x) error components of x. Both the overall bias and random errors can be calculated as a root sum square of the individual elemental sources of bias and error, as shown:

$$e = \sqrt{\sum_i (e_i)^2} \quad \text{(A. 2)}$$

where e_i are the individual elemental errors and e is either the overall bias or random error.

Then, the overall uncertainty of x, U_x, can be estimated from the overall bias and random errors by:

$$U_x = \sqrt{B_x^2 + t_{\upsilon,95} R_x^2} \quad \text{(A. 3)}$$

where $t_{\upsilon,95}$ is the Student t-factor for a 95% confidence interval, which is 1.960 in a normal distribution for the limit of many measurements.

Often, the uncertainty of the quantity that measured is not the quantity of interest; rather, the quantity of interest, y, is affected by the measured quantity x. Therefore, the uncertainty of x propagates into the uncertainty of y. The bias of y, B_y, can then be calculated from the elemental sources of bias error of x, B_{x_i}, as:

$$B_y = \sqrt{\sum_i (\theta_i B_{x_i})^2} \quad \text{(A. 4)}$$

where θ_i is the sensitivity index for each elemental error source. Note that Equation A.4 is similarly applied to random errors. The sensitivity index is defined as:

$$\theta_y = \frac{\partial y}{\partial x_{i_{x=\bar{x}}}} \quad \text{(A. 5)}$$

where $x_{i_{x=\bar{x}}}$ is the elemental quantity x at the mean of samples. Therefore, the sensitivity index represents the slope of the y vs. x curve at the mean of x. This curve can be generated experimentally.

The uncertainties for both the voltage and current estimates can be estimated in this way. Then, the uncertainty for power can also be calculated from these, since power is a function of current and voltage, as was given in Equation 14:

$$P = iV$$

Utilizing Equations A.4, A.5, and 14, the bias or random error, e, of power can be expressed as:

$$e_P = \sqrt{(Ve_i)^2 + (ie_V)^2} \quad \text{(A. 6)}$$

A.2 Fuel Cell Performance Experimental Uncertainty Analysis

The elemental errors identified affecting the performance measurements of the fuel cell are air, methanol, and sulphuric acid flow rate, cell temperature, methanol and sulphuric acid concentration, clamping torque, and flowing electrolyte thickness. These elemental errors are estimated based on the equipment manufacturers' estimates, where available, the estimates of Sabet-Shargi [11] and Kablou [34], and personal experience. Where bias is not specifically known, it is often assumed to be equivalent to random error.

The rotameter measuring air flow rate had an accuracy of 5% or 2 mm of length scale. This results in the maximum uncertainty being 30 mL/min. Therefore, both bias and random error are estimated as 30 mL/min.

The methanol and flowing electrolyte flow rates were measured using a graduated cylinder for the volume of fluid passed in one minute. Bias and random errors are each estimated at 0.25 mL/min.

The estimates for temperature uncertainty are based on the temperature controller, the thermocouple uncertainty, and the thermocouple position. The temperature controller uncertainty is estimated as 0.5°C for bias and 0.25°C for random error. The thermocouple uncertainty is estimated as 2.2°C for bias and 1.0°C for random error. The thermocouple position uncertainty is estimated as 1.0°C for bias and 0.25°C for random error. These uncertainties can be combined using Equation A.2 for an overall temperature uncertainty of 2.47°C for bias and 1.06°C for random error.

The clamping torque was measured with a torque wrench with markings every 1 in·lb; the bias and random errors were therefore each estimated as 0.5 in·lb.

The flowing electrolyte channel thickness was measured with calipers with an estimated 0.02 mm bias and random error uncertainties.

Since the methanol and sulphuric acid solutions are created by diluting methanol or sulphuric acid with water, the concentration uncertainties are not estimated directly. Rather, the uncertainties for the mixed volumes can be estimated, and then propagated to the concentrations. First, it must be recognized that the following definition for the concentration of a diluted solution, C, holds true for a diluted solution:

$$C = C_i \frac{V_i}{V_f} \tag{A. 7}$$

where C_i is the initial concentration of the solution, and V_i and V_f represent the initial and final volumes of the solution. This equation can now be substituted into Equation A.4 to find B_c; Equation A.5 must also be used to express θ_c as $\frac{\partial C}{\partial V}$. Then the bias error of concentration is:

$$B_C = \sqrt{\left(\frac{V_i}{V_f} B_{c_i}\right)^2 + \left(\frac{C_i}{V_f} B_{V_i}\right)^2 + \left(-C_i \frac{V_i}{V_f{}^2} B_{V_f}\right)^2} \tag{A. 8}$$

and the random error can be calculated similarly.

The methanol and sulphuric acid solutions were always created in batches of 2000 mL; the initial supplied concentration was 99.8% by mass (24.66 M) for methanol and 95% by mass (17.82 M) for sulphuric acid. The biases of the initial and final volumes were estimated at 1 mL and 0.5 mL, respectively. The biases of the initial concentrations were estimated at 0.1% (0.025 M) for methanol and 1.5% (0.267 M) for sulphuric acid, based on the suppliers' estimated range of purity. The concentration bias uncertainties

could then be calculated from Equation A.8 as 0.0125 M and 0.0313 M for methanol and sulphuric acid, respectively. The random errors were assumed to be equivalent.

The important quantities for these elemental errors are summarized in Table A.1. The sensitivity coefficients for voltage and current are calculated from Equation A.5 as the slopes of curves generated experimentally. Note that their units are mV per unit specified in the first column. Then the B_v and R_v columns are the bias and random errors, respectively, propagated to voltage, as calculated from Equation A.4.

Table A. 1 - Summary of Parameters for Fuel Cell Experimental Uncertainty Analysis

	B	R	θ_v	B_v [mV]	R_v [mV]
Air flow rate [mL/min]	30	30	0.023	0.69	0.69
Methanol flow rate [mL/min]	0.25	0.25	6.4	1.6	1.6
Sulphuric acid flow rate [mL/min]	0.25	0.25	4.5	1.1	1.1
Cell temperature [°C]	2.47	1.06	4.6	11.5	4.9
Clamping torque [in·lb]	0.5	0.5	0.72	0.36	0.36
FEC thickness [mm]	0.02	0.02	33	0.66	0.66
Methanol concentration [mol/L]	0.0125	0.0125	27	0.33	0.33
Sulphuric acid concentration [mol/L]	0.0313	0.0313	29.6	0.93	0.93

Then, the total bias and random uncertainties for the voltage measurement can be calculated from Equation A.2 to be 11.7 and 5.5 mV, respectively. Applying Equation A.3, the total voltage uncertainty is estimated at 14.0 mV. Then the maximum uncertainty for the cell power is calculated from Equation A.6 to be 1.19 mW.

A.3 Permeability Testing Experimental Uncertainty Analysis

For the permeability testing, there were three identified error sources: the water flow rate measurement, the porous spacer thickness, and the transducer error.

The water flow rates were measured using a graduated cylinder for the volume of fluid passed in one minute. Bias and random errors are each estimated at 0.25 mL/min. Using Equation A.3, this results in a total uncertainty of 0.43 mL/min. The volume flux is obtained by dividing the flow rate by the cross-sectional area; the uncertainty of the volume flux is therefore obtained similarly from the uncertainty of the flow rate. The bias and random error of the volume flux is calculated to be 9.7×10^{-6} m/s, which results in a total uncertainty of 1.7×10^{-5} m/s.

The flowing electrolyte channel thickness was measured with calipers with an estimated 0.02 mm bias and random error uncertainties.

The transducer error is estimated by the manufacturer to be 0.08%. This is always less than 1 Pa for all values obtained, which is negligible compared to the flow rate error when pressure is graphed versus flow rate. The transducer error will therefore be ignored.

Permeability has already been stated to be calculated by Equation 12:

$$K_{perm} = \frac{-q\mu L}{\Delta P}$$

where q is the volume flux. Therefore, the uncertainties of the volume flux and the porous spacer thickness propagate to the permeability in accordance with Equation A.4, where the sensitivity coefficients are defined by Equation A.5 to be:

$$\theta_{K_q} = \frac{\partial K}{\partial q} = \frac{-\mu L}{\Delta P} = -1.26 \times 10^{-9} \mathrm{m \cdot s}$$

$$\theta_{K_L} = \frac{\partial K}{\partial L} = \frac{-q\mu}{\Delta P} = -2.46 \times 10^{-10} \mathrm{m}$$

Therefore, the bias and random uncertainty values of the permeability from the volume flux are each calculated from Equation A.4 to be 1.2×10^{-14} m^2, and the bias and random uncertainty values from the spacer thickness are each calculated to be 4.9×10^{-15} m^2. The total bias and random uncertainties are therefore calculated from Equation A.2 to each be 1.3×10^{-14} m^2, for a total uncertainty from Equation A.3 of 2.2×10^{-14} m^2.

Appendix B - Experimental Design

This section contains further details regarding equipment and components of the experimental designs.

B.1 Backing Plates

The backing plates in the FE-DMFC experimental design are made of graphite AR-08, and designed by Kablou [34]. Further details of the properties of graphite AR-08 are shown in Table B.1 [11], and drawings of the plate are shown in Figure B.1. All dimensions are shown in mm, except for threaded dimensions, which are in inches.

Table B.1 – Properties of graphite AR-08

Bulk density	1.80 g/cm^3
Particle size	11.9 μm
Hardness, Shore D	65
Flexural strength	51.7 MPa
Compressive strength	114 MPa
Electrical resistivity	0.00124 Ω·cm

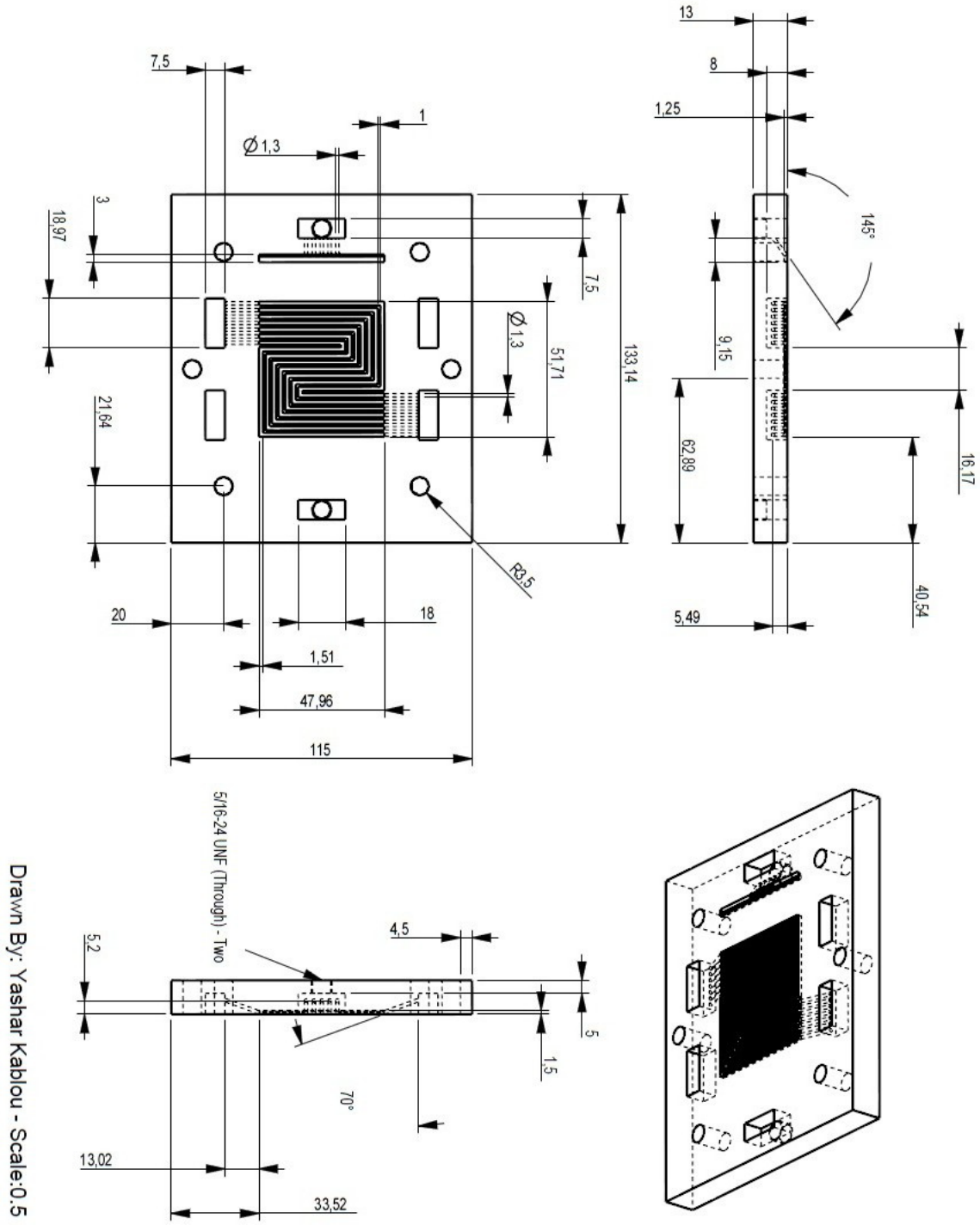

Figure B.1 - 3-view drawing of graphite backing plate [34]

B.2 Pumps

Two pumps were used in the experimental analyses: a positive displacement pump (Fluid Metering Inc. – RHB model) with internal Teflon coating for the water in the permeability tests and for sulphuric acid in the fuel cell tests, and a peristaltic pump (MASTERFlex C/L) for methanol. Their details are shown in Table B.2 [11].

Table B.2 - Pump specifications

Manufacturer	MASTERFlex	Fluid Metering Inc.
Model number	C/L-77122-22	RHB-PM6013
Speed range (rpm)	50 to 300	2200
Voltage (V)	115 (AC)	12 (DC)
Current	400 mA	4.3 A
Flow rate range (mL/min)	0 to 25	0 to 260
Temperature range (°C)	0 to 40	-
Material	Polyphenylene sulphide (PPS), polyester, and stainless steel	Wetted parts: ceramic and polyvinylidene fluoride (PVDF)

B.3 Rotameter

The Gilmont GF-9360 rotameter was used to monitor the air flow rate in the fuel cell tests; the specifications are given in Table B.3 [11].

Table B.3 - Rotameter specifications

Valve adjustment	0.1 to 100% of maximum flow
Precision	0.3 to 60% of maximum flow
Accuracy	5% of reading or 2 mm of length scale
Material	PTFE

B.4 Air Filter

The specifications of the air filter used upstream of the rotameter are given in Table B.4 [11].

Table B.4 - Air filter specifications

Particle allowance	1 μm
Maximum flow rate	20 scfm
Maximum operating pressure	100 psi
Maximum operating temperature	52°C (125°F)

B.5 Temperature Controller

An OMEGA temperature controller (CN-79000) was used to control the temperatures of the methanol inlet line and the fuel cell. Specifications are shown in Table B.5[11].

Table B.5 - Temperature controller specifications

On/off differential	Adjustable to 1C, 1°F, or 1 count of full scale
Supply voltage	100 to 240 V AC, nominal, 10-15%, 50 to 400 Hz
Operating temperature range	-10 to 55°C
Accuracy	0.25% of span

B.6 Thermocouple

A K-type thermocouple by J-KEM SCIENTIFIC INC (TEF-30-K) with a thin Teflon coating was used to measure the cell temperature, and its specifications are shown in Table B.6 [11].

Table B.6 - Thermocouple specifications

Material	Chromel-alumel wires with Teflon sealing
Dimensions	0.064 mm diameter; 914.4 mm length
Response time	0.1 s
Operating temperature range	-250 to 204°C
Precision	2.2°C or 0.75% of range

B.7 Heating Pads

Heating pads by OMEGA (SRFG-203/10-P) were used on the exterior of both the anode and cathode current collectors to maintain the fuel cell at the desired temperature. The specifications of the heating pads are shown in Table B.7 [11].

Table B.7 - Heating pad specifications

Material	Silicon rubber, Kapton
Area	2 in^2
Circuit design	Etched foil
Maximum operating temperature	120°C
Operating voltage	115 V (AC)
Heat flux	10 W/in^2

B.8 Load Bank

A Fideris (Innovator Series-250 kW) load bank was used for the fuel cell experiments, controlled by *FCPower* software. The specifications of the load bank are shown in Table B.8 [11].

Table B.8 - Load bank specifications

Type	MOSFET variable resistance load bank
Current measurement	Exchangeable shunts (1, 20, and 50 A)
Maximum current rating	50 A
Maximum voltage rating	20 V (DC)
Maximum power dissipation	250 W
Load capacitance	Less than 20 pF
Electrical requirements	26 to 50 V (DC)
Communication	Ethernet (requires DHCP)

B.9 Differential Pressure Transducer

A differential pressure transducer by OMEGA (PX409-001DWU5V) was used to measure the pressure drop in the permeability experiments; the specifications are shown in Table B.9. Not that a National Instruments data acquisition card (NI USB-6009) was used to acquire the output signals of the transducer [34].

Table B.9 - Pressure Transducer specifications

Wetted parts material	316L stainless steel
Response time	0.001 s
CE compliance	EN1326-1: 2006 for industrial locations
Bandwidth	DC to 1 kHz typical
Pressure cycles	1 million
Pressure ports	¼ NPT male
Electrical terminations	PX409: 2 m cable
Weight	200 g
Operating temperature range	-45 to 121°C
Operating pressure range	0 to 1 psi
Output impedance	100 Ω
Accuracy	0.08%
Output voltage	0 to 5 V (DC)
Operating voltage	10 to 30 V (DC)